ANALYSIS OF ISEE-1 AND 2 SPACECRAFT MAGNETOMETER DATA

by

Mark Andrew Saunders

Thesis submitted for the degree
of Doctor of Philosophy of the
University of London

The Blackett Laboratory,
Imperial College of
Science and Technology,
London SW7.

May, 1982.

'Man must rise above the Earth - to the top of the atmosphere and beyond - for only thus will he fully understand the world in which he lives'.

Socrates (469-399 B.C.)

ABSTRACT

A new interpretation is presented for the 'plasma vortices' discovered by Hones et al. (1978) from ISEE spacecraft data in the tail region of the Earth's magnetosphere. Although the 11th December 1977 vortex event receives particular study through a synthesis of magnetometer, plasma, electric field and energetic particle data, this event is not atypical. Apparent vortical motion is seen in the ecliptic plane because the plasma flow parallel to $\underline{B}$ is in quadrature to the flow perpendicular to $\underline{B}$. The vortices are hot plasma hydromagnetic wave features associated with the coupling of the Alfvén mode to the MHD slow mode. It is argued that wave coupling occurs due to non-uniformity in B, which on extended plasma sheet flux tubes gives rise to maximum plasma acceleration at the equator. This explanation is quantified with reasonable success by modelling the important vortex features using an acceleration source which is localised at the equator.

ACKNOWLEDGEMENTS

Above all I wish to thank my supervisor, Dr. David Southwood, for his guidance, understanding, and his constant example of what it means to be a physicist.

I gratefully acknowledge the financial support of the Science and Engineering Research Council during my studies.

My thanks go also to the participants of ISEE vortex workshops held at Imperial College and at Berkeley (California), all of whom contributed either directly or indirectly to views expressed here, while Drs. Ed Hones (Los Alamos National Laboratory) and Ted Fritz (Space Environment Laboratory, Boulder) deserve special thanks. Hones, Fritz and Dr. Chris Russell (UCLA) also receive grateful acknowledgement for supplying the ISEE data used in this work.

I am also indebted to Dr. Michael Rycroft for early help, not least in introducing me to Magnetospheric Physics.

Finally, I wish to thank my parents for their advice and encouragement throughout my education, with special thanks to my father, Mr. D.J. Saunders, for typing this thesis.

CONTENTS

		Page
ABSTRACT		3
ACKNOWLEDGEMENTS		4
CONTENTS		5
CHAPTER 1:	THE ISEE MISSION	7
1.1	Introduction	7
1.2	Orbits and separation strategy	10
1.3	The spacecraft and their payloads	15
1.4	This work in perspective	18
CHAPTER 2:	DATA HANDLING AND MANAGEMENT	20
2.1	Introduction and data acquisition	20
2.2	Data reduction	23
2.3	Data analysis software	26
CHAPTER 3:	HYDROMAGNETIC VORTICES - THE 11 DECEMBER 1977 EVENT	27
3.1	Introduction	27
3.2	Plasma and magnetometer data	28
3.2.1	Basic features	28
3.2.2	Mean field-aligned (MVA) coordinates	31
3.2.3	Pressures and Poynting flux	33
3.2.4	Discussion	37
3.3	Energetic charged particle observations	44
3.3.1	Introduction	44
3.3.2	Data	45
3.3.3	$\underline{E}$ x $\underline{B}$ drift	51
3.3.4	Oscillating ambient density gradient: a single instrument view	57
3.3.5	Wave-induced pressure gradients: a twin-instrument view	62
3.3.6	Flows parallel to $\underline{B}$	69

		Page
CHAPTER 4:	HYDROMAGNETIC VORTICES - FURTHER EVENTS	76
4.1	Introduction	76
4.2	28 December 1977 event	76
4.3	9 December 1977 event	87
4.4	19 December 1977 event - spacecraft/ ground comparison	89
4.5	Discussion	97
CHAPTER 5:	THEORETICAL INTERPRETATION	102
5.1	MHD modes in a hot isotropic plasma ..	102
5.2	Vortex wave mode identification	106
5.3	Coupling of Alfvén and slow modes	112
5.4	Energy dispersion	123
	5.4.1 Introduction	123
	5.4.2 Gaussian signal	126
	5.4.3 Impulse signal amd damping	130
	5.4.4 Discussion	134
5.5	Wave generation	135
CHAPTER 6	CONCLUSIONS AND SUGGESTIONS FOR FURTHER WORK	139
REFERENCES		145
APPENDIX A:	Spacecraft and initial orbit parameters	151
APPENDIX B:	The ISEE-1 and 2 experiments	152
APPENDIX C:	Software contributions	153
APPENDIX D:	Routine for converting to MVA coordinates	155
APPENDIX E:	Proof that equatorial acceleration need not give rise to energy dispersion	156

CHAPTER 1

THE ISEE MISSION

1.1 Introduction

History will confirm the launching of the International Sun-Earth Explorer (ISEE) mission, in the autumn of 1977, to be an important event in the study of near-Earth space plasma physics. Indeed, the quality and variety of the ISEE data suggest that the mission may have wider scientific benefits, extending to astrophysics and to laboratory plasma physics.

It is salutary to reflect in view of both the technological and the scientific progress made, that this event occurred within only two decades of the Explorer 1 spacecraft launch (in January 1958) which commenced our 'in situ' study of space plasmas. Subsequent to Explorer 1, a succession of 'lone' Earth-orbiting spacecraft steadily enlarged our understanding of how the Earth's magnetic field - or magnetosphere - is confined, shaped and differentiated by the solar wind. Before the ISEE programme became a reality, a detailed empirical knowledge of the main macroscopic features of the magnetosphere had emerged. On a microscopic scale, progress had been less rapid, and there remained (and still does even now!) much scope for discovery. The major problem, apart from deficiencies in instrumental resolution and spacecraft telemetry rate, which had beset the 'lone-spacecraft' investigators, was the space and time ambiguity

of identifying whether the spacecraft had passed through a particular feature or whether the latter had swept past the spacecraft. As a consequence, phenomena were known to exist without their dynamic properties being understood. The tackling of this problem was the prime motivation behind the ISEE project inception in 1971.

The ISEE mission is a three spacecraft programme undertaken jointly by NASA and ESA, and forms an integral part of the International Magnetospheric Study (IMS). A spacecraft pair, ISEE 1 and ISEE 2, is at the heart of the mission. These two spacecraft have carefully matched payloads and circulate through the magnetosphere a small and controllable distance apart. The advantages of such a system for studying magnetospheric dynamics is clear, and has been recognised since the discovery of the magnetopause by Explorer 12 (Cahill and Amazeen, 1963). From observing the difference in arrival time of the same phenomenon at the two spacecraft, the speed and the direction of movement of the feature can be identified, allowing spatial and temporal variations to be distinguished. This is, of course, not normally possible from a single platform. Although the ISEE investigators have been a little slow to utilise this long-sought for two-dimensional measurement capability (sometimes publishing with data from just one spacecraft!), several notable papers have appeared demonstrating the value of 'binocular vision' (e.g. Russell and Elphic, 1978; Paschmann et al., 1979; Sckopke et al., 1981; Hones et al., 1981; Sonnerup et al., 1981).

The greater resolution in time, direction and energy possible from the ISEE experiments in comparison with that

from previous magnetospheric spacecraft equipment has been another important feature of the mission. Indeed the benefits of extra resolving power have been adequately confirmed by the discovery of several unexpected phenomena (e.g. the tail 'vortices' (Hones et al., 1978), 'flux-transfer events' (Russell and Elphic, 1978), and the 'diffuse' and 'reflected' ion populations upstream of the bow shock (Gosling et al., 1978)). Interestingly, a feature of this increased sensitivity - the low instrument thresholds - has been achieved through a careful electrostatic and electromagnetic screening of the spacecraft. Overall, the ISEE payload is the most comprehensive and technologically advanced equipment package yet flown in studying the outer magnetosphere.

As many of the events which occur in and around the magnetosphere result from varying conditions in interplanetary space, the third spacecraft, ISEE 3, is stationed between the Sun and the Earth to monitor solar wind features about an hour before they sweep past the Earth. Further to this role, ISEE 3 is a mission in its own right, carrying instruments for studying various solar, interplanetary, cosmic ray and astrophysical phenomena. There is also a future possibility for employing ISEE 3 in a magnetospheric tail mission similar in concept to that planned for the shelved GEOS 3 project.

In theory therefore, ISEE-1 and 2 analyse the dynamic processes while ISEE 3 observes the trigger features in the solar wind. The potential exists to study both the cause and effect of magnetospheric processes as well as to make measurements in finer detail than has been possible before.

One also has the opportunity for comparing data with observations from other contemporary spacecraft such as GEOS-1 and 2, and with the measurements of various ground-based instruments deployed during the IMS. Such studies are under way.

1.2 Orbits and Separation Strategy

ISEE-1 and 2 were launched together on 22nd. October, 1977, into the same highly elliptic orbit having an apogee of 22·6 R_E (R_E = Earth radius), a perigee of 700 km, a 57 hour period and an inclination to the ecliptic of about 30°. Helped by slow changes in orbital parameters, particularly in inclination, which have occurred during the mission, this orbit has allowed most magnetospheric regions to be studied. The only areas not explored by ISEE are the far tail and the high latitudes; the latter including the important cusp/cleft region. One should note that the positive orbit inclination creates a northern hemisphere bias in the ISEE measurements, a feature which can prove to be a shortcoming in certain statistical studies.

Because the spacecraft orbit remains stationary in space during the Earth's rotation about the Sun, the line of apsides rotates annually through the magnetosphere as shown in Figure 1/1. One can see that apogees from the middle of August to late November always penetrate interplanetary space, whereas apogees in the tail occur during Spring.

As already emphasised, the separation between ISEE-1 and 2 is the key feature of the mission. An important aspect of this separation is its variability, which is

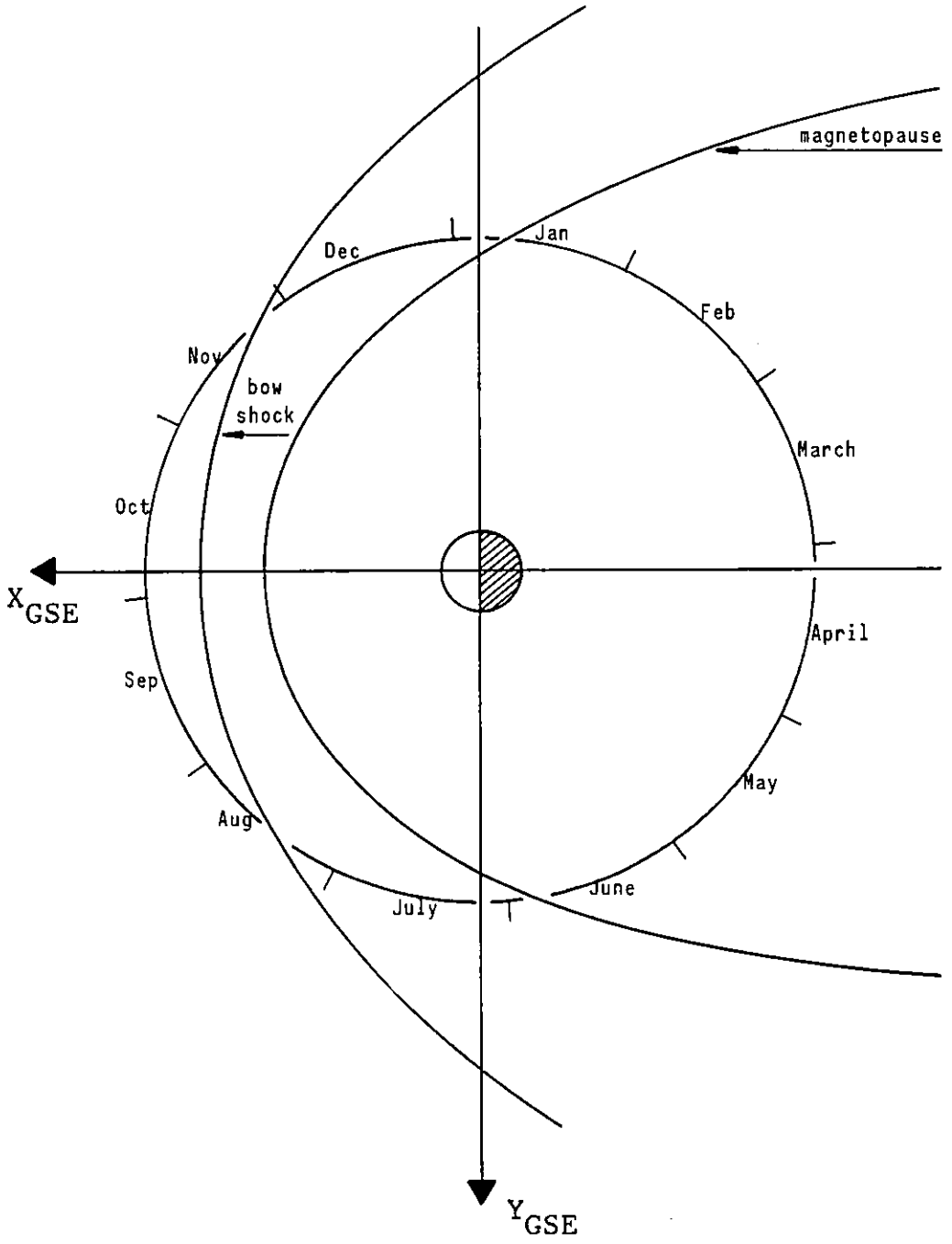

Figure 1/1. Ecliptic plane cross-section of the magnetosphere with the date circle representing the projection onto this plane of the line of the ISEE apsides for every month of the year. Apogee moves around the circle once in a year and lies outside the bow shock in the autumn and in the tail each spring.

controlled by a gas thruster on ISEE 2, although ISEE 1 is capable also of limited manoeuvres. This allows magnetospheric phenomena of different scale size to be studied, and furthermore, ensures that all instruments are put to optimum use, since particular experiments are better at measuring features of different size. Unfortunately, this system has two drawbacks. Firstly, for reasons of gas economy, the separation is only one dimensional - along the spacecraft orbit. However, as this direction is perpendicular to most magnetospheric boundaries, space and time variations can often be successfully studied. Secondly, spacecraft separations greater than 5000 km are frequently impractical because of priority problems with ground antenna tracking. This is due to the fact that large separations usually require two stations for successful tracking - a luxury which cannot always be guaranteed owing to the lower priority status accorded ISEE-1 and 2 as the mission progresses. Happily, intervals of large separation have been possible, most notably during the winter of 1978/79 when separations reaching 10,000 km were successfully tracked.

Although the spacecraft have an almost constant separation in time, because speed is a function of orbital position (Kepler's Second Law), their separation distance changes significantly around the orbit. Consequently separations are often expressed in terms of time. The history of the planned (until October,1981) and actual separations are shown in Figure 1/2. A spacecraft velocity of 2 km/s provides a reasonable guide to the corresponding separation distances (except when near

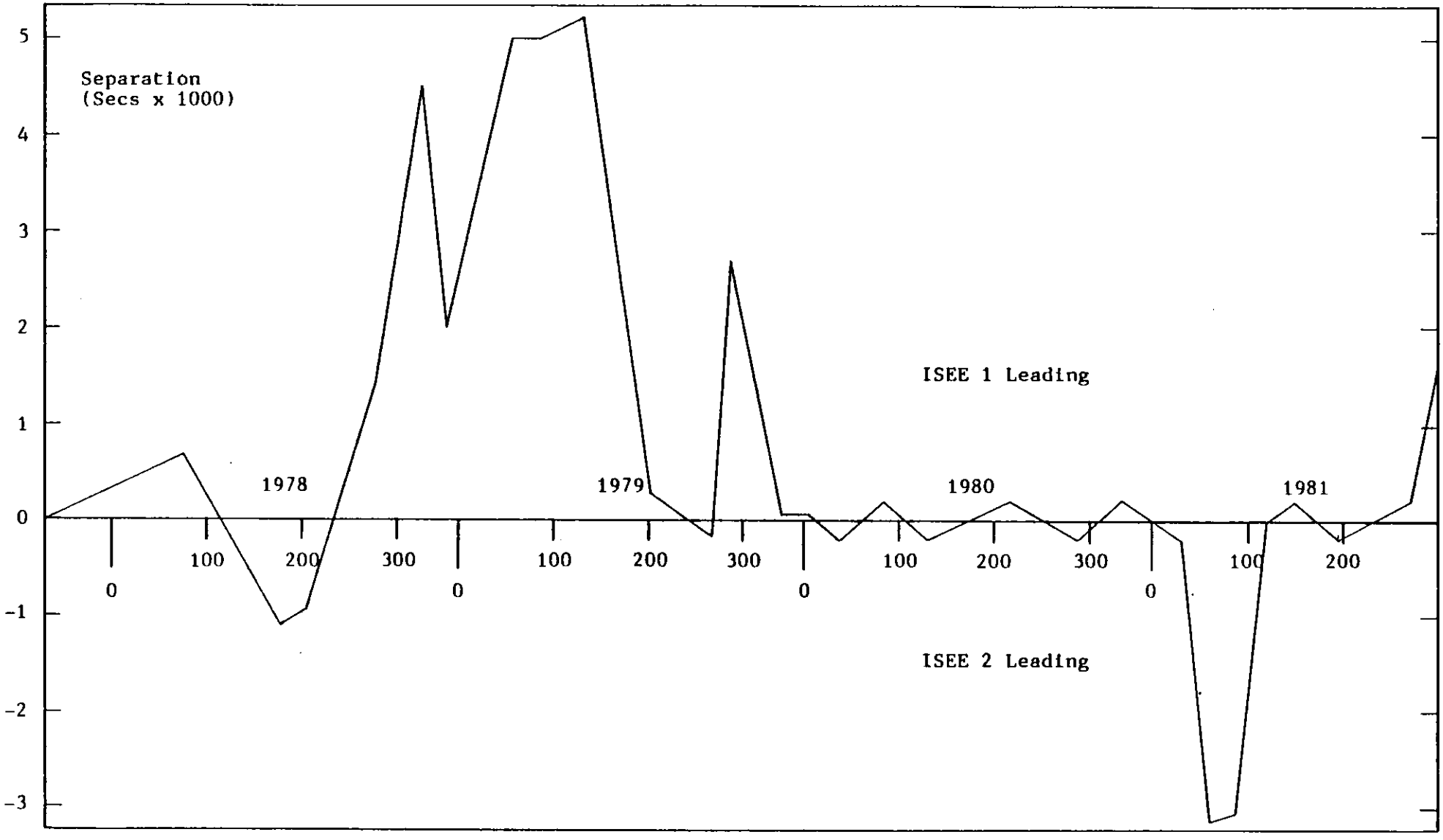

Figure 1/2. ISEE-1 and 2 separations from launch through to day 300 in 1981.

perigee). A noteworthy feature of this diagram is the regular change in identity of the leading spacecraft. The spacecraft 'flybys' which occur at times of effective zero separation are used for instrument recalibration and are most important.

The third spacecraft, ISEE 3, was launched on 12th. August, 1978, as soon after ISEE-1 and 2 as manpower deployment would allow. Injection into a six month period halo orbit about the sunward libration point was completed on 1st December, 1978. This position, about $235R_E$ upstream on the Earth-Sun line, is the most economical location, in terms of gas consumption, at which to place a satellite between the Earth and the Sun. Additionally, it was expected that at this large upstream distance, ISEE 3 would be 'uncontaminated' by particles and waves of magnetospheric origin; surprisingly this has not been the case (e.g. Durney, 1980). An orbit about the sunward Lagrangian point, rather than placement at this position, was necessary to avoid solar radio emission swamping the spacecraft telemetry. A halo-shaped orbit was chosen (again for fuel economy reasons), with its plane normal to the Earth-Sun line and its major axis in the ecliptic. It is worth noting that at its orbit extremity, ISEE 3 is 28° away from the Sun, or equivalently, departs from the Sun-Earth line by over $100R_E$. Such a large offset clearly reduces the effectiveness of ISEE 3 as an accurate monitor of the solar wind and IMF immediately upstream from the Earth. Indeed, Russell et al. (1980) have confirmed this to be the case

from an initial correlation of ISEE-1 and 3 magnetometer data.

1.3 The Spacecraft and their Payloads.

ISEE 1 and ISEE 3 were built by NASA as their main contribution to the IMS. They are similar in size and design, and are based on the old IMP series. ISEE 2 is smaller and was constructed by ESA specifically for the mission. The main spacecraft parameters are listed in Appendix A. The spacecraft are spin stabilized with their spin axes perpendicular to the ecliptic to within ± 1° (ISEE 2's precision is ± 3°) and pointing north. To allow all-round viewing for some experiments, the spin rates of the ISEE pair differ slightly (19·7 ± 0·05 revolutions per minute for ISEE 1 and 19·8 ± 0·1 rpm for ISEE 2). Although two telemetry rates are available, the higher rate (by a factor of 4) can only be employed for ISEE-1 and 2 about 20% of the time. This telemetry limitation is unfortunate since it reduces considerably the performance of every instrument. Incorporated into the design of all spacecraft is the important technique pioneered by GEOS, of having the entire outer spacecraft surface conducting. This ensures the spacecraft exterior is an equipotential so eliminating any differential charging and consequent spin modulation in measurements from some of the instruments.

The three spacecraft carry a total of 33 experiments with investigator participation from 33 institutes in 8 countries. The experimental payloads for ISEE-1 and 2 are listed in Appendix B, together with the name of the

principal investigators and their affiliations. Details of ISEE 3's experimental complement, together with further general information on this spacecraft, can be found in Durney (1977) and Ogilvie et al. (1977). The eight instruments on ISEE 2 are matched by similar, complementary, or in two cases, almost identical experiments on ISEE 1. The latter, in addition, carries six extra experiments, including detectors for measuring D.C. electric fields and for determining plasma mass composition.

Three key ISEE instruments are the UCLA fluxgate magnetometers, the Los Alamos National Laboratory (LANL)/ Max Planck Institute at Garching (MPI), fast plasma analysers, and the NOAA Space Environment Laboratory at Boulder/Max Planck Institute at Lindau (MPAe), medium energy particles experiments. As observations from these experiments, particularly those from the magnetometers, will feature prominently in subsequent Chapters, a brief knowledge of instrument characteristics will be useful in understanding the data to be presented.

The magnetometers on ISEE-1 and 2 are virtually identical, being of triaxial fluxgate design, and having two ranges: $\pm$ 8192γ and $\pm$ 256γ (1γ = 1nT). In the latter range, the absolute field and field direction are accurate to 0·1γ and 0·1° respectively. Data are available at three temporal resolutions: low resolution, 64s averages; medium resolution, 12s averages; and the full resolution which varies from $\frac{1}{4}$ to $\frac{1}{32}$ of a second per sample. The magnetometer recordings presented in this report are 4s data produced by overlapping the 12s averages by two thirds. A thorough description of the instrument can be found in Russell (1978).

The identical 'Fast Plasma Experiments' on ISEE-1 and 2 consist of three quadrispherical electrostatic analysers. Particles are measured in the energy per charge range from 11 eV to 20 keV (electrons) and from 70 eV to 40 keV (ions). During high bit rate transmission, complete 2D distributions are repeated every 3s, whereas at low bit rate the repetition cycle is 12s. For each data telemetry rate the corresponding 3D distribution takes four times longer to compile. Unfortunately, this good time resolution has to be balanced against incomplete spatial resolution, since the detectors only measure flows within ± 55° of the spacecraft spin plane (approximately the ecliptic). Further information on the LANL/MPI instruments and on the data reduction procedures employed in calculating moments of the distribution function, may be found in Bame et al. (1978) and in Paschmann et al. (1978).

The ISEE 'medium energy particles experiments' (MEPE) consist of a focusing magnet and solid state detectors which separate and measure, in sixteen energy channels, ions from 24 keV to 2 MeV and electrons from 24 keV to 1 MeV. The spectrometers on the two spacecraft differ in their temporal and angular resolving power. Whereas the ISEE 2 detector has a constant look angle (82°) to the spin axis, the ISEE 1 detector scans in polar angle relative to the spin axis, covering the angular range from 10° to 170° in 12 spins at which point the scan is reversed. The ISEE 1 experiment therefore samples the 3D unit sphere every 36s. In comparison, the ISEE 2 spectrometer samples basically

only in the ecliptic plane, but can do so in just 3s. Williams et al. (1978) describe both MEPE's in detail.

Upon reaching its nominal three year lifetime in October, 1980, with all spacecraft continuing to operate successfully, the mission was extended. Overall the project has had a less than average number of instrument failures; faults have developed, but in most cases they have proved only partial so that experiments have continued to send back worthwhile results. Although funding allows for tracking until at least 1983, the mission can not extend past 1987 as the decrease in perigee altitude of ISEE-1 and 2 will cause them to 'burn-up' in the atmosphere. By then ISEE will have been superseded by the next major magnetospheric mission, AMPTE (Active Magnetospheric Particle Tracer Explorers).

1.4 This work in perspective

Following the description of the ISEE spacecraft mission, the data from which will form the basis of this report, now appears an appropriate moment to place the subsequent Chapters in context. This thesis interprets through data analysis and theory a specific magnetospheric phenomenon: the tail plasma vortices - an unexpected ISEE discovery first reported by Hones et al. (1978).

As data reduction and handling have formed an integral part of this study, and as on behalf of the ICST Space Physics Group I have had the responsibility during my research for processing and managing all incoming ISEE data, Chapter 2 briefly describes the work undertaken in this regard.

The 'meat' of the thesis is contained in Chapters 3 - 5. By synthesizing data from several ISEE experiments, Chapter 3 presents a detailed analysis of the initial (11th December 1977) vortex event reported by Hones et al. (1978). Important features of the event are emphasized, especially the significant field-aligned flow and the antiphase gas and magnetic pressure perturbations. The interpretation of the event suggested by Fritz (1981) using MEPE data alone is shown to be incorrect, and an alternative explanation is given for these data.

To demonstrate that the 11th December 1977 vortex was neither atypical nor uncommon, Chapter 4 details the characteristics of three similar vortices recorded within three weeks of and at similar locations to the initial study. These include one event where magnetic pulsations were observed on the ground in association with the vortex in space.

Chapter 5 presents a theoretical interpretation of the vortex phenomenon. After reviewing MHD wave theory for a hot and isotropic plasma, it is shown how, in many respects, the vortex characteristics are consistent with an MHD slow mode wave. However, the direction of phase motion across the field implied by the energetic particle data and the wave polarisation, indicates that there is coupling with the Alfvén mode. It is suggested that the wave coupling occurs due to non-uniformity in B and is associated with maximum plasma acceleration at the equator; an explanation which is quantified with reasonable success by modelling the important vortex features.

Conclusions and suggestions for further research are discussed in Chapter 6.

CHAPTER 2

DATA HANDLING AND MANAGEMENT

2.1 Introduction and Data Acquisition

During my research I have had the responsibility for managing many of the ISEE data interests of the ICST Space Physics group. This work, although time consuming and often mundane, has provided me with useful training and experience in the organisation of a scientific data system. It has allowed me to foster relations with other institutes, and, most importantly, has instilled a scepticism for the 'face-value' accuracy of spacecraft data and results obtained through computer analysis. As an additional benefit, it has vastly improved my ability in computer programming!

Since ISEE data handling and management has been an integral part of my day, it seems appropriate to detail briefly the nature of the work involved. The purpose of this Chapter is to describe both this work and also the part played by Imperial College within the system of ISEE data distribution.

As Dr. Peter Hedgecock was initially co-investigator on the ISEE-1 and 2 magnetometer experiment, with responsibility subsequently transferred to Dr. David Southwood, the ICST Space Physics group routinely receives ISEE magnetometer data from UCLA. In the course of my research, working relations have also been established with the groups at Los Alamos and at MPI (Garching), thereby allowing selected intervals of ISEE plasma data

to be acquired. Contacts with several other ISEE investigators have also been developed, initially by correspondence, but following two workshops which I helped organize in connection with the 11th. December, 1977 tail vortex event (see Chapters 3 and 5), these contacts are now on a good personal basis. The workshops were held at ICST (August, 1981) and at Berkeley in California (December, 1981).

The position of Imperial College in the ISEE data handling system is shown in flow diagram form in Fig. 2/1. The upper part of the Figure shows that the methods for retrieval, initial processing and dissemination of ISEE data are somewhat archaic, owing to the fact that ISEE is a 'low cost' mission. Compared with its contemporary, GEOS, for example, data are not normally available in real time, and telemetry rates from spacecraft to ground are, at best, a factor of 4 less and usually 16 times smaller. Another unsatisfactory feature of the ISEE data system is the time taken for despatch to principal investigators, which is at least a month after recording. Release to the general scientific community occurs later, and is via a 'pool' tape (recently superseded by 'pool' microfilm) which carries compressed data from most of the mission experiments. This data, received routinely at ICST, is useful for identifying interesting events such as boundary crossings, but is unsuitable for studies requiring good time resolution. To undertake such work, one has to solicit the appropriate principal investigator for data at higher resolution.

The lower part of Fig. 2/1 summarizes the major

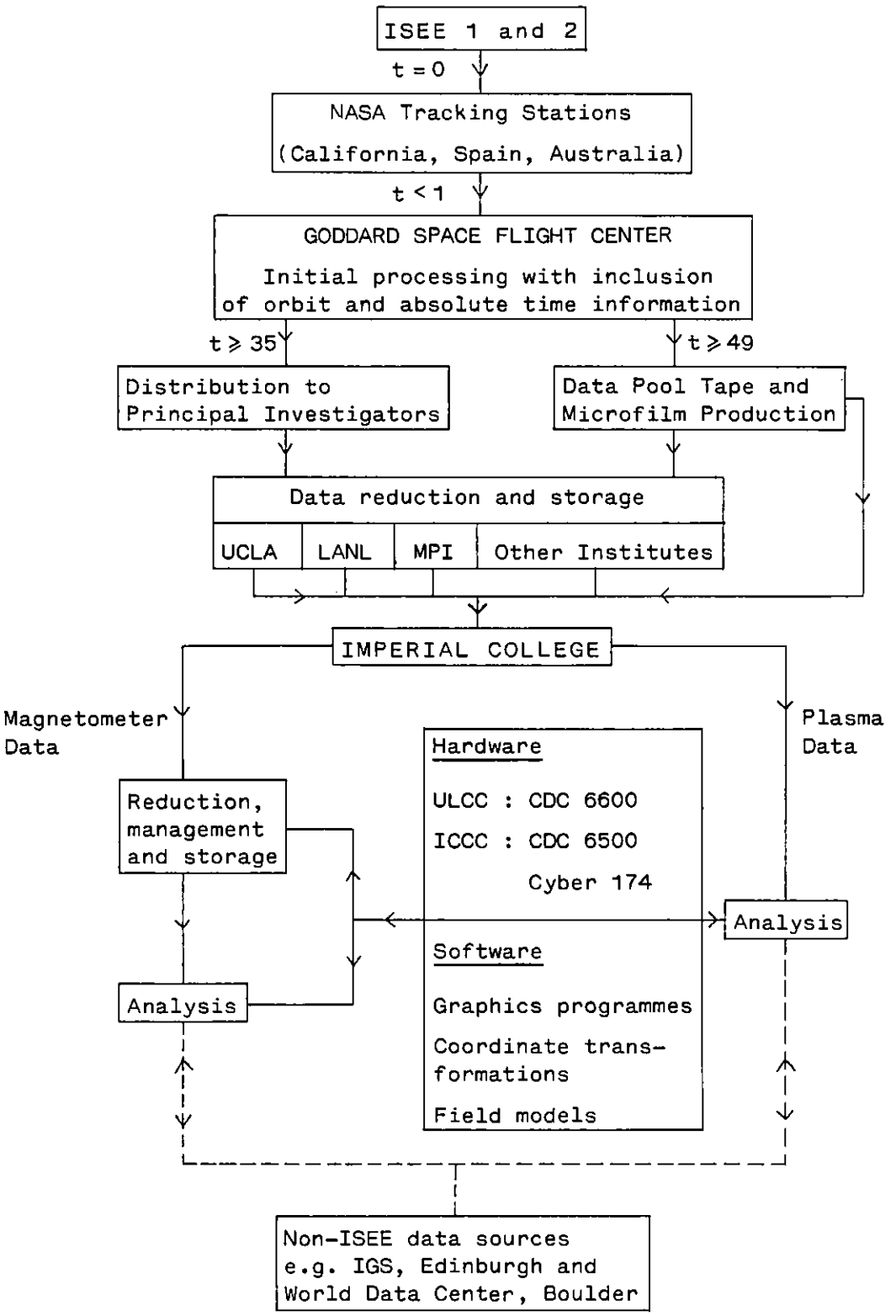

FIGURE 2/1 Block diagram of the ISEE data flow and analysis system.

Times, t, are in days subsequent to initial recording.

features of the ISEE data processing and analysis work performed at ICST. Aspects of this work will now be discussed.

2.2 Data Reduction

The processing of incoming data forms the most important part of my ISEE data handling duties. All data is digitised on magnetic tape, and up to 100 tapes can be received a year. Although the plasma data are fully reduced, the magnetometer measurements require further processing. The procedures and software for achieving this were originally developed by Dr. Peter Hedgecock and Mrs. Anne Evans, but following improvements by UCLA in their methods for generating data tapes, I updated the systems approximately a year ago. The main procedures now associated with our data processing are outlined in block diagram form in Fig. 2/2 and are also described below.

The data reduction and the bulk of the data analysis take place at the University of London Computer Centre (ULCC) rather than at the Imperial College Computer Centre (ICCC). Reasons for this are partly historical, but the ULCC complex (based on CDC 6400,6600 and 7600 machines) has roughly four times the computing turnaround of ICCC (centred on CDC 6500 and Cyber 174 hardware). This extra computing capacity, coupled with generous tape storage facilities, are the main reasons for using ULCC.

Each UCLA data tape contains recordings from one spacecraft for up to eleven days. Three types of information are included: low (64s - averaged) and medium

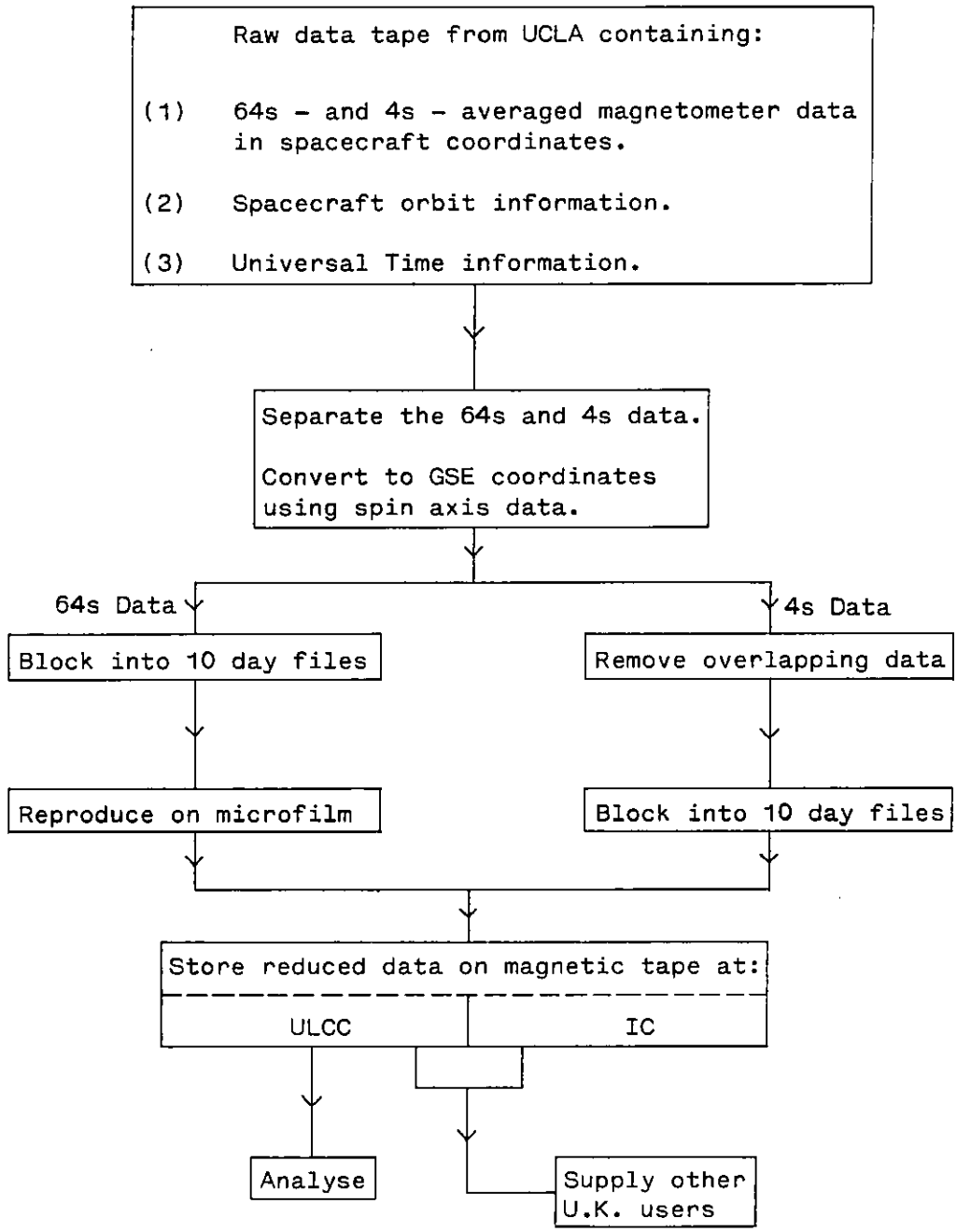

FIGURE 2/2 Aspects of the ISEE magnetometer data reduction.

(12s-averaged) resolution magnetometer data, spacecraft position vectors, and timing information. The 12s resolution B data are overlapped by two-thirds, and so are received as 4s data. The raw data are in 'spacecraft coordinates' (defined relative to the spacecraft spin axis) and have to be converted to a more useful coordinate system. The GSE system (see Russell (1971) for a description of this and other coordinate systems) is used to achieve this. Information on the spin axis orientation necessary to perform this transformation, together with various other useful spacecraft attitude and orbit information, are obtained from microfiche listings produced by UCLA. It should be noted that the 64s and 4s data are processed separately. Various ordering and tidying procedures then follow (e.g. the removal of overlapping data, and the blocking of data into suitable length files). To provide a rapid means of surveying the data for interesting events, the reduced 64s measurements are routinely displayed in GSM coordinates on microfilm for subsequent hard-copying and filing.

The processed data is stored on magnetic tape, either in the ULCC tape library (if required for ongoing analyses), or in the Space Physics group tape library at Imperial College. More than 300 tapes are presently under management, of which approximately 60 are stored semi-permanently at ULCC. A further aspect of managing the ISEE magnetometer data reduction is the responsibility for supplying processed data to other U.K. users (e.g. the Institute of Geological Sciences (IGS) at Edinburgh, and the University of York).

2.3 Data Analysis Software

With the increasing sophistication of magnetospheric spacecraft measurements, it is essential to have a thorough and flexible software back-up to assist in data analysis. Having been involved with magnetospheric spacecraft data for more than a decade, the ICST Space Physics Group has a well-developed library of programmes and subroutines for analysing data. This includes contributions from my own data analysis work, two examples of which (a routine for converting to Boundary Normal (LMN) coordinates for use in studying the magnetopause, and a graphics programme for plotting ISEE-1 and 2 data simultaneously) are described briefly in Appendix C.

CHAPTER 3

HYDROMAGNETIC VORTICES - THE 11th DECEMBER 1977 EVENT

3.1 Introduction

The observation of intervals of apparent vortical or circulating plasma flow by Hones et al. (1978) was an unexpected ISEE discovery. In a more comprehensive study, Hones et al. (1981) report the detection of 169 vortical flow events during the first 19 months of ISEE operation; an average of two events every three orbits. These vortices all occurred in the plasma sheet and magnetopause boundary layer regions tailward of the dawn-dusk meridian. Their distinguishing characteristic was a solar ecliptic plasma flow longitude which rotated through 360°, often repeatedly, (in one instance sporadically for 9 hours), with rotation periods of between 5 and 20 minutes. The flow rotation (viewed from above the ecliptic) was clockwise in the morningside plasma sheet and counterclockwise in the eveningside. In the magnetopause boundary layers the rotation sense was reversed from that in the adjoining plasma sheet. The occurrence of vortical flow was independent of geomagnetic activity.

This chapter investigates the initial plasma vortex event catalogued by Hones et al. (1978). A detailed study is presented using plasma and magnetometer data from both ISEE spacecraft and energetic particle and electric field data from ISEE 1. The event occurred on 11th. December, 1977, during the recovery phase of a magnetic storm,

when the spacecraft were outbound at $8{\cdot}8R_E$ in the dawn plasma sheet (see Table 3/1). Although transient in comparison with other vortex events it did exhibit clear rotation, and as we show in Chapter 4, it was not atypical.

3.2 Plasma and Magnetometer Data

3.2.1 Basic features

ISEE 2 vortex event magnetic field and 3D thermal plasma data are displayed in Fig. 3/1 using GSE coordinates. Since telemetry was at high bit rate the plasma data have 12s resolution - the same time resolution as the $\underline{B}$ recordings. The rotation in plasma flow longitude over two cycles from 23.10 to 23.22 U.T. is striking. Not surprisingly Hones et al. (1978,1981) interpreted this rotation in terms of a vortex motion; though since curl $\underline{v}$ can not be measured they have not proved it is a vortex.

Since the flow rotation occurred in a highly conducting collisionless plasma, one would expect the magnetic field to twist around in response; indeed one might expect a transverse hydromagnetic wave. Such simple expectations were dashed, for as Fig. 3/1 shows, although field perturbations occurred in conjunction with, and possessed the same 6-minute timescale as, the flow rotation, the field direction did not rotate through 360°. Instead, surprisingly, field strength changes occurred with the peak-to-peak field compression exceeding a third of the background field strength.

Another unexpected feature was the tail-like nature of the background field, which almost lay in the ecliptic plane - a 24° distortion from the Peter Hedgecock 1977B field model (unpublished) prediction for $K_p > 2$ conditions (see Table 3/2). This is important because since the

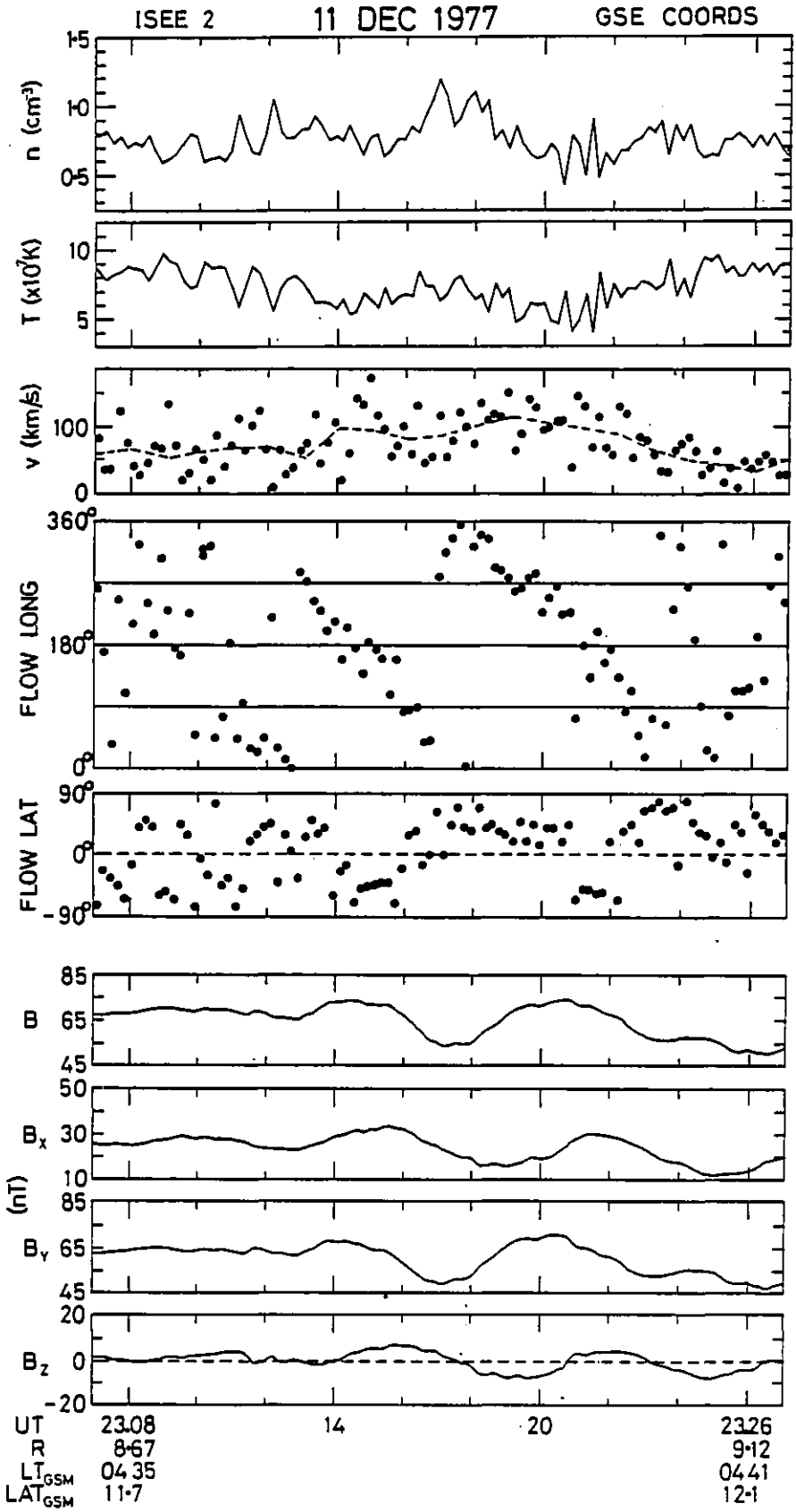

FIGURE 3/1. ISEE 2 thermal plasma and magnetometer data for the 11 December, 1977 vortex event, with components of the flow and field displayed in GSE coordinates. Spacecraft position is shown at the base of the diagram in terms of radial distance (R), GSM coordinate local time (LT_{GSM}) and latitude (LAT_{GSM}). The plasma parameters are, from top to bottom: proton density (n), proton temperature (T), flow speed (v) with the dashed line representing a 2 minute running average, flow longitude and flow latitude. The lower four panels show the strength (B) and components of the magnetic field.

flow rotated in the ecliptic plane, part of the flow rotation must have been field aligned. This surprising feature does not agree with the simple Kelvin-Helmholtz interpretation of the vortices envisaged by Hones et al. (1981) using plasma data alone.

Density and temperature perturbations were also notable features in the plasma data during the vortical flow. These were in phase and produced a plasma pressure perturbation in antiphase with the field strength oscillation; this will be a point of significance when we consider the direction of energy flow during the disturbance (Section 3.2.4.), and later when we investigate the vortex wave mode (Chapter 5). The presence of a temperature perturbation, δT, is also a point of some importance. δT was related to the density perturbation, δn, and the background density, n, and temperature T, by:

$$\frac{\delta T}{T} \; : \; \frac{\delta n}{n} \sim 2:3 \quad .$$

For an adiabatic process:

$$\frac{\delta T}{T} = (\gamma-1)\frac{\delta n}{n} \quad , \qquad (1)$$

so γ, the ratio of specific heats, was of order $5/3$ during the vortex event. This means that the plasma in the spacecraft vicinity was behaving like a gas with three degrees of freedom. In other words the plasma pressure remained isotropic during the rotational motion. Distribution function plots confirm this isotropy in plasma pressure (Hones, ICST vortex workshop, August 1981).

3.2.2 Mean field-aligned (MVA) coordinates

For the detailed study of wave phenomena in space it is useful to employ a coordinate system aligned with the background (or average) magnetic field direction. Such a system, described by Hedgecock (1976), is used here and called mean vector aligned (MVA) coordinates. A listing of the subroutine conversion to MVA coordinates (written by Peter Hedgecock) is given in Appendix D. This shows the $+Z_{MVA}$ axis is aligned with the mean field direction; with Dipole VDH coordinates as the subroutine input, X_{MVA} is outward in the magnetic meridian defined as the plane containing Z_{MVA} and the radius vector; Y_{MVA} completes the right-hand orthogonal set.

As the mean field direction may vary during the interval of study, the MVA plots presented here had their Z - direction defined by a running mean method using a low pass digital cosine convolution filter. With 4s samples, the filter cut-off amplitude response fell from 99% at a period $\sim$ 3000s to 2% at $\sim$ 750s. The MVA - coordinate transformation of each vector was performed in such a way that the Z_{MVA} axis followed the vector direction specified by the filtered data sequence. As an added convenience, variations in background field magnitude were removed from the Z_{MVA} magnetometer plots by subtracting the magnitude of the vector filtered sequence.

ISEE-1 and 2 magnetometer data and ISEE 2 plasma data for the vortex event are displayed in MVA coordinates in Fig. 3/2. The Z_{MVA} direction for each spacecraft was calculated from the field at that spacecraft. From the foregoing, b_x and b_y are the transverse field perturbations

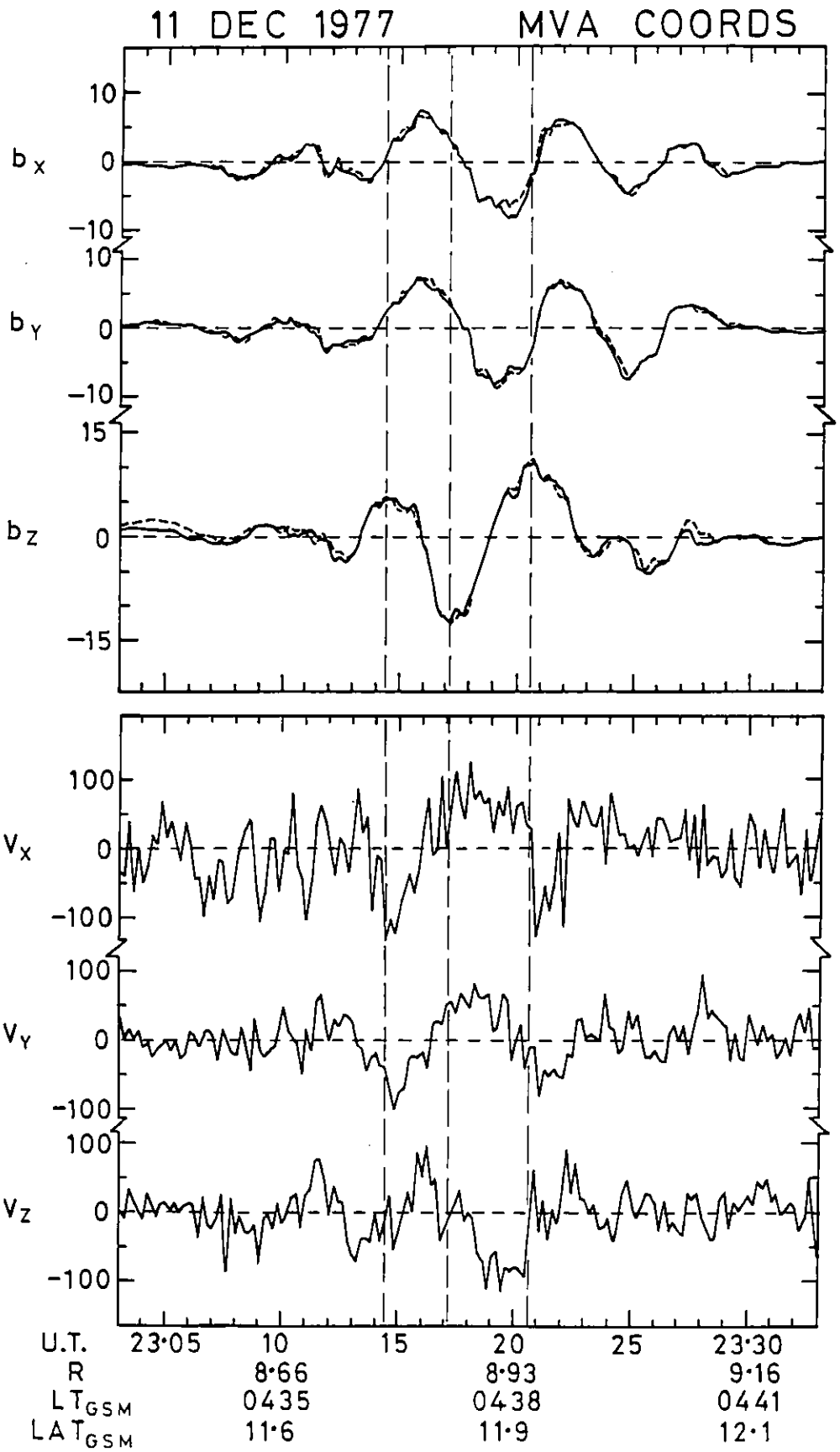

FIGURE 3/2. Magnetometer and thermal plasma observations expressed in a field-aligned (MVA) coordinate system (see text for discussion). The magnetic field recordings (in nT) are shown for both spacecraft, with ISEE 1 data shown as the solid trace, while the thermal flow measurements (in km/s) are data from ISEE 2.

with X positive northwards and Y positive sunwards. Previously deduced vortex features are now clear, especially the nett v_Z indicative of plasma 'sloshing' along the magnetic field. Other characteristics to note are:

(a) b_X and b_Y (and similarly v_X and v_Y) were in phase indicating the wave had a linear transverse polarisation. Although not apparent in Fig. 3/2, the polarisation directions of $\underline{b}_\perp$ and $\underline{v}_\perp$ in fact differed by 10°. We believe this offset is probably an instrumental effect; the LANL/Garching detectors do not measure perfectly flows of high solar ecliptic elevation and this event had a significant v_Z GSE - component.

(b) b_Z was in approximate quadrature with $b_\perp$ the perpendicular field perturbation (it led in phase by ∿ 60° to 90°).

(c) $b_\perp$ led $v_\perp$ in phase by ∿ 135°.

(d) b_Z led v_Z in phase by $\geq$ 90°.

(e) the 'break-up' of flow rotation was synchronised with the disappearance of b_Z rather than $b_\perp$.

Fig. 3/2 also shows no evidence for phase difference in the low frequency signal between the two spacecraft. The spacecraft were separated by about 800 km.

3.2.3 Pressures and Poynting Flux

The magnetic pressure, $B^2/2\mu_0$, and scalar plasma pressure, p, for a 90 minute interval encompassing the vortex event are displayed in Fig. 3/3. p was calculated assuming isotropy. The magnetic pressure is shown for both ISEE-1 and 2; ISEE 1 is the solid line. The plasma β (ratio of plasma to field pressure) and the total pressure

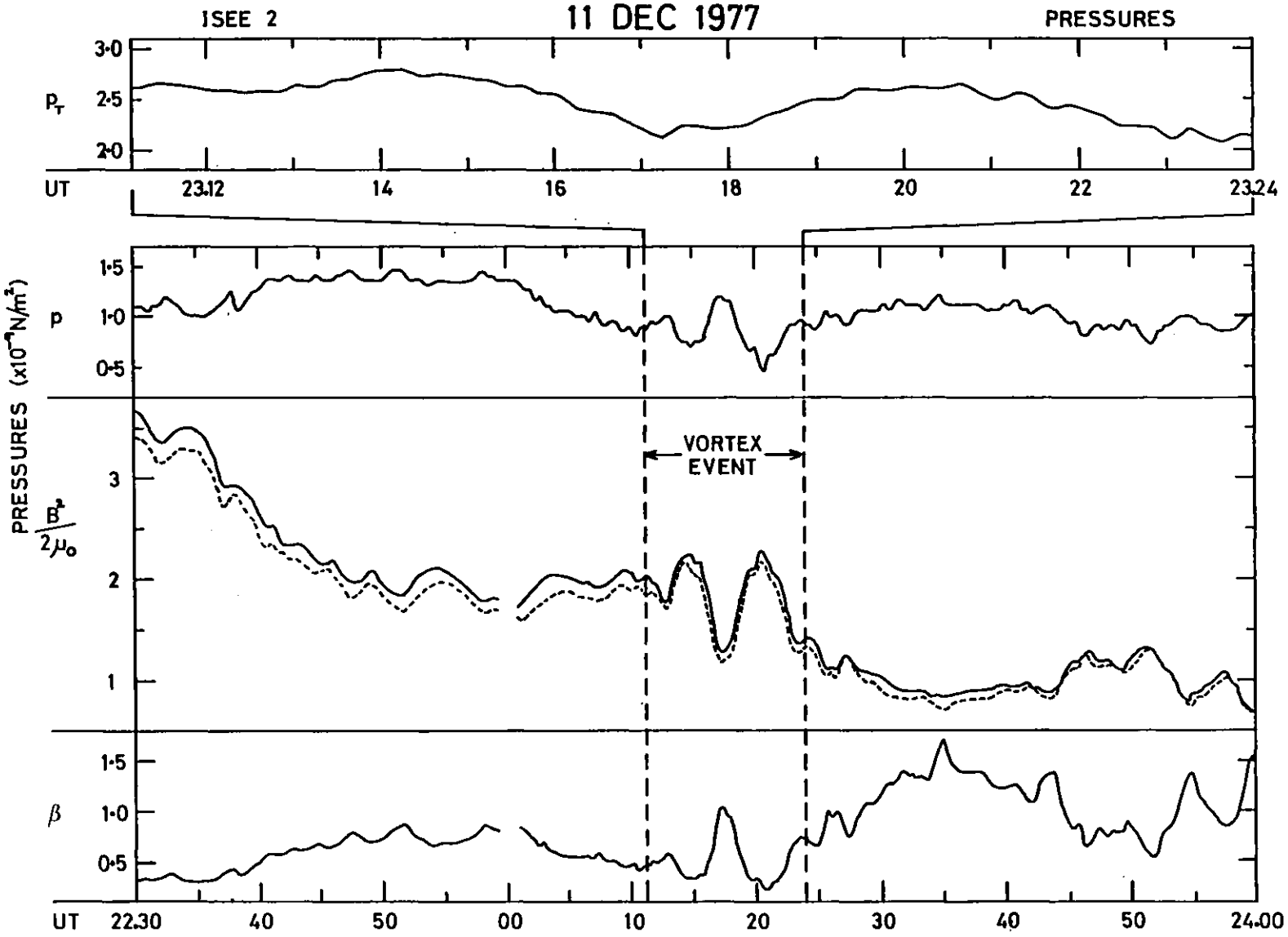

FIGURE 3/3. ISEE 2 pressure data for the 11th December, 1977 vortex. The lower three panels show the scalar thermal (70eV to 40keV) proton pressure (p), magnetic pressure ($B^2/2\mu_0$) and plasma β for 90 minutes overlapping the event. The field pressure is displayed for both spacecraft, with the solid line representing ISEE 1. The top panel shows the total pressure ($p+B^2/2\mu_0$) during the interval of vortical flow.

$p_T (= p+B^2/2\mu_o)$ are also included, though the latter is shown only for the vortex event. Prior to and during the event, oscillations occurred in both the plasma and magnetic field pressures. These oscillations were in strict antiphase, had about a six minute period, and maximized in amplitude during the rotational motion. The proton (70 eV to 40 keV) and electron (11 eV to 20 keV) pressures oscillated in phase,with the electron pressure perturbation (not shown) an order of magnitude smaller than the proton pressure perturbation.

Since the field pressure perturbation exceeded the plasma pressure perturbation by a factor of two, pressure balance was not maintained. The contribution from energetic (>40 keV) and cold (<70 eV) ions, neglected in the LANL/MPI plasma pressure calculation, should be small. Our inspection of the Boulder/Lindau ISEE 1 MEPE data confirms this was the case for the high energy range where the pressure contribution was ∿10%. Assuming the continuum radiation cut-off occurred at the local plasma frequency, the ISEE plasma wave experiment (R.Anderson, private communication) shows that cold particles also made little contribution to the total density (and thus to the pressure).

The Poynting vector $\underline{S}$ is well known for describing electromagnetic energy flux. In ideal hydromagnetics

$$\underline{S} = (\underline{v}\ (\underline{B}.\underline{b}) - \underline{B}(\underline{v}.\underline{b}))/\mu_o$$

where $\underline{b}$, $\underline{B}$ and $\underline{v}$ are the magnetic perturbation, background field and plasma velocity; μ_o is the permeability of free space. The computed Poynting flux during the vortex event is shown in MVA coordinates in Fig. 3/4. Since the

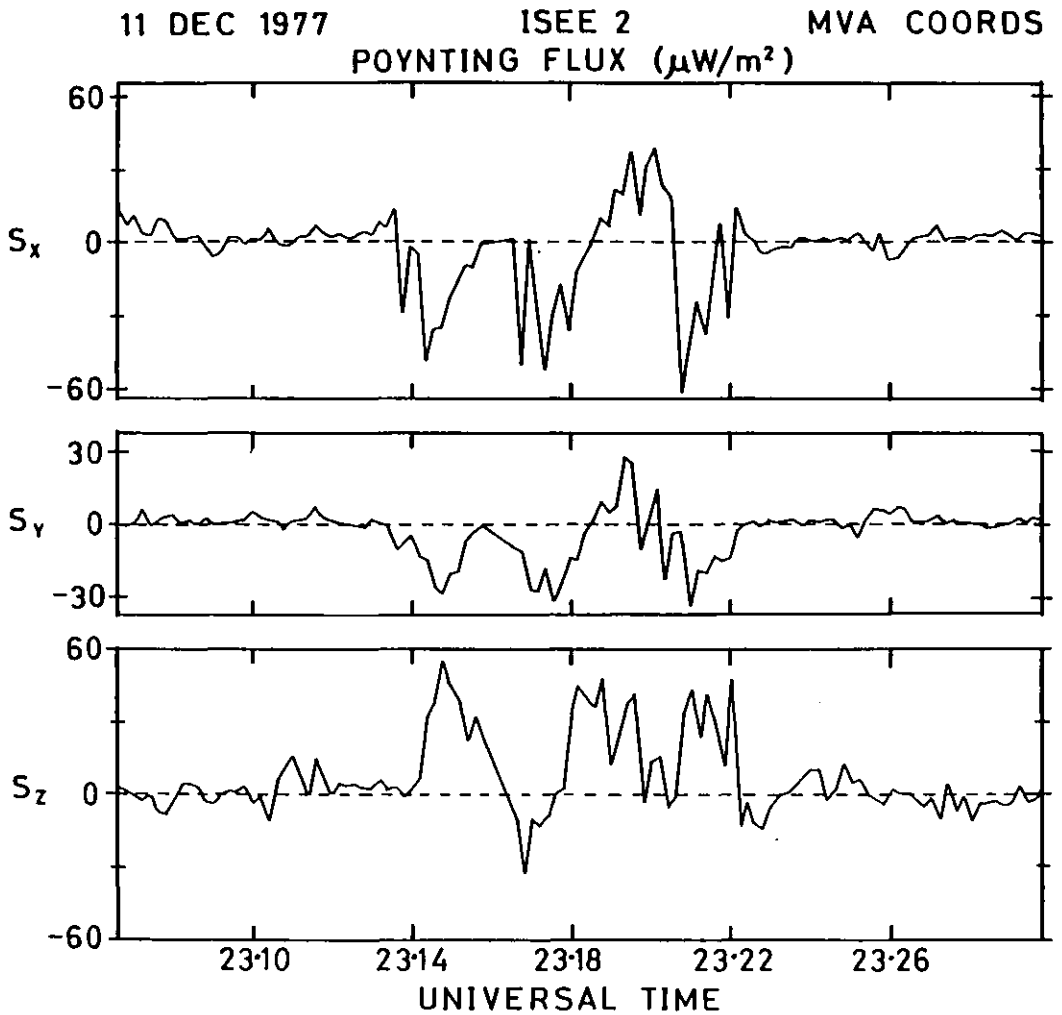

FIGURE 3/4. Poynting flux computed assuming ideal MHD and displayed in field-aligned coordinates.

spacecraft were above the neutral sheet the field pointed Earthward. Clearly there was a nett Earthward field-aligned electromagnetic energy flux during the event. The nett perpendicular Poynting flux was tailwards and southwards.

3.2.4 Discussion

There can be little doubt that the vortex is hydromagnetic in nature. Hydromagnetics is valid provided time and space scales are long compared with the scales of ion gyration. From the ISEE ion mass spectrometer we know that H^+ was the major plasma constituent during the event (Lennartsson et al., 1979 - also, see Table 3/2). In the 65γ background field a thermal (5·5 keV) proton had a Larmor radius of 160 km. Since we show later this event had a wavelength perpendicular to $\underline{B}$ of $(5\pm1) \times 10^3$ km, its scalesize was clearly several thermal proton gyroradii, though only a few gyroradii at higher proton energies. In addition, the six minute period of the flow and field oscillation was more than 300 times a gyration period, and was probably comparable with the thermal bounce period between hemispheres.

The accepted approach for discussing hydromagnetic oscillations in the magnetosphere with periods greater than about a minute is in terms of Alfvén waves with standing structure along entire magnetospheric flux tubes (Lanzerotti and Southwood, 1979). This is because the frequency is so low that the Alfvén wavelength is comparable to the entire flux tube length. This was also the case here since the local Alfvén speed of 1300 km/s (Table 3/2)

and wave period of 6 minutes give an Alfvén wavelength, λ_A, of order 5 x 10^5km. or $70R_E$; a reasonable value for the local flux tube length. In this respect the hydromagnetic vortex did resemble a standing Alfvén wave.

In other respects the event was clearly not a pure standing Alfvén wave. The signals were not transverse polarised; a substantial compressional magnetic oscillation was present. In addition, because the Alfvén mode is guided by the field, provided the ionospheres at each end of the flux tube are effective at reflecting the wave, the resulting standing wave should have zero nett field-aligned Poynting flux. This signal did not exhibit this characteristic as Fig. 3/4 shows.

A strong compressional magnetic component in low frequency signals has been reported elsewhere, e.g. at synchronous orbit by Barfield and McPherron (1972), Hughes et al. (1979) and Kremser et al. (1981), and at $8-12R_E$ near dusk by Hedgecock (1976). However, the polarisation in the plasma sheet event here differed by being linear transverse to $\underline{B}$. At synchronous orbit the plasma pressure and ambient magnetic pressure are often comparable. This $\beta \sim 1$ circumstance also applied here (see Fig. 3/3). That the plasma and magnetic pressures oscillated in antiphase was not surprising on dynamic grounds. It is, for example, to be expected in the MHD slow mode; a point we shall return to later.

For the moment, let us note that the size of the plasma pressure perturbation indicates we are observing a wave with hot plasma properties. Thus we should be cautious in interpreting the Poynting electromagnetic flux as the

total wave energy flux. The wave may have had a significant heat flux associated with it. Although computation of the heat flux magnitude requires a detailed knowledge of the particle distribution, one can deduce its direction from the information presented here. Fig 3/2 shows the compressional magnetic perturbation, b_z, was in antiphase with v_z, the field-aligned plasma velocity. Fig. 3/3 shows the plasma pressure change, δp, was in antiphase with b_z so the mean value of $v_z \delta p$, $\langle v_z \delta p \rangle$, was positive. As the parallel heat flux should be proportional to $v_z \delta p$, the nett heat flux parallel to $\underline{B}$ was Earthward during the event. This energy flux therefore added to the field-aligned Poynting flux, S_z, and was of comparable magnitude.

Since the total field-aligned energy flux was Earthward, it seems the energy supply was equatorward of the spacecraft. The absence of a significant return flow indicates this energy was absorbed somewhere Earthward of the spacecraft, possibly by Joule heating in the ionosphere. At the prevailing 0430 local time, ionospheric conductivity should be low, and consequently Alfvén wave reflection imperfect (e.g. see Newton et al., 1978). Greenwald and Walker (1980) point out that the energy flux carried by hydromagnetic waves into the auroral zone can be appreciable. For the event here, the energy flux of $\sim 3 \times 10^{-5}$ W/m^2 measured at the spacecraft in a 65γ field corresponds to an energy flux in excess of 10^{-2} W/m^2 when mapped along the field to the ionosphere. This would be comparable with auroral energy deposition rates (see e.g. Hultqvist, 1975).

As Southwood (1977) points out, the total energy flux perpendicular to $\underline{B}$ in a hot collisionless plasma is

$$\underline{v}_\perp (\delta p_\perp + \underline{B}.\underline{b}/\mu_o)$$

where $\underline{v}_\perp$ and $\delta p_\perp$ are the transverse plasma velocity and transverse plasma pressure perturbations associated with the wave. Clearly with the pressure fluctuation in antiphase with $\underline{B}.\underline{b}$, the perpendicular heat flux was in the opposite direction to the transverse Poynting flux. As Fig. 3/4 shows the magnetic pressure perturbation exceeded the particle pressure oscillation, one infers that the nett energy flux perpendicular to $\underline{B}$ was parallel to $\underline{S}_\perp$; namely antisunward and southward.

Another measurement useful in establishing the physics behind a wave oscillation is the wave wavelength perpendicular to $\underline{B}$. Fig. 3/2 shows no phase difference in the low frequency oscillation between the ISEE spacecraft. As the spacecraft were separated across $\underline{B}$ by ~450 km, a perpendicular wavelength $\lambda_\perp$ of several R_E is implied. Such a scalesize would be inconsistent with previous observations of compressional signals (Barfield and McPherron (1972), Hedgecock (1976), Su et al. (1977), Hughes et al. (1979) and Kremser et al. (1981)) which suggest they are fairly localized across $\underline{B}$ with $\lambda_\perp \sim 1R_E$.

Caution is needed however. If the parallel wavelength is large and compressional and transverse signals are comparable, requirements on the divergence of $\underline{b}$, namely

$$i\underline{k}_\perp .\underline{b}_\perp + ik_{||} b_{||} = 0,$$

indicate the transverse wave component should tend to align perpendicular to the direction of wave phase variation across $\underline{B}$. The linear transverse magnetic polarisation straight-forwardly gives the line of phase variation.

As Fig. 3/5 shows, this direction was within 9° ± 5° of perpendicular to $\underline{R}_{12}$, the spacecraft separation vector. The small perpendicular distance of 70 ± 40 km between $\underline{R}_{12}$ and the transverse wave-field direction would be consistent with the signal having a rapid perpendicular phase difference between the ISEE spacecraft. Taking this phase difference as <5° gives a lower limit on $\lambda_{\perp}$ of (5 ± 3) x 10^3 km; a figure comparable to that obtained in Section 3.3.5 where we use energetic particle data to remote sense the wave. When mapped to the ionosphere, this scalesize would give a horizontal wavelength of at least several hundred kilometres; a value sufficiently large to ensure that signal attenuation between the ionosphere and the ground was not significant (Hughes and Southwood (1976a,b)).

The ISEE vortex event magnetic footprint was determined using several model combinations of internal and external magnetic field. It fell within an area bounded by 75° to 77°N. latitude and 81° to 92°E. longitude (geographic) which is in the Kara Sea off Northern Siberia. The nearest magnetometer station, Dixon Island (73·5°N, 80·6°E), did not observe a signal in association with the vortex. However, 6 minute oscillations were seen at Tixie (71·6°N, 129°E), which was located at 0800 LT (3½ hours later in local time than the spacecraft). The signals on the ground and in space appeared almost simultaneous, and since Tixie has a nominal L-value of 5·6 the wave was clearly not localised in L-shell.

One might argue there is one curious feature in the above picture. The nett perpendicular Poynting flux

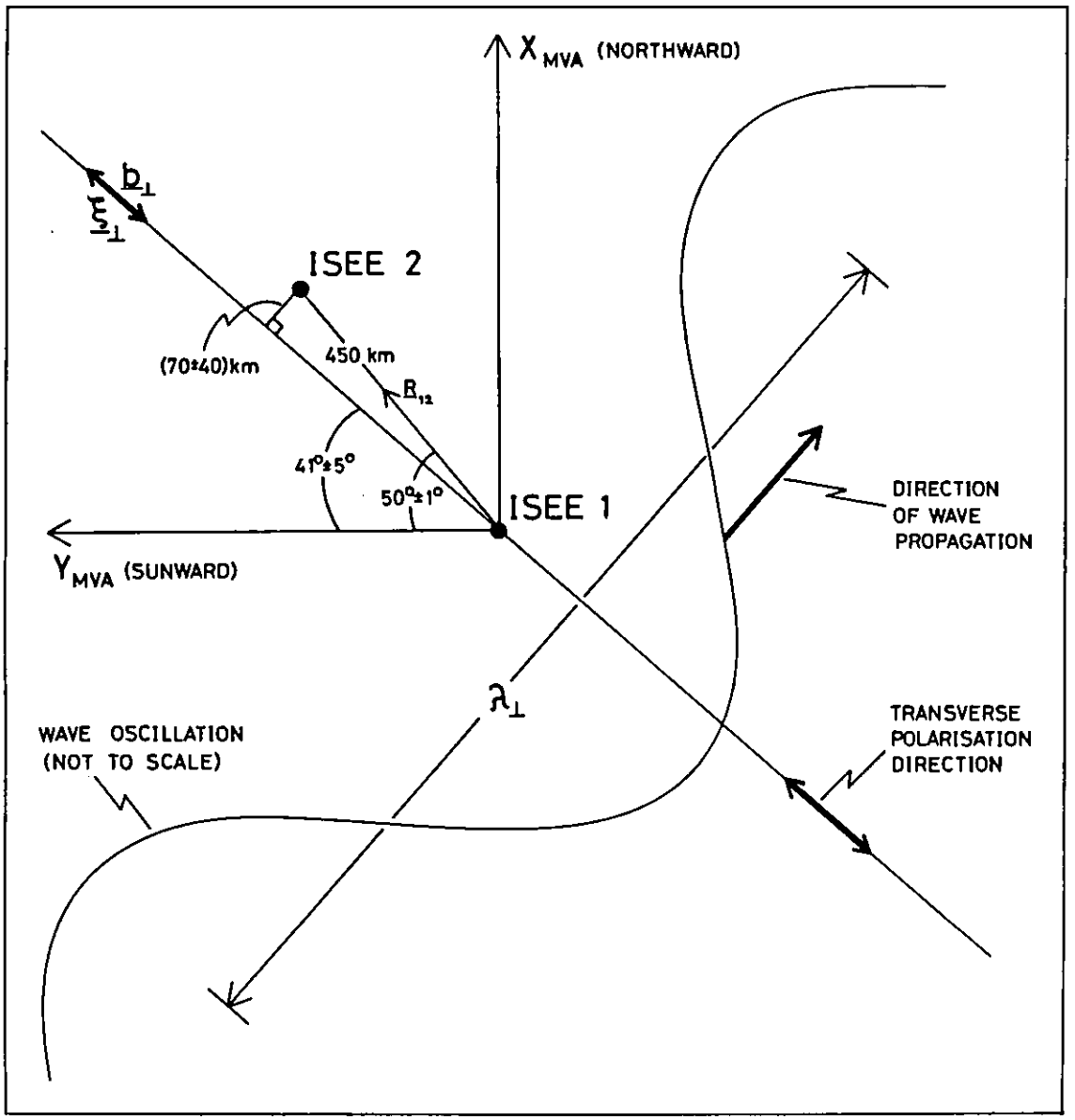

FIGURE 3/5. Transverse wave schematic of the 11th December, 1977 vortex. Although the spacecraft are separated by ∿ 450km perpendicular to $\underline{B}$, no phase difference is seen between the spacecraft (Fig. 3/2) because their separation vector, $\underline{R}_{12}$, is almost parallel to the direction of transverse wave polarisation.

(Fig. 3/4) and energy flux were at right angles to the direction of transverse wave phase variation (Fig. 3/5). Assuming particle and field pressure perturbations did not balance, one concludes that the energy flow in the 'downwave' direction (i.e. parallel to the transverse phase velocity) was not the dominant energy flux component across $\underline{B}$. Rather than being incongruous this result is perfectly reasonable. This is because transverse energy flux is associated with transverse field line motion, and here the dominant field motion was perpendicular to the 'downwave' direction. The result is also consistent with the field line resonance concept which predicts an inwards energy flux (from an outer boundary source) perpendicular to the downwave direction.

The oscillation mode of hydromagnetic wave flux-tubes is important for delimiting the pulsation energy source (e.g. Southwood, 1980). Various arguments indicate the hydromagnetic vortex was oscillating principally in the fundamental mode and was generated at the equator:

(a) From the stretched string model of a field line (Sugiura and Wilson, 1964), and the spacecraft location (12° above the GSM equator but $\sim 6R_E$ above the Fairfield model neutral sheet position (Fairfield, 1980)), $\underline{b}_\perp$ would lead $\underline{v}_\perp$ in phase for odd-mode oscillations, while in even-mode signals $\underline{b}_\perp$ would lag $\underline{v}_\perp$. Fig. 3/2 shows $\underline{b}_\perp$ leads $\underline{v}_\perp$ by $\sim 135°$, implying a fundamental mode oscillation but not a pure standing wave.

(b) The presence of a background particle energy change δW during the disturbance (Fig. 3/1) also indicates a

symmetric signal. In an antisymmetric wave the bounce-average of δW is zero (Southwood and Kivelson, 1981) and so the nett δW in an even-mode wave with a frequency much less than the particle bounce frequency is small.
(c) The nett Earthward field-aligned energy flux is most easily understood if there is an equatorial energy source, and consequently, a symmetric disturbance.
(d) The local Alfvén wavelength was $\sim 70 R_E$; a value consistent with expectations for a fundamental odd-mode disturbance.

3.3 Energetic Charged Particle Observations

3.3.1 Introduction

Energetic charged particle behaviour in a low frequency compressional hot plasma wave can be an important wave structure diagnostic. Firstly, energetic ions, through their large gyroradii, provide a means of 'sounding' transverse wave structure. A spinning detector with a look direction at right angles to $\underline{B}$, remote-senses the spacecraft vicinity to two gyroradii in a spin period. As Williams (1979) and Williams et al. (1979) have demonstrated at the magnetopause, the presence, orientation and velocity of density gradients can be inferred with this sounding capability. We use this technique here to infer the location of wave-induced density gradients.

Secondly, by comparing particle behaviour over a range in energy the potential exists for delimiting wave structure both along and perpendicular to $\underline{B}$. This is because a particle's response to a wave depends on how it 'sees' the wave; namely on how its bounce frequency ω_b

and mean drift frequency $\tilde{\omega}_d$ (due to gradient and curvature magnetic forces) relate to the wave frequency ω (Southwood and Kivelson, 1981). We compare ion flow behaviour with energy for flows parallel and perpendicular to $\underline{B}$, but are limited by the fact that $\omega_b \geq \omega$ over our spread in particle energy. This means the response of all particles we analyse depends on the average wave amplitude over their entire bounce orbit. Particles having $\omega_b < \omega$ are required to gain information on local wavefields.

3.3.2 Data

ISEE 1 MEPE ion (assumed to be proton) and electron differential flux data are shown at high resolution in Fig. 3/6 for half a vortex wave cycle. The magnetic field strength variation is included for reference in the top panel. Two ion (44·5-65·5 and 95·5-142 keV) and two electron (22·5-39 and 75-120 keV) energy channels are plotted. Other energetic charged particle energy channels showed similar features. The detector scan motion is shown by the zig-zag curve at the base of the plot, taking 36·5s for a full unit sphere scan. Scan UP (DOWN) looks towards ecliptic north (south). During its up/down motion the detector scans continuously in longitude (see Section 1.3 for a description of instrument operation).

There is a marked difference between the ion and electron records. The ion data have strong 3s (spin-cycle) modulations indicating nearly an order of magnitude greater flux in one look direction to the opposite direction. Equivalently one should note the large flux difference between times of upscan and downscan. The electron flux,

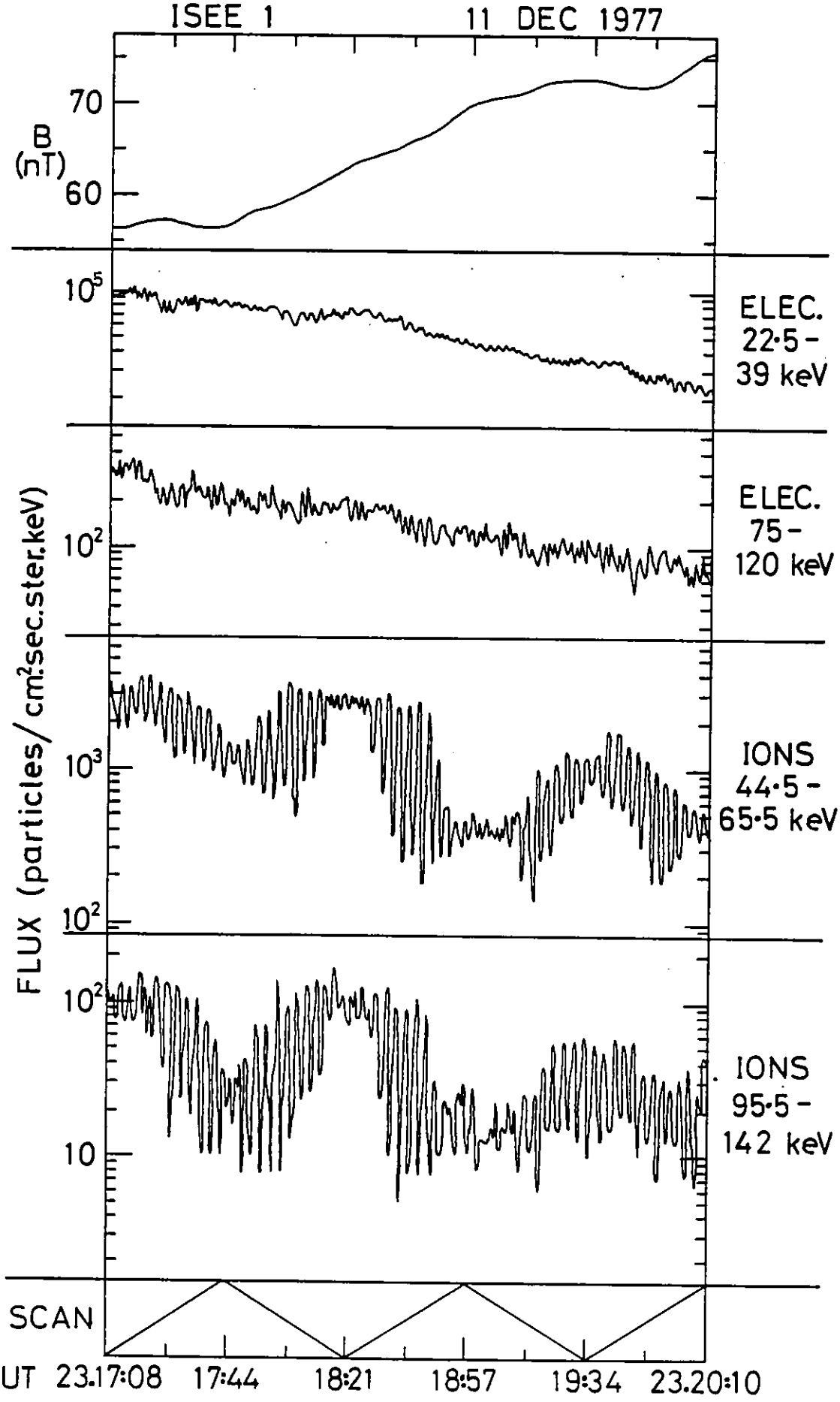

FIGURE 3/6. High resolution electron and ion MEPE flux observations during half a vortex wave cycle when B (top panel) is increasing. Detector scan motion is shown in the bottom panel.

in contrast, shows little evidence for spin asymmetry. As will become clear, this disparate behaviour is a consequence of the different species gyroradii. For the moment it is necessary only to note that the gyroradii r_L of 119 keV protons and 31 keV electrons in the prevailing 65γ field were 770 km and 6 km respectively. Since 90° pitch angle particles reflect flux conditions a gyroradius away, over a spin cycle and in the absence of bulk flow, the 119 keV protons can 'sound' conditions at points separated in space by up to 1540 km compared with 12 km for the 31 keV electrons.

Fig. 3/7 illustrates the flux asymmetries in terms of pitch angle. Data from the P3 ion (44·5-54·8 keV) and E3 electron (39-60 keV) energy channels are displayed in time sequence from 23.13:11 U.T. to 23.22:18 U.T. through the main vortex event. The three-dimensional particle distributions are presented in the latitude, θ, longitude, ϕ, format described by Williams (1979) except that here the ion intensities are colour-coded. The display is in satellite coordinates, or equivalently, solar ecliptic coordinates, where ϕ=0°, θ=90° corresponds to X_{GSE}; ϕ=90°, θ=90° corresponds to Y_{GSE}; and θ=180° corresponds to Z_{GSE}. Note the particles observed are moving away from the directions labelled. Intensities are indicated by the logarithmic colour bar beside each figure. Multiplication by 69·3 converts all intensities to differential fluxes. The data tilt readily identifies UP scans (θ=10° to 170°) from DOWN scans (θ=170° to 10°).

The time at the head of each panel is the centre

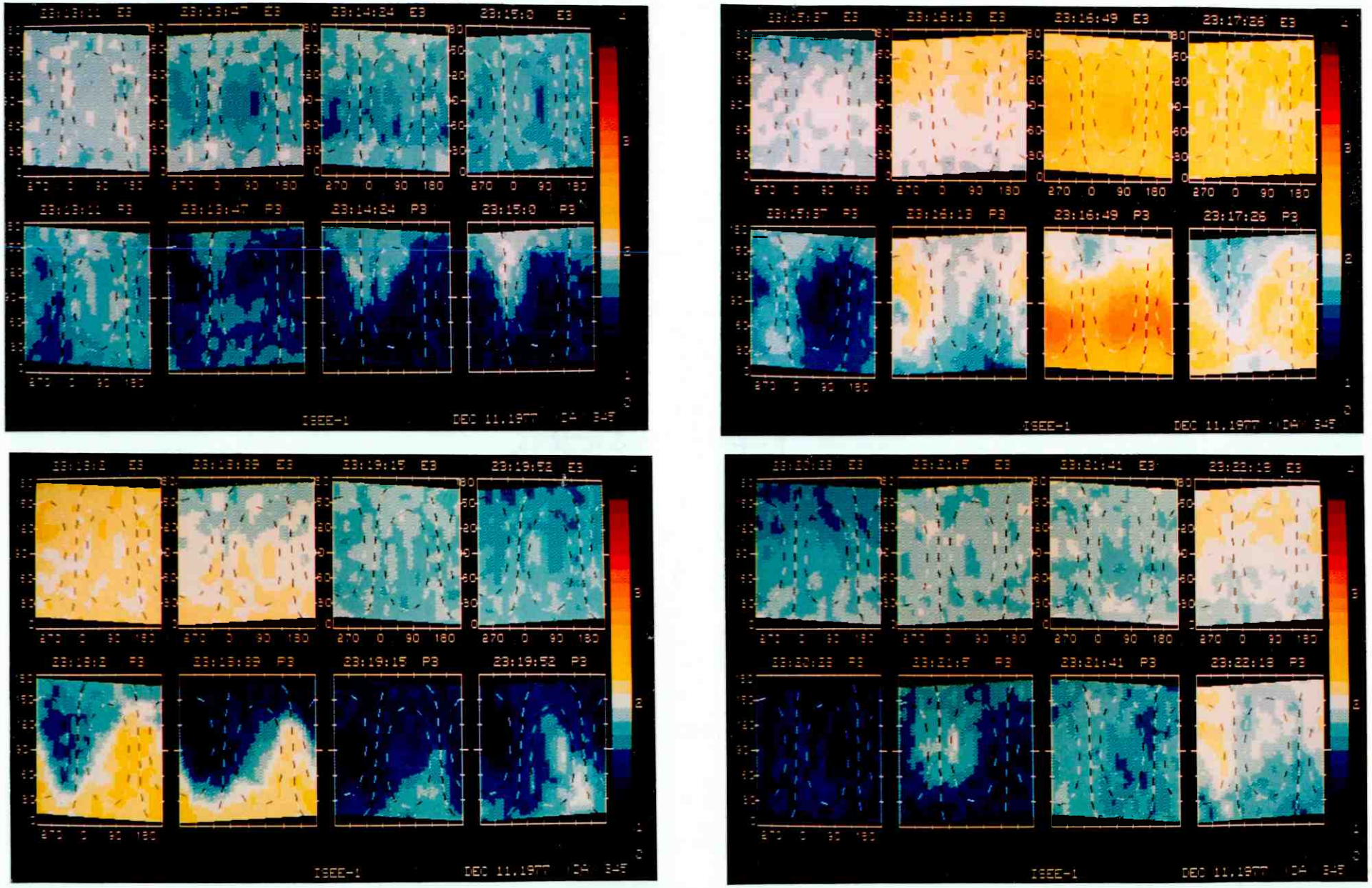

FIGURE 3/7. Colour coded flux intensities in terms of pitch angle from the P3 ion (44·5-54·8 keV) and E3 electron (39-60 keV) MEPE energy channels.

time for that particular three-dimensional scan. Black and white dashed lines give the locus of 90° (unclosed vertical curves) and ± 60° (ellipses) local pitch angles determined from the magnetic field at the scan centre time. With $\underline{B}$ principally in the $+Y_{GSE}$ direction, the central panel ellipse is the -60° pitch angle locus. The data are continuous, apart from transmitter interference by the electron density experiment in the lower ¾ of the 23.16:49 U.T. panel.

Ion flux asymmetries are clear. For example, those evident in Fig. 3/6 are now striking in the 23.18:02 and 23.18:39 U.T. panels. It is interesting to note the reversed asymmetry sense at these times compared with the panels at 23.14:24, 23.15:00 and 23.21:05. This change has the six minute vortex period.

There is no evidence for E3 electron flux spin cycle asymmetry. However, a longer period flux change was apparent showing that at field strength minimum the flux was greatest (23.17:26 panel) and at field maximum it was lowest (23.15:0 and 23.20:28 panels). The P3 ions also showed a 6 minute period flux change in phase with the electrons. Indeed, this flux oscillation was present, and nearly in phase for both species, to energies of at least 200 keV.

Ion distribution functions at field strength maximum and minimum are shown in Fig. 3/8. The distributions at thermal energies are Maxwellians computed from the LANL/MPI observed number densities and temperatures

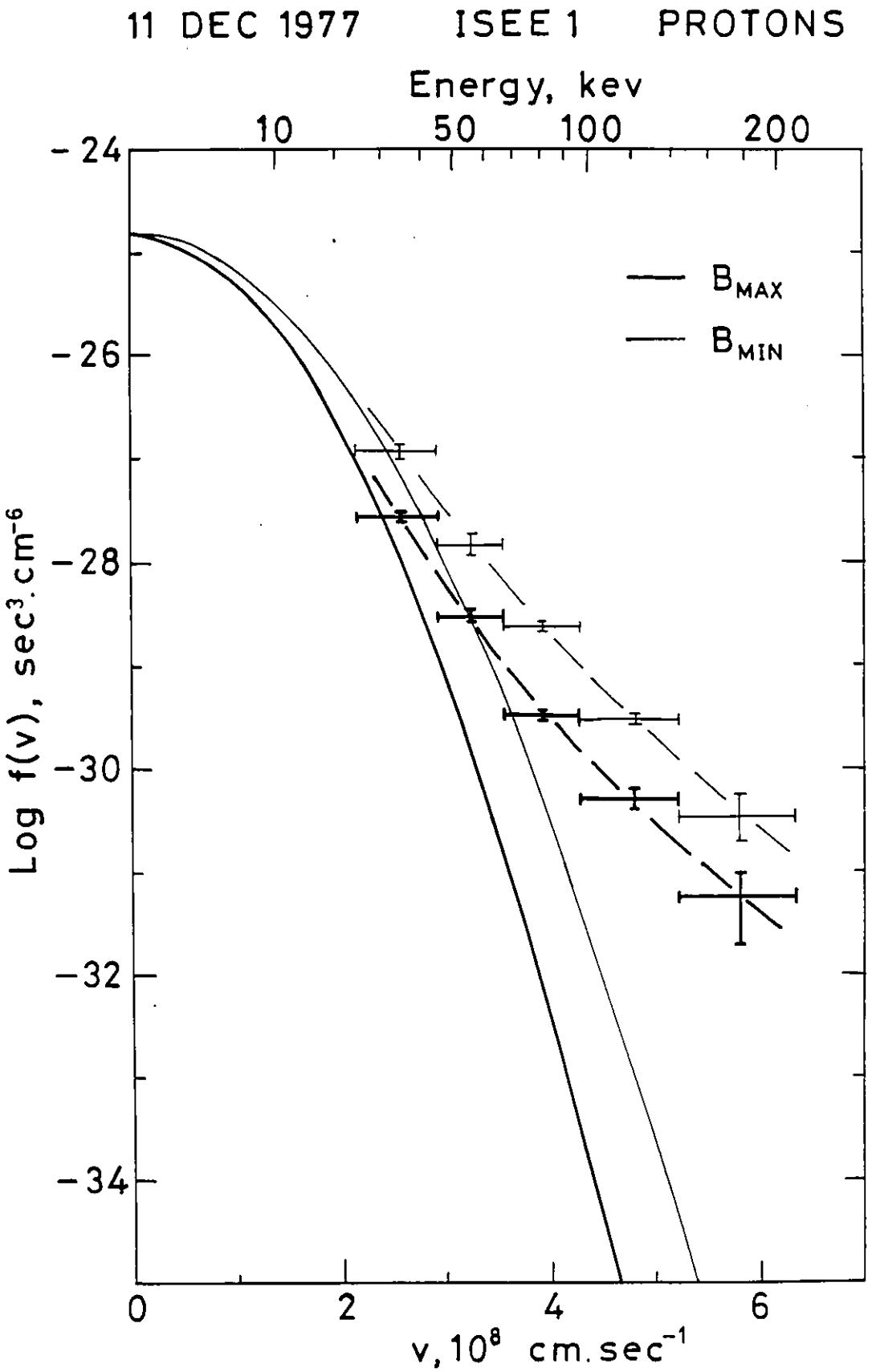

FIGURE 3/8. Proton distribution functions recorded at field strength maximum and minimum. The continuous curves are Maxwellians computed from the thermal number densities and temperatures, while the high energy data are MEPE measurements.

(W=6·4 keV, n=1·18 cm^{-3} (B_{MIN}); W=4·8 keV, n=0·72 cm^{-3} (B_{MAX})) . The high energy distributions are MEPE data; they are power laws with a spectral index α of 4·2. Note the smooth spectral transition from thermal to power law around 30 keV, an energy near the expected $(\alpha+1)kT$ transition point (Roelof et al., 1976; Sarris et al., 1981). This high energy tail has some dynamic importance, since energies above 45 keV contributed about 10% of the total plasma pressure. The peak-to-peak ion energy change evident in Fig. 3/8 was about 40% independent of initial energy. This independence shows that parallel electric fields were not an important acceleration source, as a parallel potential drop would provide an energy change independent of energy.

3.3.3 $\underline{E}$ x $\underline{B}$ drift

To investigate the cause of the MEPE spin cycle flux asymmetries, we first study the effect of $\underline{E}$ x $\underline{B}$ drift. Fig. 3/9 shows vortex event electric field data from the spherical double-probe experiment on ISEE 1 (see Fahleson et al. (1979) for a description of the experiment and its limitations). The magnetic field (also in GSE coordinates) is included in this Figure for reference. Unfortunately the $\underline{E}$ field experiment was in its 'grounded' or less favourable mode for the event. In addition, as only the electric field in the satellite spin plane is measured directly (E_x and E_y in GSE coordinates), E_z has to be determined assuming $\underline{E}.\underline{B} = 0$. When $\underline{B}$ lies within about 10° of the ecliptic as occurred here, this

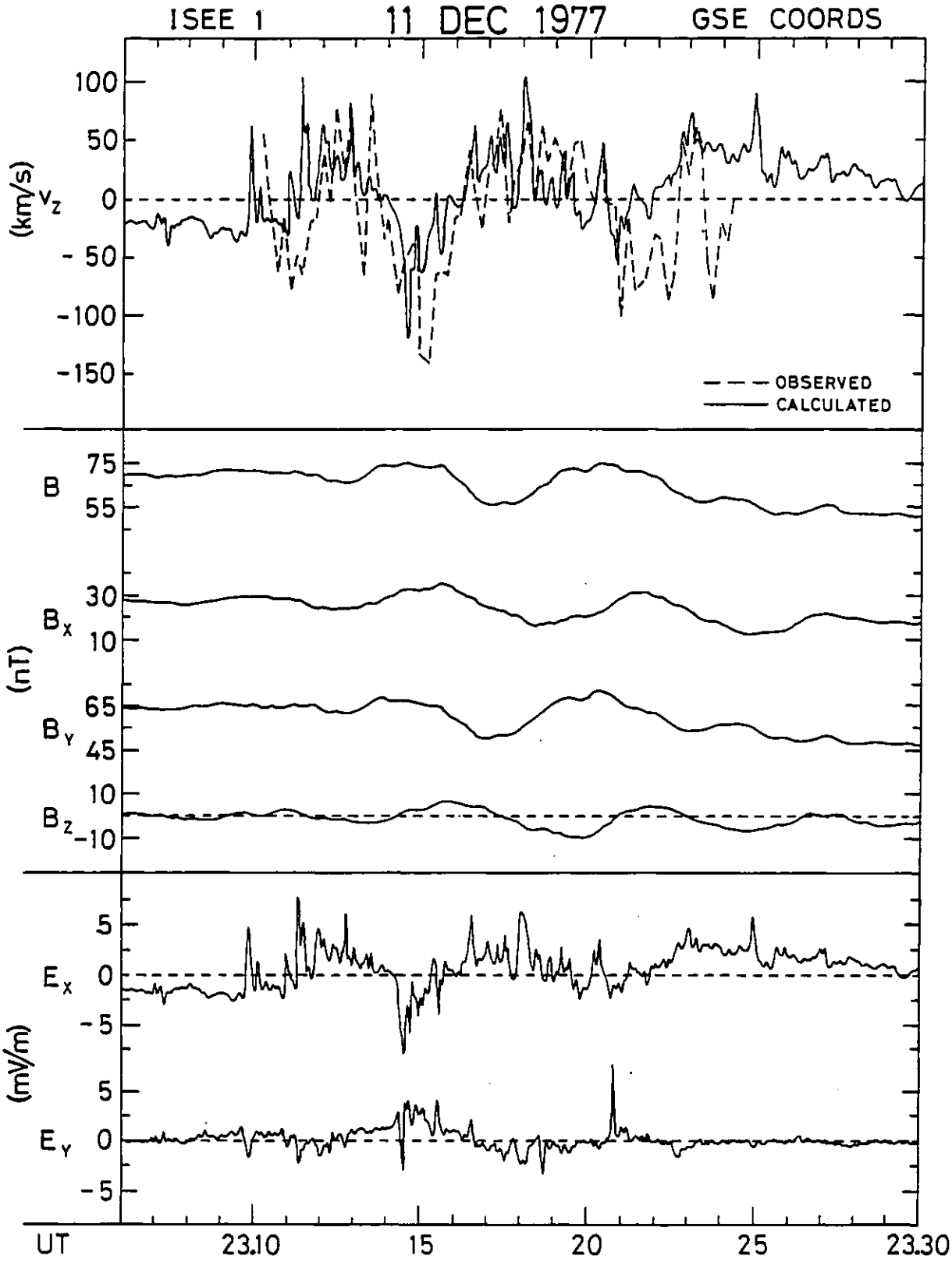

FIGURE 3/9. Plasma flow, electric field, and (for reference) magnetic field data displayed in GSE coordinates. The top panel compares the observed, (fast plasma experiment), and computed, ($\underline{E}x\underline{B}/B^2$), northward flow speeds.

assumption produces inaccuracy in E_z. In such circumstances only the $u_{z\,GSE}$ velocity component can be reliably calculated from $\underline{u}_E = \underline{E} \times \underline{B}/B^2$; this is shown in Fig. 3/9 with the LANL/MPI observed $v_{z\,GSE}$. When comparing these, one should remember that $v_{z\,GSE}$ is the most poorly determined LANL/MPI flow component (Section 1.3). Also, as the observed plasma flow

$$\underline{v} = \underline{u}_E + \underline{v}_d + \underline{v}_D$$

where $\underline{v}_d$ is the magnetic gradient and curvature drift and $\underline{v}_D$ represents fluid drift due to local pressure gradients, $\underline{u}_E$ may be only an approximate indicator of plasma drift perpendicular to $\underline{B}$. However, this approximation should be good at low energy because $\underline{v}_d$ and $\underline{v}_D$ are both energy dependent. Despite some scatter, sufficient agreement exists between u_z and v_z to conclude the low frequency thermal flows at right angles to $\underline{B}$ were principally due to $\underline{E} \times \underline{B}$ drift.

Was $\underline{E} \times \underline{B}$ drift also important at high energy, perhaps producing or contributing to the spin-period flux asymmetries? We investigate this possibility by comparing in Fig. 3/10 ion flow behaviour at various energies in the Z_{GSE} (perpendicular to $\underline{B}$) direction. The top row is the thermal energy channel which has a shorter sampling interval than the more energetic channels below. The flow sense for these latter channels is given by the count rate anisotropy defined as (A-B)/(A+B). Notice (a) that oscillations at all energies were in phase, and (b) the flux anisotropy increased with particle energy. While the first

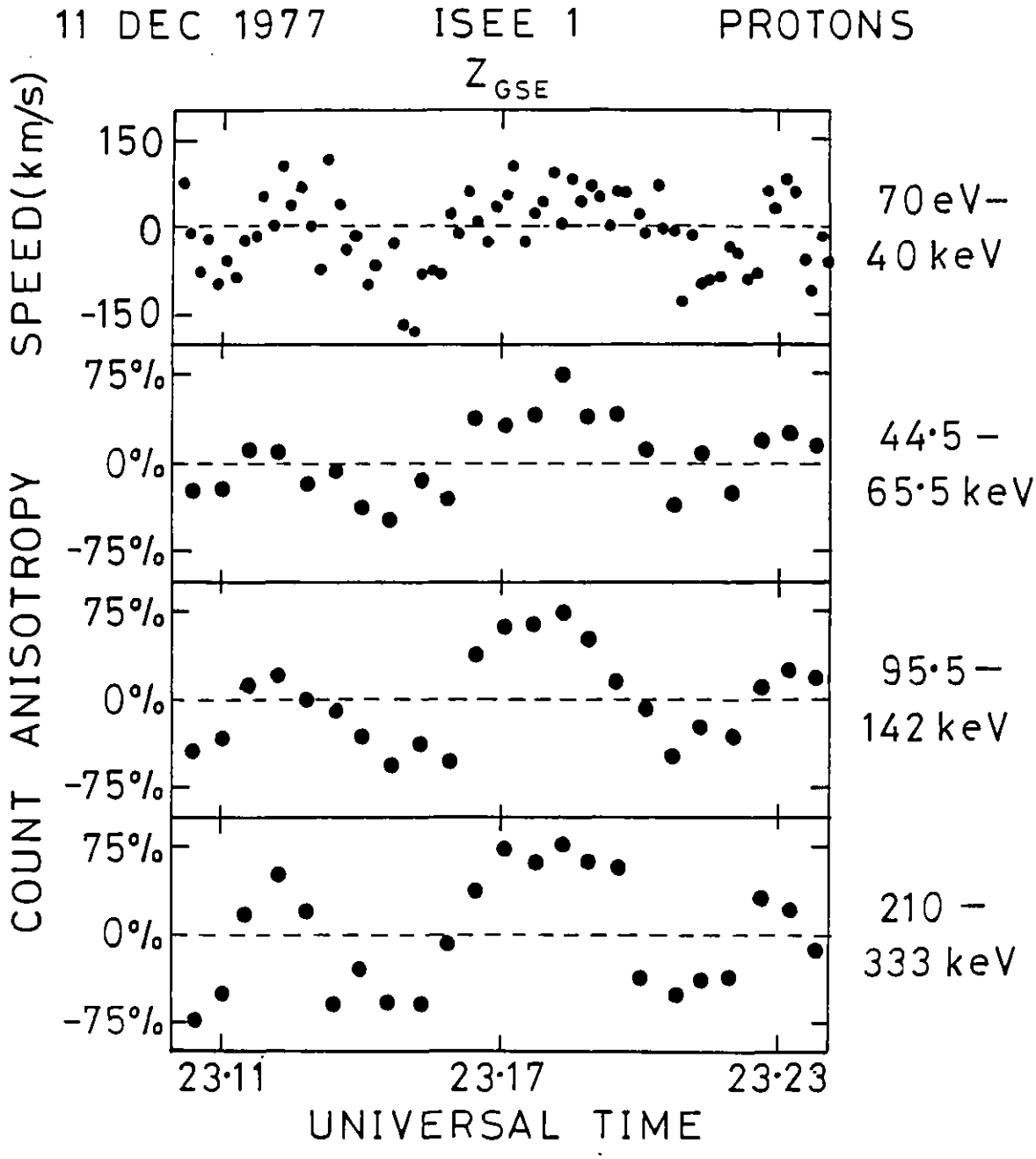

FIGURE 3/10. Ion (assumed to be proton) flow behaviour at four energies in the Z_{GSE} (perpendicular to B) direction, with the top panel displaying LANL/MPI data and the lower panels showing MEPE recordings.

point is consistent with $\underline{E} \times \underline{B}$ drift, the second is certainly not.

Southwood and Kivelson (1981) have shown how a particle gyrating through a wave electric field is continually accelerated and decelerated on the scale of its Larmor orbit. They term this acceleration by the wave 'gyration acceleration'. Depending on detector look direction a particle's velocity can change by $\pm \underline{E} \times \underline{B}/B^2$. The effect of this acceleration is equivalent to the Compton-Getting effect (first noted in cosmic ray studies: Compton and Getting (1935); also, see Ipavich (1974) and Roelof et al. (1976)). If a particle distribution moves at bulk speed δv (the $\underline{E} \times \underline{B}/B^2$ drift speed) relative to a spacecraft detector, the detector sees a different angular distribution to the plasma rest frame distribution. For a power law spectrum of spectral index α, the change in distribution δf (or Compton-Getting anisotropy) at particle speed v and distribution function f is

$$\delta f/f = 2(\alpha+1)\frac{\delta v}{v} \ .$$

Fig. 3/11 indicates the size of the effect. Energetic ion distribution functions are shown for a successive downscan (23.18:21) and upscan (23.18:57) when the fast plasma experiment saw plasma streaming northward at ~100 km/s. The dashed line gives the Compton-Getting correction (δv = 200 km/s) to the upscan distribution. Although clearly still significant at W~30 keV (contributing about a third of the distribution function change), gyroacceleration was not the dominant cause of energetic ion flux spin-cycle asymmetry. The

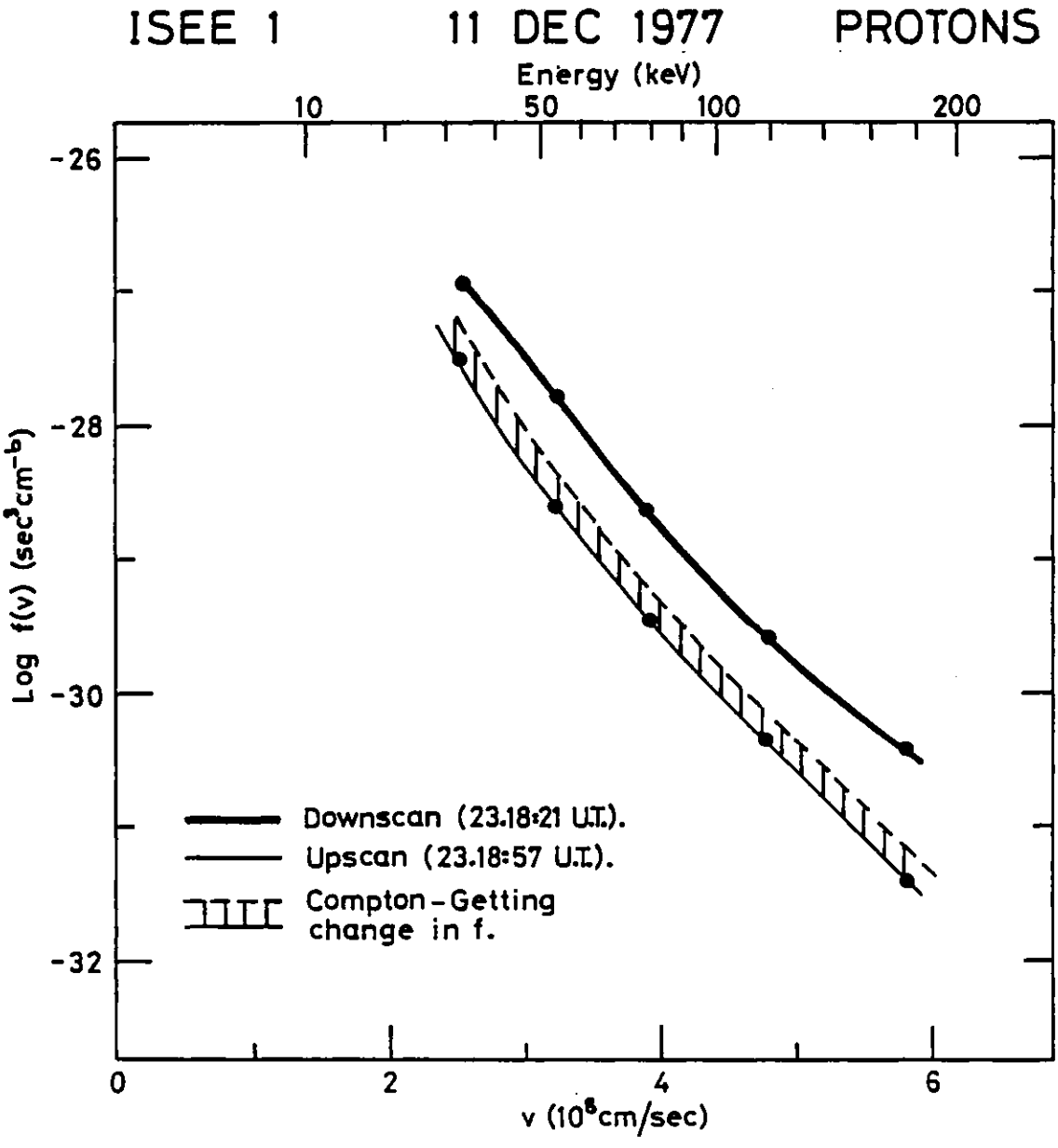

FIGURE 3/11. Illustration of the size of the Compton-Getting effect in relation to the observed energetic ion flux asymmetry. MEPE proton distributions are shown for a successive downscan and upscan when the bulk flow was northward at ∿ 100km/s. The difference in f between the upscan distribution and the dashed line represents the Compton-Getting contribution to the change in f between upscan and downscan.

most simple explanation for this energetic ion behaviour, and an interpretation which we shall develop in the following two sections, is that it is based on the mechanism first described by Su et al. (1977) and more recently by Kremser et al. (1981). It seems the flux asymmetries are due to diamagnetic drift from wave-induced pressure gradients.

3.3.4 Oscillating ambient density gradient : a single instrument view.

Here we describe an interpretation of the hydromagnetic vortex suggested by Dr. Ted Fritz based on ISEE 1 MEPE data alone (Edinburgh IAGA talk, 1981; ICST vortex workshop, August 1981). Oscillatory motion of an ambient density gradient forms the basis of the interpretation. Although the multi-instrument data set indicates this could not be the case (Section 3.3.5), a view now accepted by Fritz (Berkeley vortex workshop, December 1981), it is instructive to outline Fritz's data analysis method and results for subsequent reference.

Estimation of density gradient location, orientation and velocity is common practice with the ISEE energetic particle data. The technique, described by Williams (1979), has been applied at the magnetopause (Williams et al., 1979) and plasma sheet / tail lobe interface (Spjeldvik and Fritz, 1981). Let us now assume there is an ambient density gradient near ISEE and apply the same technique. First let us consider the P3 panel at 23.14:24 and note the V-shaped response centered on the 90° pitch angle locus between the $-Y_{GSE}$ (ϕ = 270°) and

$+X_{GSE}$ (ϕ = 0°) directions. All 90° pitch angle particles from a latitude $\theta \sim 75°$ through to $\theta \sim 170°$ on the opposite side of the Z_{GSE} axis were sensed at high intensity during the 36·5s scan. Other 90° pitch angles were present but at a reduced intensity. The particle trajectories appropriate to this geometry are displayed in Fig. 3/12(a) using an MVA coordinate system where $Z_{MVA} = \underline{B}$ and $X_{MVA} = Z_{GSE}$, which is almost identical to the MVA system described previously. The inferred density gradient location is shown by the heavy line lying ∿ 210 km <u>above</u> ISEE 1 at an angle ∿ 43° to the Y_{MVA} axis.

Now consider the 23.18:02 P3 panel. 90° pitch angle fluxes were greatest between $\theta \sim 150°$ and $\theta \sim 40°$ on the opposite side of Z_{GSE}. The corresponding particle trajectories and inferred density gradient position are shown in Fig. 3/12(b). The density gradient has reversed sense, it is now apparently ∿ 500 km <u>below</u> the spacecraft and inclined by ∿ 35° to the Y_{MVA} axis. Repeating this analysis procedure at other times allows the density gradient motion to be tracked. The distance D of some reference level density from ISEE 1 is plotted against time in the upper panel of Fig. 3/13 using P2 (34·2 - 44·5 keV) and P3 (44·5 - 54·8 keV) energy channel data. The data points are the heavy dots, and positive (negative) D means that the density gradient was northward (southward) of the spacecraft, in the sense that the spacecraft was always in the high density region. The dotted arrows at ± 820 km indicate that the gradient was more than two P2 (40 keV) ion gyroradii from the spacecraft; in other words no flux asymmetries were seen before 23.13:11, at 23.16:13,

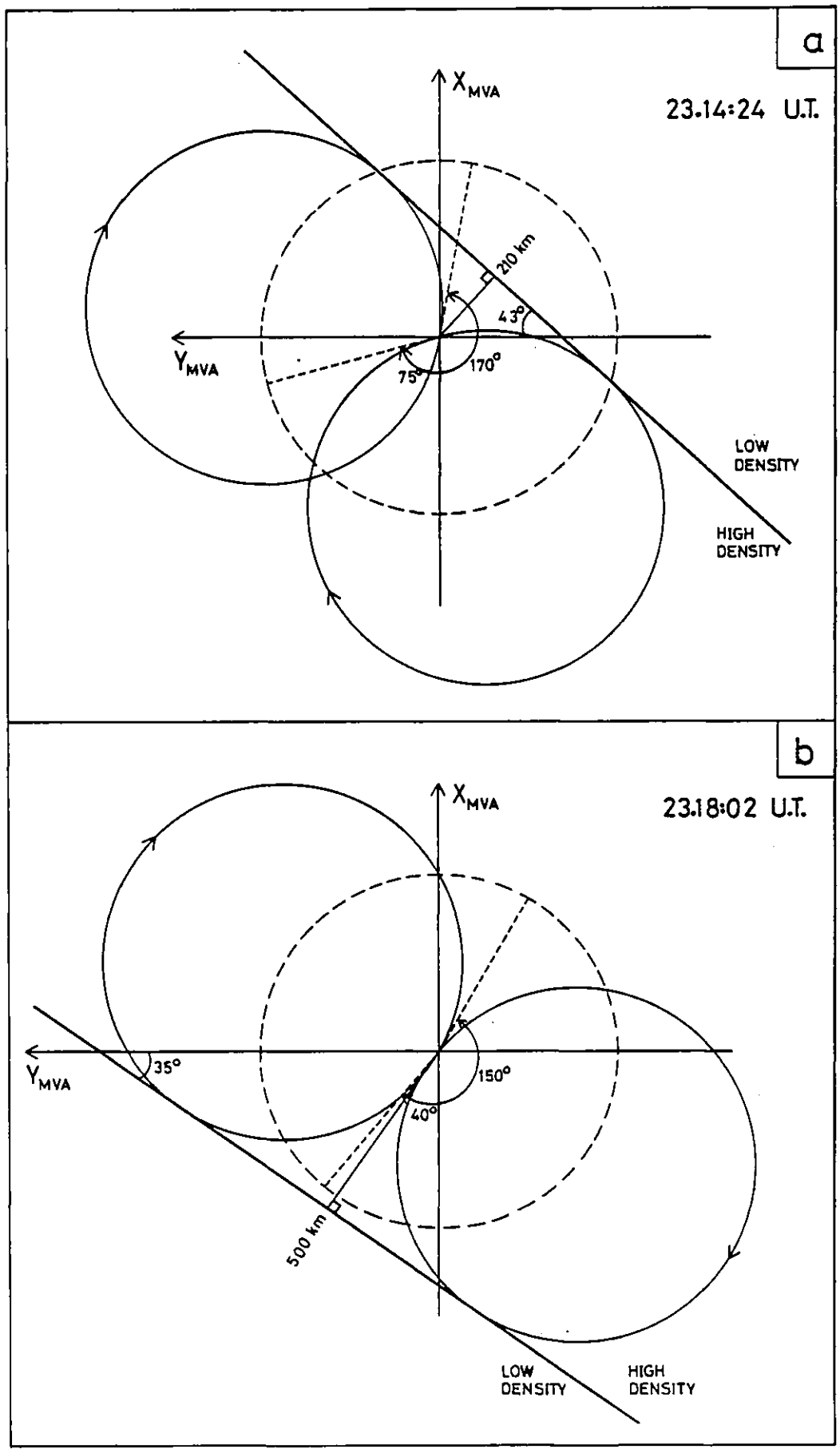

FIGURE 3/12. Geometry used in estimating the density gradient location and orientation from the MEPE data in Fig. 3/7. Detector position is at X_{MVA}, $Y_{MVA}=0$, and the dashed circle represents the locus of all P3 (50keV) proton gyrocentres which impact the detector. (The gyroradius of a P3 proton is ∿ 460km). The solid circles define the proton orbits which appear to graze the boundary separating regions of high and low density. The inferred density gradient position is shown by the thicker line.

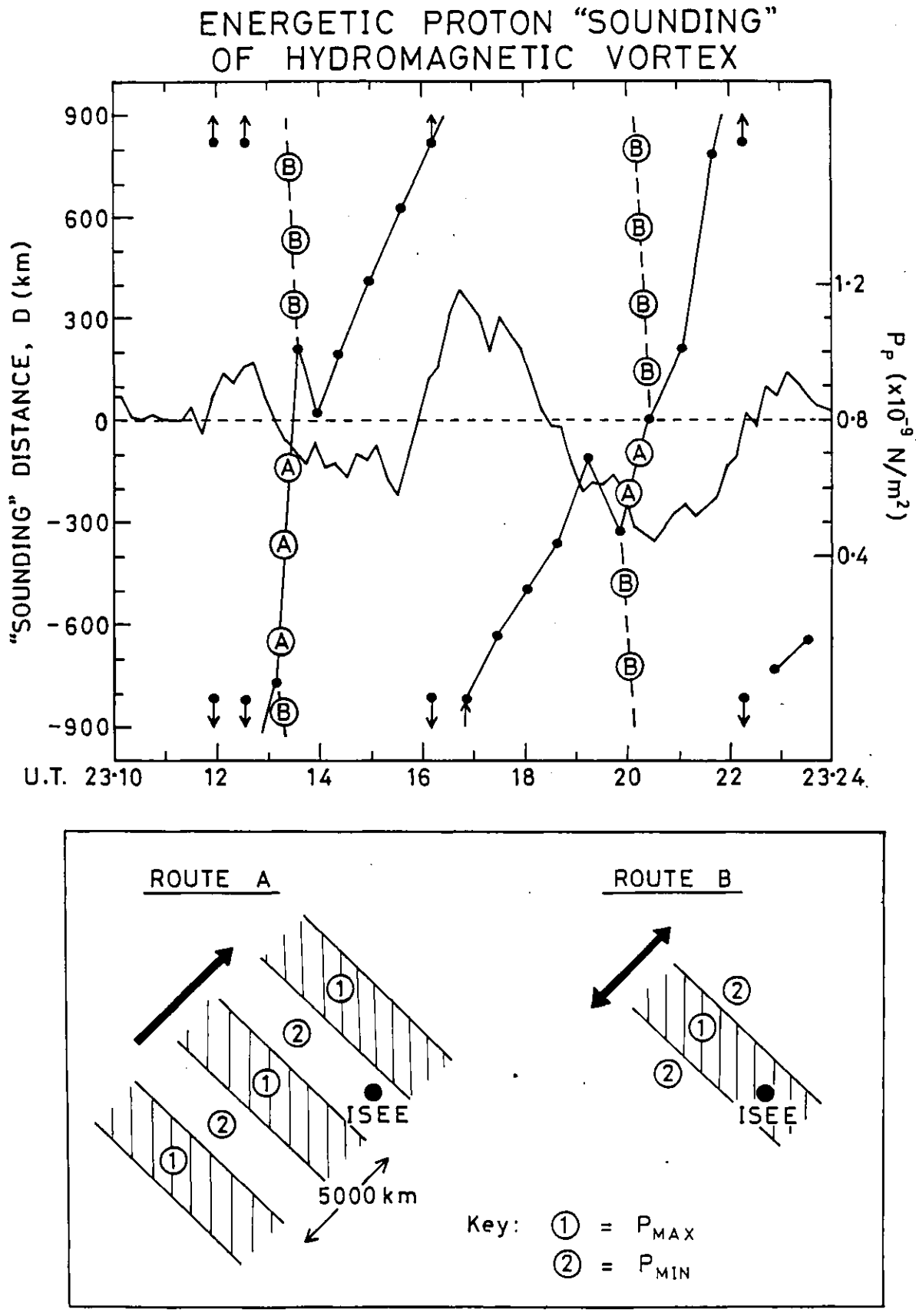

FIGURE 3/13. The top panel shows the density gradient 'sounding' distance (D) as a function of time, with, superimposed, the variation in thermal proton pressure (P_p). The lines containing circled A's and B's denote alternative routes for joining the data points either side of D=0, with the letters referring to the physical models (Route A and Route B) shown schematically in the lower panel and discussed in the text.

23.20:29 and at 23.22:18. The lack of asymmetry in the 23.20:29 panel is discussed further below and again in Section 3.3.5.

The two sets of lines containing circled A's and B's represent alternative ways of connecting the solid lines. The letters directly relate to the model predictions (routes A and B) shown in the lower part of the Figure. In these schematics regions (1) and (2) denote areas of high and low particle pressure respectively. The solid arrow indicates their motion with respect to ISEE. A natural interpretation of the large ion flux gradients is in terms of an ambient density gradient which oscillates back and forth across the spacecraft, as route B depicts. Alternatively the density gradients, or equivalently, the non-uniformity in particle guiding centres, could have been induced by a wave which propagated past the spacecraft; this situation corresponds to route A and is discussed in Section 3.3.5. Finally, note the LANL/MPI proton pressure variation which is included in the centre of the upper Figure for later reference.

Considering the crude analysis method and probable change in gradient location during a 36s scan, the D values should be taken as a guide only. Nevertheless a pattern is clear: the gradient was periodically below and then above the spacecraft, the spacecraft remaining always on the high density side (apart from 23.20:29 U.T. when ISEE was > $2r_L$ from a high density region). Fronts of constant pressure (orientations not shown) favoured a particular direction; namely that observed in Fig. 3/12, which is very similar to the phase front direction deduced earlier (Section 3.2.4)

from the magnetometer data. Fritz (Edinburgh IAGA talk, 1981; ICST vortex workshop, August 1981) interpreted this density gradient as a 'sounding' of the plasma sheet boundary, a situation which can be pictured as an extreme example of route B (Fig. 3/13). He argued that the gradient was sometimes below and sometimes above the spacecraft because ISEE was inside an oscillating plasma sheet 'horn' - a descriptive term for the structure connecting the plasma sheet and auroral zone. The upper boundary was pictured as the plasma sheet / tail lobe interface with the lower boundary as the inner edge of the plasma sheet. This interpretation requires a 'horn' thickness of about 2000 km ($\sim 4r_L$) and oscillation speed $\sim$ 10 km/s. In this picture the low flux seen throughout the 23.20:29 panel would have been a consequence of ISEE 1 exiting at least $2r_L$ into the lobe. We show in the next section why both this interpretation and the more general one of an oscillating ambient density gradient are incorrect.

3.3.5 Wave-induced pressure gradients : a twin-instrument view.

The vortex interpretation suggested by Fritz was based on data from one instrument : the ISEE 1 MEPE experiment. Since the 450 km spacecraft separation perpendicular to $\underline{B}$ was at right angles to the density gradient, comparison of ISEE-1 and 2 MEPE responses would not be a definitive test for this oscillatory ambient density gradient theory. However, a twin-instrument view of the event (combining MEPE with LANL/MPI fast plasma data) does show this interpretation to be incorrect.

We conclude the density gradients were wave-induced.

Let us reconsider Fig. 3/13. Route B, the oscillating ambient density gradient interpretation, requires the trend in gradient location, clearly diagonally upward with the six minute wave period, to suddenly (within 36s) reverse sense at ∿ 23.13:30 and again at ∿ 23.20:10. Consequently, at these times the low density region has to switch from below to above the spacecraft. Such reversals in the route B picture would require rapid southward motion, when in fact, the thermal plasma flow was clearly northward. This is shown in Fig. 3/14 : the energetic ion sounding distance plot is displayed again at the top, with the thermal plasma flow in field-aligned coordinates plotted below. v_x and v_y, the transverse flow components, are rotated from their directions in the Fig. 3/2 MVA display such that v_x is now perpendicular to $\underline{b}_\perp$ and directed northwards approximately <u>along</u> the pressure gradient. Clearly during the two crucial intervals, which for emphasis are boxed by the vertical guidelines and in which the flows have been shaded, the major transverse flow was in the positive x - direction. That is, $\underline{v}_\perp$ was directed along the pressure gradient and northward, which is opposite to the direction required by route B. Notice also that v_z, the field-aligned flow component is negative throughout these intervals; this also does not fit with the route B picture, since when ISEE was clearly in the middle of the high density region (at ∿ 23.16:20 and at ∿ 23.22:20), v_z was strongly positive.

Fig. 3/13 provides further evidence that the oscillating ambient density gradient model is incorrect. Consider

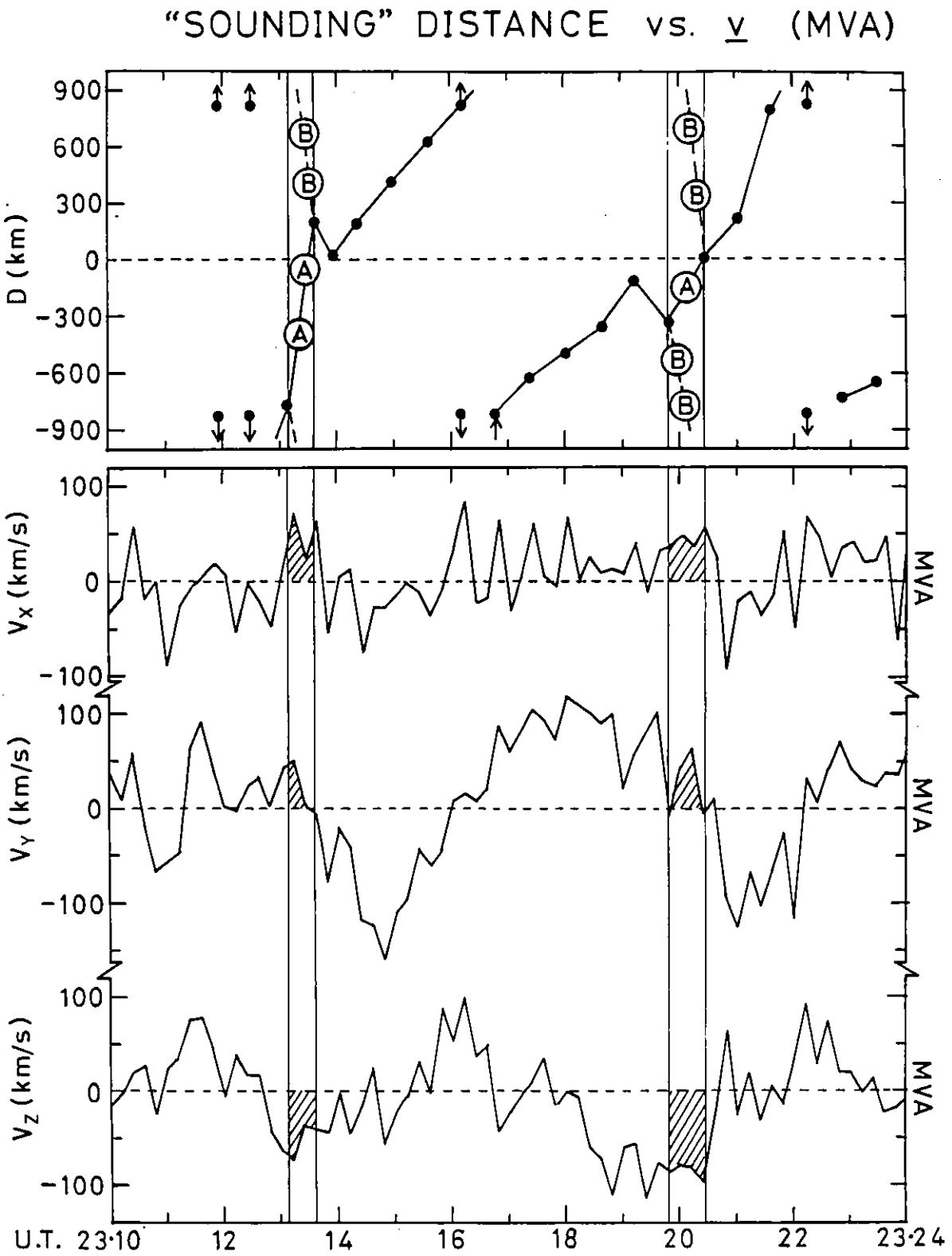

FIGURE 3/14. A display of the energetic proton 'sounding' distance plot of Fig. 3/13, and of the thermal flow in a rotated MVA coordinate system where X_{MVA} is approximately parallel to the pressure (density) gradient.

the proton pressure p during the same two crucial intervals in question above. p was near a minimum throughout, and did not suddenly revert through a maximum as route B requires. An additional argument against Fritz's specific interpretation of route B in terms of the plasma sheet / tail lobe interface is that there was no evidence for a plasma sheet crossing (as required, for example, at 23.20:29) in the LANL/MPI plasma data from either spacecraft, either before, during or after the event. Density and thermal energy exceeded $0{\cdot}4 cm^{-3}$ and 3 keV throughout. The data also show ISEE had been outbound inside the plasma sheet since at least 22.00 U.T..

Route A, the propagating wave-induced density gradient can straightforwardly explain all the features in Figs. 3/13 and 3/14. One can visualise route A as successive wave phase fronts approaching, passing over, and receding northwards from the spacecraft. Notice how the gradient in p correctly changes sense almost exactly when the 'sounded' gradient switches from below to above the spacecraft and vice versa. Assuming that the wave has a sinusoidal plane waveform, we can estimate the transverse wave wavelength $\lambda_\perp$ using

$$\lambda_\perp = \pi n_o / |\underline{\nabla} n|_{max} \quad ,$$

where n_o and $|\underline{\nabla} n|_{max}$ are the 90° pitch angle peak-to-peak density oscillation, and maximum density gradient, over a half-wave cycle. Obtaining n_o and $|\underline{\nabla} n|_{max}$ at several energies from pitch angle plots like those in Fig. 3/7, and for intervals of increasing and decreasing $|\underline{B}|$, gave the $\lambda_\perp$ values in Table 3/3 . Although the contribution of $\underline{E} \times \underline{B}$ drift to n_o and $|\underline{\nabla} n|_{max}$ was not eliminated in these

calculations, its effect on our value for $\lambda_\perp$ should be small. The mean wavelength was $\lambda_\perp = (5\pm1)\times10^3$ km which corresponds to a transverse wave phase velocity of (14±3) km/s. Errors are for the 1σ (68%) level. Correction for ISEE's outward orbital velocity of $\sim$ 2km/s , which was principally in the meridian, would not significantly modify this phase speed value.

Implicit in our above interpretation, and also in the discussion of the previous section, was the assumption that diamagnetic drift was the basic cause of MEPE ion flux asymmetry. Let us now consider diamagnetic drift more quantitatively. In the hydromagnetic limit for a hot plasma and in the absence of flow, the current perpendicular to $\underline{B}$, $\underline{j}_\perp$, is proportional to plasma pressure (see e.g. Clemmow and Dougherty, 1969). Writing parallel and perpendicular wave pressure perturbations as $\delta p_{||}$ and $\delta p_\perp$ gives (Southwood,1980)

$$\underline{j}_\perp = \frac{\underline{B}}{B^2} \times \left(\underline{\nabla}(\delta p_\perp) + (\delta p_{||} - \delta p_\perp) \frac{\hat{\underline{n}}}{R} \right) \quad , \qquad (2)$$

where $\underline{n}$ is the field principal normal and R the field line radius of curvature. This equation can also be derived by combining plasma current contributions from gradient and curvature magnetic drifts with the magnetisation current (e.g. Thompson (1962, p.163), Cowley (1978)), and so is true for a subset of the plasma population. It should also be noted that in an isotropic plasma ($p_{||} = p_\perp$) the effects of $\underline{\nabla}B$ and curvature magnetic drifts are exactly cancelled by other effects in the summation. Now, observations indicate the pressure anisotropy was small, and since R was locally large (the field lines were

tail-like and DZ (distance above the Fairfield (1980) model neutral sheet) was $\sim 6R_E$), we deduce that $\underline{j}_\perp$ is proportional to the gradient in perpendicular wave pressure. The current, $\underline{j}_\perp$, is known as a diamagnetic current. Consequently, the energetic ion flux asymmetries can, if produced by a perpendicular wave pressure gradient, be the signature of a diamagnetic current. We suggest that this was the case here.

As a test, let us see if the direction of transverse wave phase motion fits with the direction and phase of the diamagnetic drift. Ampere's Law and the observed phase difference between $b_\parallel$ and $\underline{v}_\perp$ shows that it does. For a (diamagnetic) current $\underline{j}_\perp$ along the transverse wave polarisation direction, Ampere's Law gives

$$-i\mu_o \underline{j}_\perp = \underline{k} \times \underline{b} = \underline{k}_\perp \times b_\parallel \qquad (3)$$

where $\underline{k}_\perp$ is the perpendicular wave vector. In other words, to have a current with such a polarisation, $\underline{b}$ must equal $b_\parallel$, and consequently, $\underline{k}$ must equal $\underline{k}_\perp$ where $\underline{k}_\perp$ is perpendicular to $\underline{j}_\perp$. Note furthermore that since equation (2) shows $\underline{\nabla} p_\perp = \underline{j}_\perp \times \underline{B}$, and equation (3) shows $\underline{j}_\perp$ is in quadrature with $b_\parallel$, then $b_\parallel$ must be in quadrature with $\underline{\nabla} p_\perp$ just as Fig. 3/13 shows. Now the $\underline{j}_\perp$ direction depends on the sign of $b_\parallel$ such that for $\underline{k}_\perp$ tailward and northward, $b_\parallel$ increases (decreases) when $\underline{j}_\perp$ is sunward and northward (tailward and southward). This agrees with the observed phase relationship between $b_\parallel$ and $\underline{j}_\perp$ (compare Figs. 3/10 and 3/2). It may be recalled that this $\underline{k}_\perp$ direction matches the propagation direction we deduced earlier from the MEPE data, and, subject to a 180° ambiguity, it agrees with our earlier conclusion based on $\underline{\nabla} . \underline{b} = 0$.

Furthermore it is consistent with our results for a similar event (Chapter 4) when a phase shift did exist between spacecraft.

To prove numerically that the anisotropy resulting from diamagnetic drift $\underline{v}_D$ was sufficient to produce the large distribution function changes seen at high energy, we derive a simple expression for $|\underline{v}_D|$. Recognising that for a monoenergetic detector the nett drift seen is due just to a density gradient, then

$$\underline{v}_D = \frac{\underline{B} \times \underline{\nabla} p}{q\, n\, B^2} = \frac{mv^2\, \underline{\nabla} n}{2\, q\, n\, B} \quad .$$

The density gradient $\underline{\nabla} n$ for 90° pitch angle particles can be expressed in terms of particle gyroradius, r_L, and gyrofrequency, Ω, and the density change δn ($= n_A - n_B$) between opposite detector look directions, as

$$|\underline{\nabla} n| = \frac{\delta n}{2 r_L} = \frac{\delta n\, \Omega}{2v} = \frac{\delta n\, e\, B}{2mv} \quad .$$

$$\therefore \quad |\underline{v}_D| = \pm \frac{v\, \delta n}{4 \bar{n}}$$

where $\bar{n}$ is the mean density $((n_A + n_B)/2)$ and sign distinguishes charge species. Using the data in Fig. 3/11, and noting $n = fv^3$, we derive the $\underline{v}_D$ values in Table 3/4. $\delta v(W)$ is the velocity shift at constant f and mean particle energy W between the data sets at successive downscan and upscan. Clearly without correction for $\underline{E} \times \underline{B}$ drift, diamagnetic drift was capable of producing the observed flux changes. Also, since $\underline{v}_D$ is velocity dependent, the flux asymmetry it produces will increase with particle energy. We noted such an increase in Fig. 3/10.

To complete this section let us summarize our conclusions concerning the flows / anisotropies perpendicular

to $\underline{B}$. These were due to a combination of $\underline{E} \times \underline{B}$ drift and diamagnetic drift. $\underline{E} \times \underline{B}$ drift, $\underline{u}_E$, dominated the LANL/Garching thermal energy response, while diamagnetic drift, $\underline{v}_D$, dominated the MEPE response. Using $\lambda_\perp \sim 5000$ km we find $\underline{v}_D \sim 10$ km/s at thermal energies while $\underline{u}_E$ contributed a third and a seventh to distribution function changes at $W \sim 30$ keV and $W \sim 150$ keV respectively (see Fig. 3/11). As these competing effects were in phase and thus always giving rise to 'flow' in the same direction, the wave-induced pressure gradient, $\underline{\nabla} p_\perp$, must have been antiparallel to the wave electric field $\underline{E}$. This implies that $\underline{\nabla} p_\perp$ and the perpendicular wave phase motion had significant east-west components (Chapter 5).

3.3.6 Flows parallel to $\underline{B}$

Plasma motion along $\underline{B}$ was perhaps the most surprising hydromagnetic vortex feature of all, especially when one considers that without an oscillating field-aligned flow, a vortex would not have been seen. Parallel flow occurs when there is a greater flux of particles moving in one direction along $\underline{B}$ than in the opposite direction, or more precisely, when non-uniformity exists in particle bounce phase distribution. Information on the temporal and spatial nature of the acceleration source which gives rise to the bounce phase dependence, can be furnished from Fig. 3/15, where in the same format as Fig. 3/10, proton flow is compared at various energies in the Y_{GSE} (approximately field-aligned) direction. Firstly, though, let us recognise that in a collisionless plasma it is difficult to sustain a coherent parallel flow

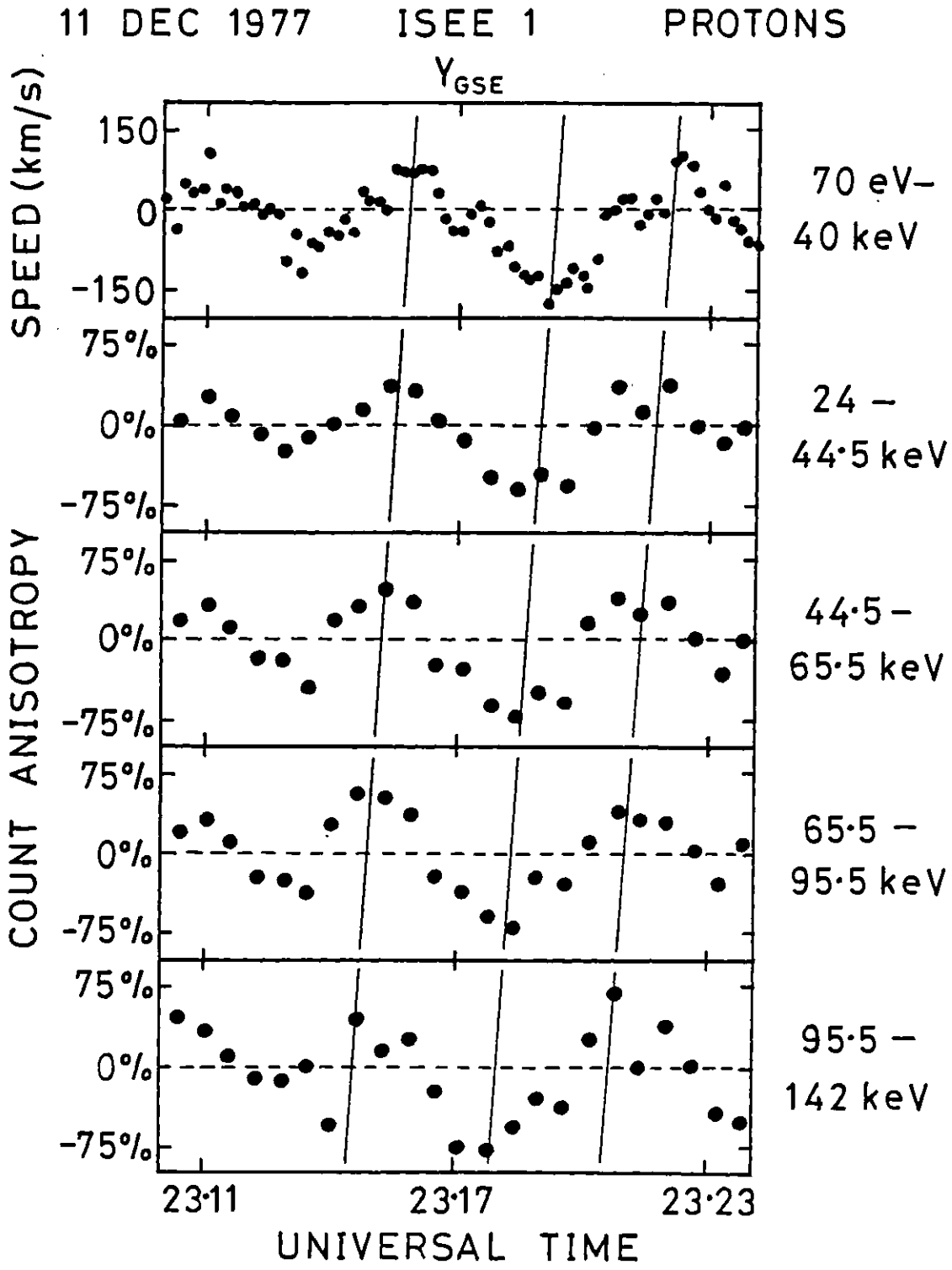

FIGURE 3/15. Proton flows as a function of energy in the Y_{GSE} (approximately field-aligned) direction, with the guidelines helping to illustrate the energy dispersion.

because energy dispersion will occur. One would therefore expect to see evidence for dispersion in Fig. 3/15, and indeed this is so, for careful inspection, using the guidelines through the peaks and troughs, shows that high energies led in phase throughout the event.

The energisation source for the parallel flows was clearly extended in time, and was not instantaneous. This is implicit from the sinusoidal form of the $v_{||}$ signal, for if the acceleration had been transient, the $v_{||}$ signals would have appeared as Dirac delta functions. The constancy in dispersion slopes is another significant feature in Fig. 3/15, and indicates firstly, that there was not a single interval of energisation with particle mirroring producing the changes in parallel flow direction, and secondly, that the source was spatially localised. The slopes can be used to calculate a source distance, d_s, and a time, T_o, when the source acceleration was a maximum, by using the time of flight equations

$$t_i = T_o + \frac{d_s}{v_i}$$

$$t_j - t_i = d_s\left(\frac{1}{v_j} - \frac{1}{v_i}\right) \quad ,$$

where t_i, t_j are the arrival times for ions of energies i,j having velocities v_i, v_j. Assuming for the purpose of calculating velocities that the ions are protons, a least squares analysis gives $d_s = (14 \pm 2)R_E$ and $T_o = -(90 \pm 10)$ secs., where the errors are for the 1σ level and T_o is expressed relative to times of extrema in the thermal $v_{||}$ flows at the spacecraft. Although useful as a guide, the values for d_s and T_o are not absolute. The time of

flight calculation does not include, amongst other things, the effect of a particle's previous acceleration history. The concepts introduced above will be developed in a detailed theoretical interpretation and modelling of energy dispersion in Section 5.4.

Day	11 Dec., 1977 (DAY 345)
Time	23.10 - 23.24 U.T.
Location	Plasma Sheet
Radial Distance	$8 \cdot 8 R_E$
Local Time $_{GSM}$	0437
Latitude $_{GSM}$	12°
Dipole L-shell	$\sim$ 10
DZ	$5 \cdot 6 R_E$
Spacecraft separation	GSM : (-10,760, -350) km MVA : (-350, -290, 710) km

Table 3/1 Spacecraft position and separation parameters for the 11th. December, 1977, vortex event. Separations are from ISEE 2 to ISEE 1. DZ is the distance above the Fairfield (1980) model neutral sheet.

WAVE	
T	360s
Cycles	2
$b_{\parallel}$	11 γ
$b_{\perp}$	10 γ
$v_{\parallel}$	90 km/s
$v_{\perp}$	120 km/s
Field displacement, $\xi_{\perp}$	0·9 R_E
Harmonic	Fundamental
Phase speed, ω/k	∿ 14 km/s
Parallel phase speed, $(\omega/k)_{\parallel}$	∿ 600 km/s
$\lambda_{\parallel}$	∿ 34 R_E
$\lambda_{\perp}$	(5±1)x10³ km
BACKGROUND	
B	65 γ
P	0·85x10⁻⁹ N/m²
β	0·5
n	0·9 cm⁻³
($n_{H^+} m_{H^+}$%, $n_{O^+} m_{O^+}$%, $n_{He^+} m_{He^+}$%)	(65, 25, 10)
γ(ratio of specific heats)	1·75±0·11
Alfvén speed, A	1300 km/s
Sound speed, c_s	1000 km/s
Thermal speed, v_{th}	1000 km/s (5·5keV)
Thermal bounce period (L=10), $\tau_{b_{th}}$	340s (α_{eq}=0°) / 180s (α_{eq}=90°)
$\underline{B}_{GSM}$ (observed)	(23, 59, 7) γ
$\underline{B}_{GSM}$ (field model)	(4, 54, 24) γ
K_p	4⁺

Table 3/2 Wave and background parameters for the 11th. December, 1977, vortex event. Apart from the mass density values, which were obtained from Lennartsson et al.(1979), all plasma parameters were determined from the LANL/MPI ion plasma data. The oscillating wave quantities are defined by their amplitude. Dr. P. Hedgecock's 1977B field model for $K_p > 2$ conditions was used for the $\underline{B}_{GSM}$ model calculation.

	W(keV)	$\lvert\nabla n\rvert_{max}$ (cm^{-4})	n_o (cm^{-3})	$\lambda_\perp$ (km)
$\lvert B \rvert$ decreasing (23.14–23.17UT)	29	$7{\cdot}7\times10^{10}$	$8{\cdot}6\times10^{-2}$	3500
	39	$1{\cdot}4\times10^{10}$	$2{\cdot}0\times10^{-2}$	4500
	50	$8{\cdot}5\times10^{11}$	$1{\cdot}7\times10^{-2}$	6300
	60	$3{\cdot}4\times10^{11}$	$5{\cdot}5\times10^{-3}$	5100
$\lvert B \rvert$ increasing (23.17–23.20UT)	29	$11{\cdot}3\times10^{10}$	0·16	4400
	39	$2{\cdot}1\times10^{10}$	$2{\cdot}8\times10^{-2}$	4200
	50	$12{\cdot}1\times10^{11}$	$1{\cdot}9\times10^{-2}$	4900
	60	$8{\cdot}5\times10^{11}$	$1{\cdot}1\times10^{-2}$	4100

Table 3/3. A listing of parameters associated with the calculation of the transverse wave wavelength, $\lambda_\perp$, using 90° pitch angle MEPE ion data. Values are given at four ion energies, W, during half-wave cycles when $\lvert B \rvert$ was decreasing and increasing.

W(keV)	v(km/s)	$\delta n/\bar{n}$	δv(km/s)	v_D(km/s)
35	2550	1·75	400	1100
55	3250	1·81	600	1500
80	3920	1·84	700	1800
120	4800	1·67	800	2000

Table 3/4. Diamagnetic drift speeds, v_D, and associated parameters (see text for details), calculated at four ion energies, W, from the distribution function data in Fig. 3/11.

CHAPTER 4

HYDROMAGNETIC VORTICES - FURTHER EVENTS

4.1 Introduction

To provide a firmer observational basis for our theoretical interpretation of the vortex phenomenon (Chapter 5), this Chapter will describe data for three further vortex events which occurred within three weeks of, and at similar locations to, the 11th. December event. Table 4/1 lists the events, their locations, and other parameters of interest. Although our data sets for these additional events lack MEPE and mass composition information, the loss of these will not substantially affect the points we wish to make. In particular we will show that the 11th. December event (hereafter termed event 1) was not atypical.

4.2 28th. December, 1977, event.

Fig. 4/1 shows ISEE 2 magnetometer and 2D thermal plasma data for this vortex event, displayed in GSE coordinates. Since the event, as the others we shall be discussing, occurred during a low bit rate orbit, the plasma measurements were not recorded at their highest possible resolution - the data in Fig. 4/1 are 24s samples. Nevertheless, the rotational motion in plasma flow longitude is clear, especially between 17.20 and 17.40 U.T. when perturbations maximized in the field magnitude and direction. A semblance of clockwise flow motion can also be seen prior to 17.20, when the field did not exhibit marked oscillatory motion. However, inspection of the 3D flow velocity data

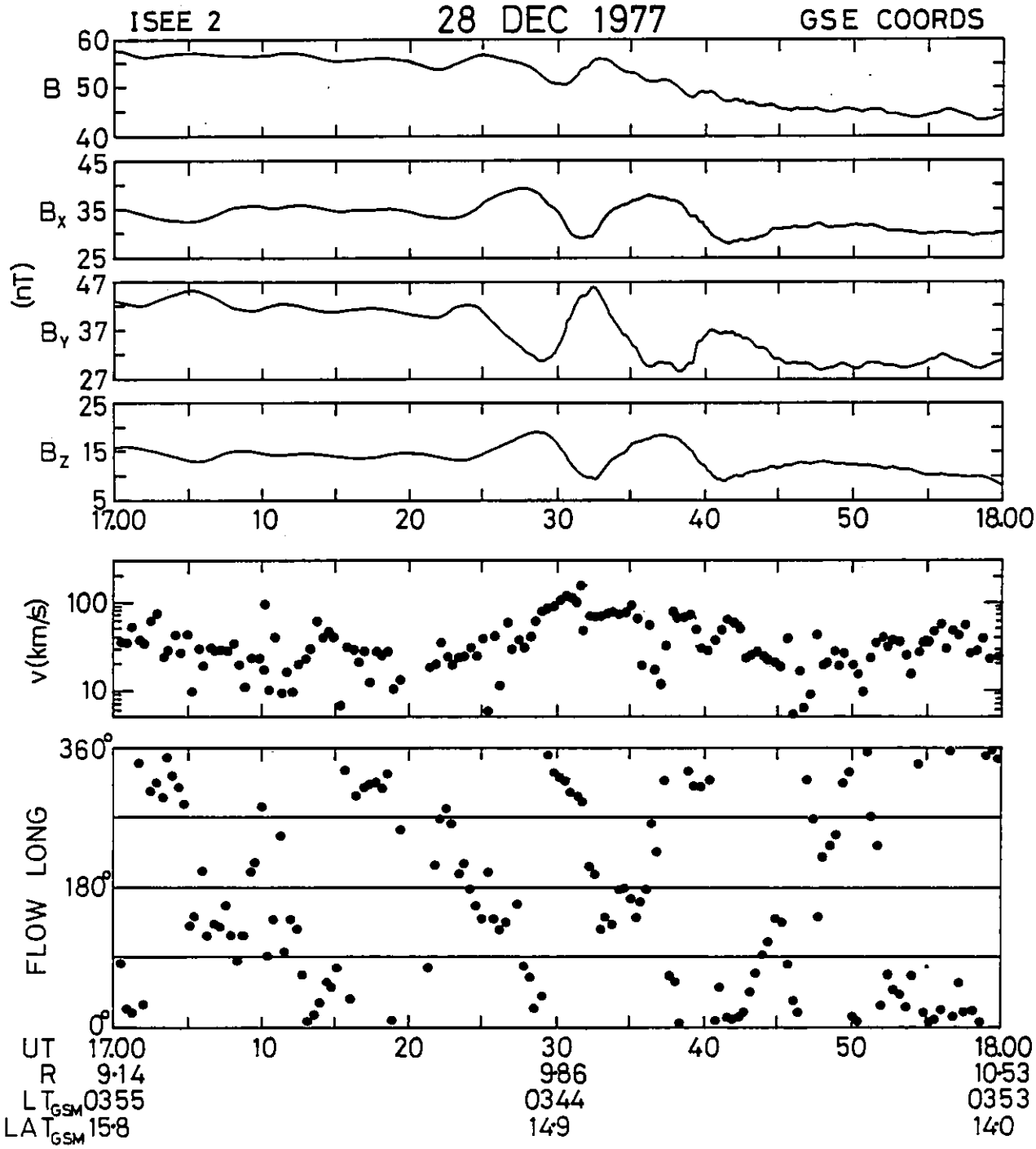

FIGURE 4/1. GSE coordinate display of ISEE 2 magnetometer and 2D thermal plasma data for the 28 December, 1977 vortex event. The field measurements are 12s averages plotted every 4s, while the plasma data have 24s resolution.

shows the flow speed low and flow direction variable at this time, indicating that caution should be exercised in interpreting the 2D flow measurements. Significantly, as for event 1, the ambient field lay almost in the ecliptic, and showed tailward bending compared with the Peter Hedgecock 1977B field model prediction (see Table 4/2 for both a comparison of the observed and model field values and a list of other background and wave parameters). The decrease in background field strength across the main vortex event is also noteworthy; event 1 exhibited a similar sharp $|\underline{B}|$ decrease (see Fig. 3/3). Density, δn, and temperature, δT, perturbations (not shown) also accompanied the 28th. December event (hereafter called event 2). δn and δT were in phase with each other, and in antiphase with the field strength oscillation. Using equation (1) we obtain a value for γ of $1{\cdot}7 \pm 0{\cdot}4$, a figure consistent with isotropy in plasma pressure. The high error results from the analog and low resolution nature of the data used.

The data are expressed in MVA coordinates in Fig. 4/2. Magnetometer recordings from both spacecraft are shown in the top panel, with ISEE 1 depicted as the solid trace, while ISEE 2 flow velocity data are displayed in the bottom panel at the highest 3D time resolution available (48s). The noisiness of the latter data is due partly to the time resolution, but also to the bulk speeds being so low that they were close to the instrument threshold value. The MVA coordinate system used here is identical to that employed in Fig. 3/2, so X_{MVA} is directed outwards in the meridian (approximately northward). The low pass filter cut-off frequencies used for defining the mean field

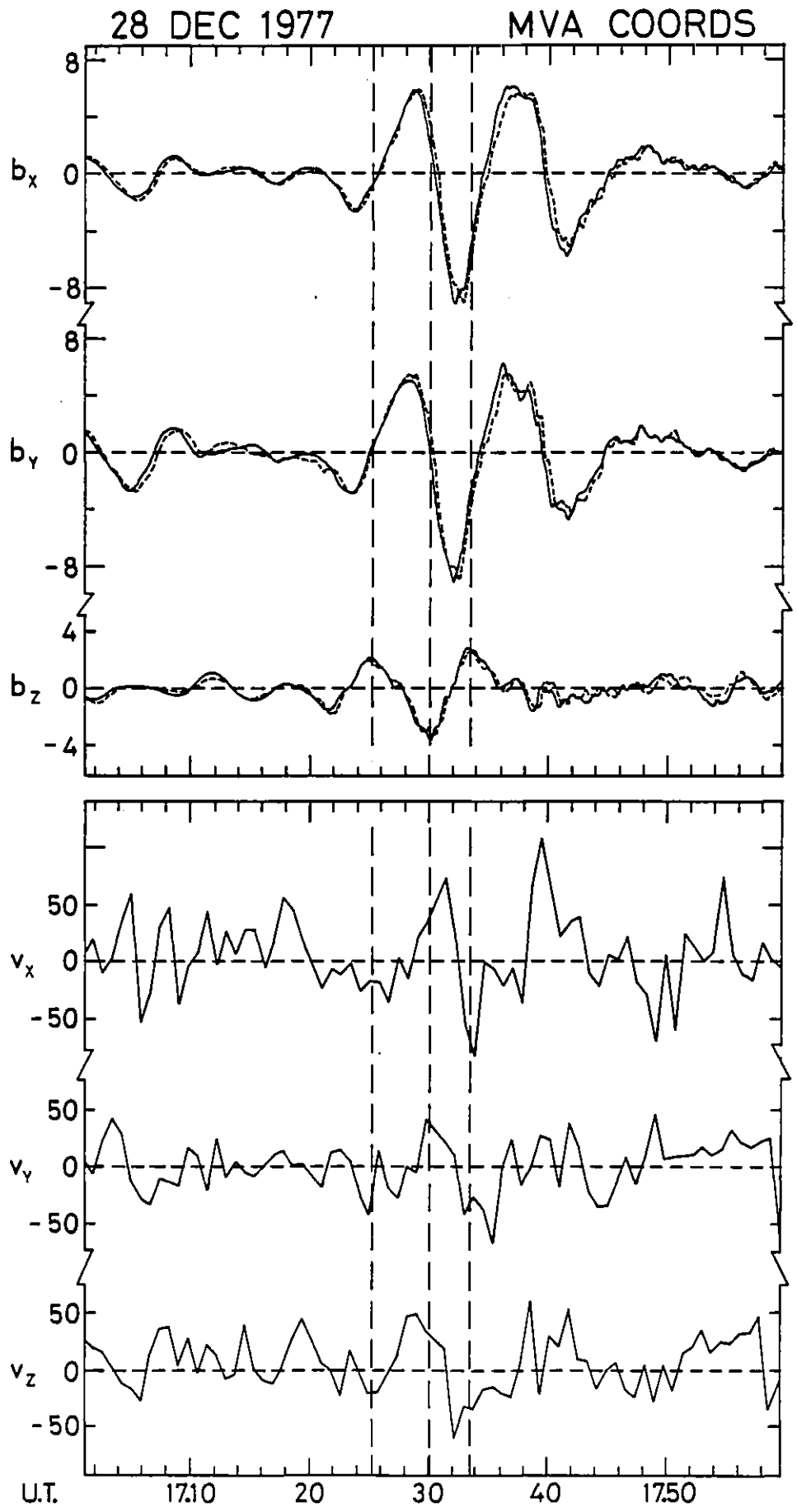

FIGURE 4/2. Magnetic field observations (in nT) and thermal plasma flow measurements (in km/s) displayed in MVA coordinates. The magnetometer data are shown for both spacecraft, with ISEE 1 as the solid trace, and the flow data from ISEE 2.

direction were also the same as described previously. Vertical guidelines through the b_z maxima and minima assist in studying the vortex $\underline{B}$ and $\underline{v}$ phase relations which are summarised below:

(a) The signal transverse polarisation is linear. Although clear in the field data, the poor quality of the flow data makes this feature more difficult to see in the latter.

(b) $v_{\parallel} \sim -i\underline{v}_{\perp}$, that is $v_{\parallel}$ and $v_{\perp}$ are of similar magnitude and $v_{\parallel}$ leads $\underline{v}_{\perp}$ in phase by $\sim 90°$. Since the ambient field lay in the ecliptic (Fig. 4/1), this indicates that clockwise vortex motion is seen (when viewed from above the ecliptic) because the flow parallel to $\underline{B}$ leads in quadrature the flow perpendicular to $\underline{B}$. In the field data, the parallel component also leads the perpendicular wave component in phase, but the phase angle is $\sim 120°$, and $b_{\parallel}$ is only a third the amplitude of $b_{\perp}$.

(c) $\underline{b}_{\perp}$ leads $\underline{v}_{\perp}$ in phase by $\sim 90°$; a phase relation one would expect for a fundamental mode standing structure at the spacecraft location.

(d) $b_{\parallel}$ leads $v_{\parallel}$ in phase by $\sim 150°$.

Two other features are worth noting from Fig. 4/2. Firstly, there is a phase shift in the wave signal between the spacecraft during the vortex. Cross spectral analysis shows that ISEE 1 leads in phase by $10° \pm 3°$ where the error is at the 3σ level. Secondly, field oscillations also occur prior to the vortex event - these have a similar period to, but a smaller amplitude than, those seen during the vortex itself.

The Poynting flux computed from $\underline{B}$ and $\underline{v}$ is displayed in MVA coordinates in Fig. 4/3. This shows that the electromagnetic energy flow maximised in amplitude during the vortex event, and was directed principally along the field. As S_z oscillated in sign at twice the wave frequency and there was no nett field-aligned Poynting flux, one concludes that the field oscillations had standing structure, as would be expected from $b_\perp$ and $v_\perp$ being in quadrature (Fig. 4/2). The small nett perpendicular Poynting flux was directed in the same sense as for event 1, namely southwards ($-X_{MVA}$) and tailwards ($-Y_{MVA}$).

ISEE 2 pressure data for event 2 are plotted in Fig. 4/4. The centre and bottom panels show respectively, the LANL/MPI plasma pressure, p, and the field pressure for the hour interval from 17.00 U.T. The plasma pressure is the sum of proton and electron pressures - these constituent pressures oscillated in phase, with the electron pressure smaller in magnitude by a factor of ten. The top panel shows the total pressure, $p_T (= p+B^2/2\mu_0)$, during the 20 minute interval of main vortical flow. Although gas and magnetic pressures clearly oscillated in antiphase, it is interesting to note that perturbations were not always in <u>strict</u> antiphase - for example, there was a slight phase offset at 17.30. In comparison with event 1 there was better pressure balance here, though p_T was still dominated by the magnetic pressure perturbation. Unlike event 1, the decrease in $B^2/2\mu_0$ across event 2 was partly matched by a corresponding increase in gas pressure.

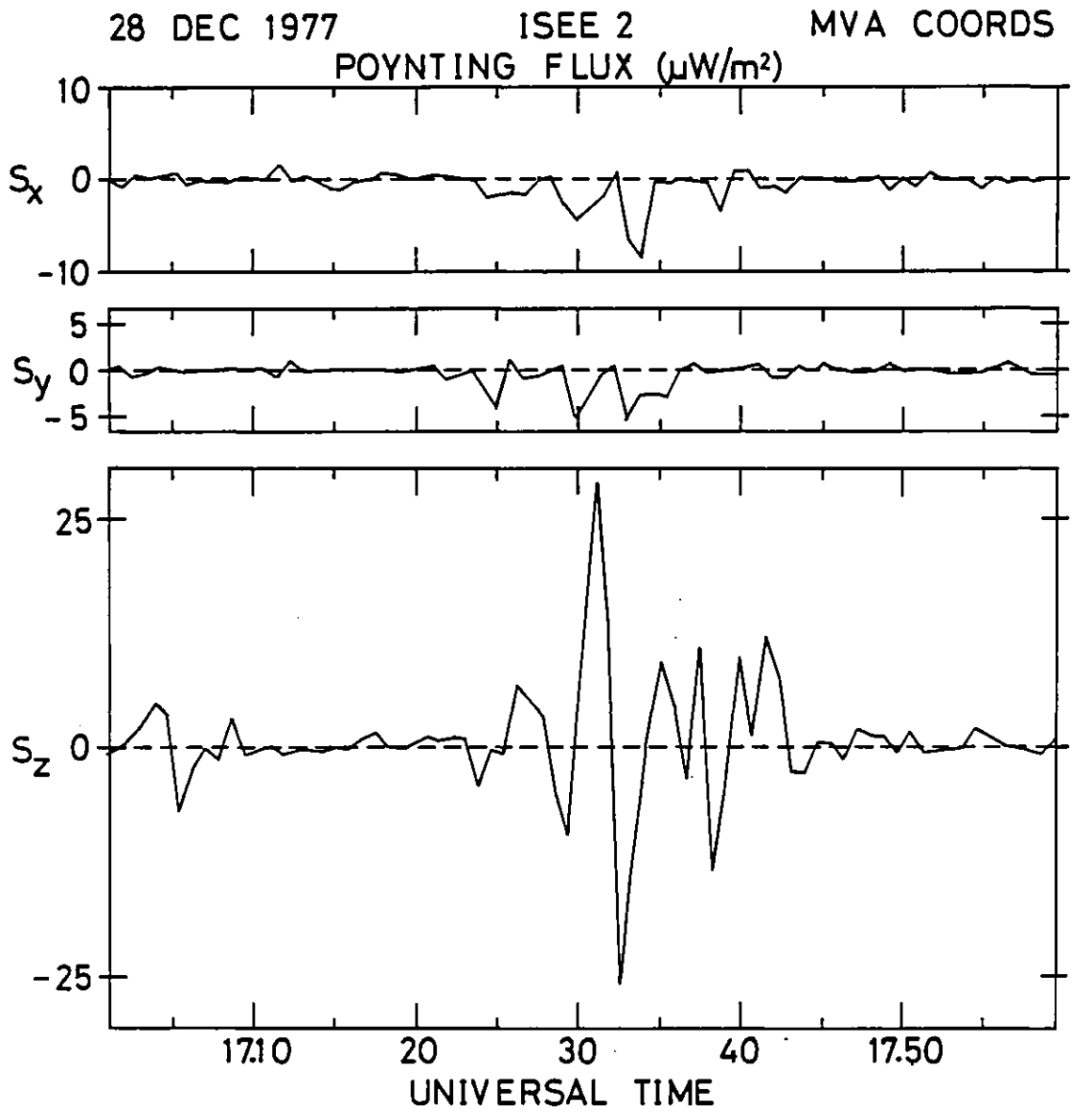

FIGURE 4/3. Computed Poynting flux in field-aligned coordinates.

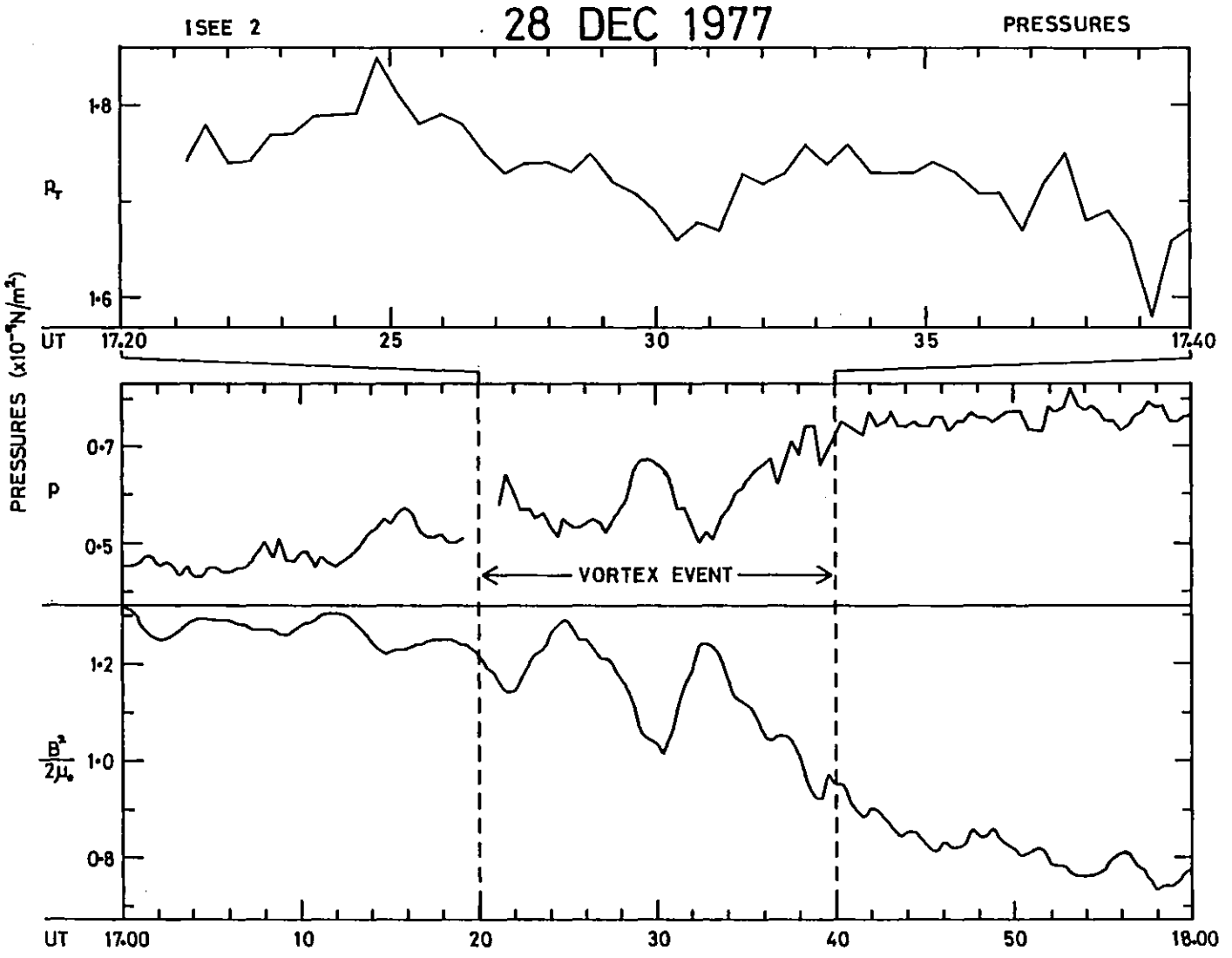

FIGURE 4/4. Plasma and magnetic field pressure data for the28 December, 1977 vortex. The scalar thermal plasma pressure (p) is the sum of proton and electron pressures. The total pressure (p_T) is shown only for the interval of vortical flow.

The plasma beta increased from $\sim 0{\cdot}35$ at 17.00 to $\sim 1{\cdot}0$ at 18.00.

Let us now briefly discuss the observations in Figs. 4/1 - 4/4, by comparing them in more detail with the corresponding features of event 1. The spacecraft location, the number of wave cycles, the wave period and several features of the wave polarisation (e.g. the linear transverse polarisation, and the quadrature phase relations between $v_{\parallel}$ and $v_{\perp}$, and between $b_{\parallel}$ and $b_{\perp}$), are almost identical for the two events. Furthermore, the phase relation between $v_{\perp}$ and $b_{\perp}$ and the presence of the change in particle energy, are strong reasons for feeling that event 2, like event 1, oscillated in the fundamental mode. The antiphase gas and magnetic pressure perturbations, the direction of nett transverse Poynting flux and the tailwards bending in the background field are additional points of similarity. The electric field data, although we have not shown them, are, as they were for event 1, consistent here also with the perpendicular flows resulting from $\underline{E} \times \underline{B}$ drift.

There are also some interesting features which differ between the events. For example, the phase lag between $b_{\parallel}$ and $v_{\parallel}$ is noticeably larger for event 2. Event 1 has a nett Earthwards field-aligned Poynting flux, but no such nett flux exists for event 2. One other difference is the presence of the background pressure change across event 2.

How does the perpendicular wave wavelength, $\lambda_{\perp}$, compare? The phase difference in the wave signal between ISEE-1 and 2 (Fig. 4/2) can be used to calculate $\lambda_{\perp}$ for event 2, by applying the arguments (based on $\underline{\nabla}.\underline{b} = 0$) that we used in

Section 3.2.4. to obtain the transverse wave propagation direction for event 1. The transverse wave field schematic in Fig. 4/5 compares the orientation of the transverse wave phase fronts (assumed to be parallel to $b_\perp$) with the spacecraft separation vector across $\underline{B}$. Clearly because these directions are not so closely aligned as they were for event 1 (see Fig. 3/5), there are stronger reasons for expecting a phase shift between the spacecraft in event 2. A phase shift is indeed observed (Fig. 4/2) - the phase lag being $\sim 10°$. Using this phase lag and the spacecraft separation of 240 km at right angles to $b_\perp$, with the wave period of 500s, one obtains $\lambda_\perp$ as $\sim$ 8,500 km and the transverse wave phase speed as $\sim$ 17 km/s; values which are similar to, though slightly larger than, the corresponding figures for event 1. Since ISEE 1 led in phase the wave was propagating northward and tailward, a direction which agrees with that deduced for event 1.

Although event 2 did not possess a nett field-aligned Poynting flux, there may have been a nett field-aligned heat flux associated with it. Arguments identical to those put forward in Section 3.2.4., indicate that since δp and $v_\parallel$ oscillated in phase (compare Figs. 4/2 and 4/4), the event had a nett Earthwards field-aligned heat flux. Similarly one can argue there was a nett heat flux perpendicular to $\underline{B}$, for as $\delta p_\perp$ and $b_\parallel$ oscillated in antiphase, the transverse heat flux would have been directed opposite to $\underline{S}_\perp$. Because this would reduce further the already small $S_\perp/S_\parallel$ ratio (Fig. 4/3), one concludes that the wave to a first approximation was guided along $\underline{B}$.

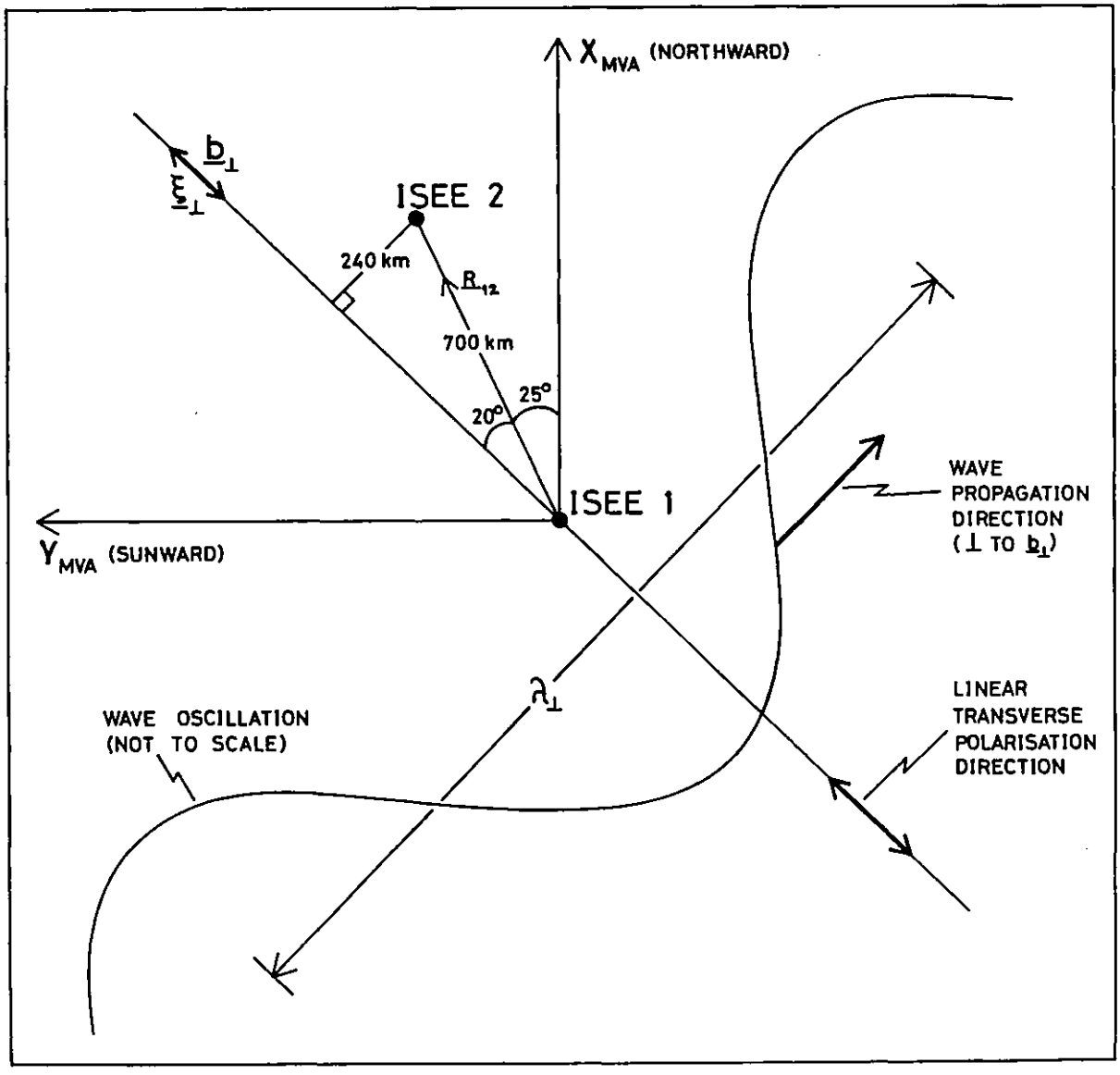

FIGURE 4/5. Transverse wave schematic of the 28 December, 1977 vortex. From the angular offset between $\underline{R}_{12}$ and the direction of transverse wave polarisation, coupled with the fact that ISEE 1 led in phase by 10° (Fig. 4/2), we deduce that $\lambda_{\perp}$ was ∿ 8500km.

The background change in pressure across event 2 merits comment. Prima facie,pressure data in Fig. 4/4 could be taken to suggest that this was a spatial feature, with the wave pressure perturbations a consequence of this supposed ambient gradient convecting back and forth across the spacecraft. However, Fig. 4/2 shows this was not the case, for one would expect δp to be in quadrature with $v_\perp$ under such circumstances, and such a phase relation was not seen. We favour instead the interpretation used to explain the MEPE data of event 1, namely that the pressure oscillations here were also wave-induced and propagated past the spacecraft at the transverse wave phase speed; ideas which will be further developed in Chapter 5.

4.3 9th. December, 1977, event.

This vortex event was recorded on ISEE's outbound passage, exactly one orbit before event 1. Although K_p values differed considerably during the two events, 0+ in this case as against 4+ for event 1, the wave magnetic polarisations were quite similar.

Table 4/2 shows that the background field again lay in the ecliptic, but this time its direction agreed very well with the field model prediction. ISEE-1 and 2 magnetometer data for the event are displayed in MVA coordinates in the top panel of Fig. 4/6; the coordinate directions being defined as described in Section 3.2.2. The lower panels of the Figure show ISEE 2 2D flow longitude (GSE coordinate) and speed data at 24s resolution; 3D flow measurements have not been obtained for this event.

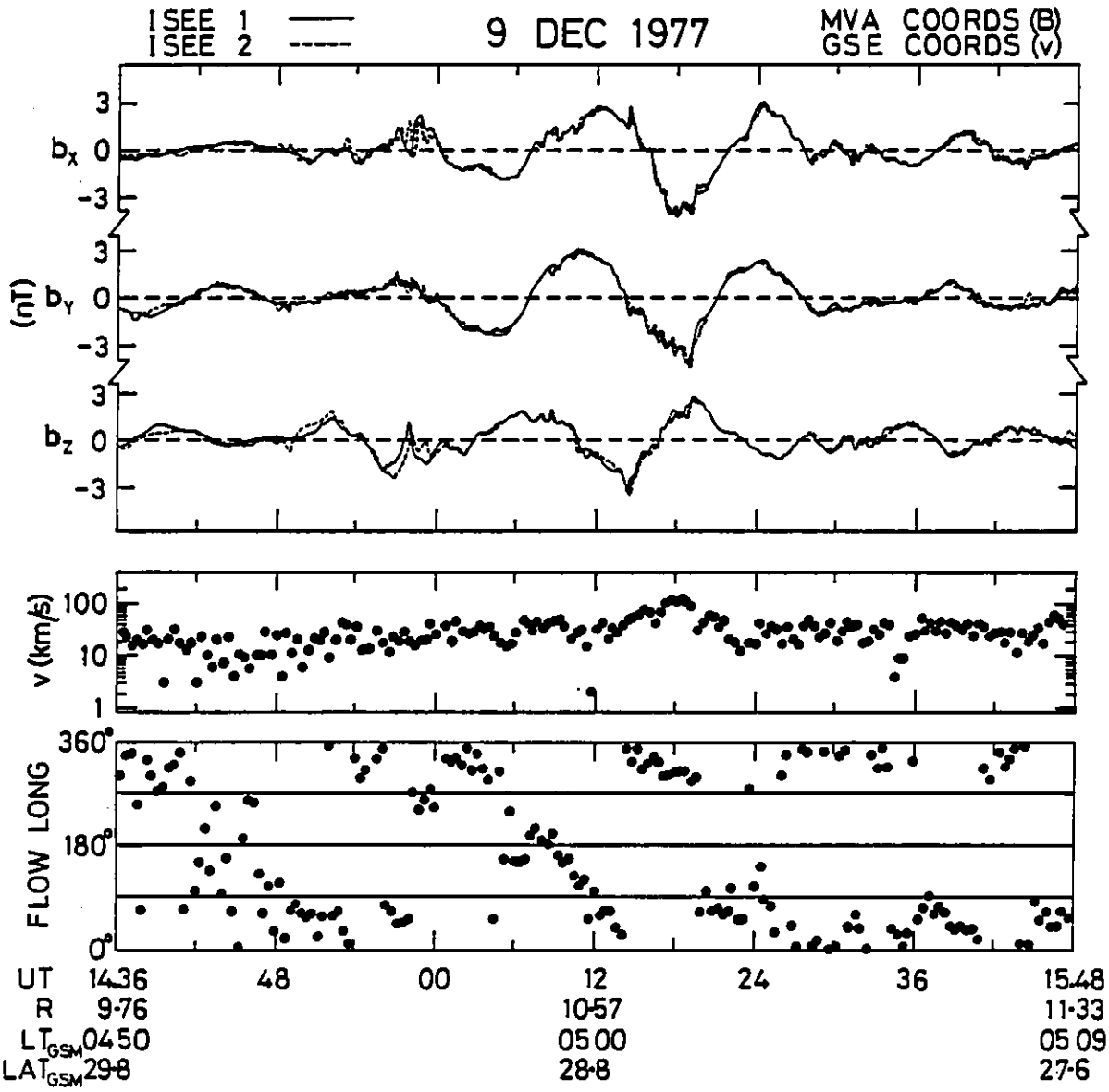

FIGURE 4/6. ISEE-1 and 2 magnetometer measurements displayed in MVA coordinates, with ISEE 2 2D plasma flow data shown at 24s resolution in GSE coordinates, for the 9 December, 1977 vortex event.

The transient nature of the event, the presence of both transverse and compressional magnetic signals which maximized in amplitude during the main interval of vortical flow (when $|\underline{v}|$ was above background), the approximately linear transverse polarisation and the quadrature phase difference between $b_{||}$ and $b_{\perp}$, are all features characteristic of the two other vortex events. Since the GSE longitude of $\underline{B}$ was $\sim 75°$, it is clear that part of the flow rotation was field-aligned. Density and temperature perturbations were also features of the event, and in common with events 1 and 2 they combined to give a plasma pressure perturbation which was in antiphase with $b_{||}$. The ratio of specific heats γ was $1{\cdot}7 \pm 0{\cdot}4$.

There were also features which distinguished this event from the vortex events studied previously. In particular, despite the spacecraft transverse separation in this case being favourable for measuring a phase difference (if our earlier arguments are correct), no phase lag was seen in the signals between the spacecraft. This implies that the perpendicular wavelength was several R_E. A second difference (data not shown) was the absence across the event of background changes in either $|\underline{B}|$ or p.

4.4 19th. December, 1977, event - spacecraft/ ground comparison.

As in the 9th. December event, our fourth vortex example (19th. December, 1977) occurred when magnetic activity was very low. Despite its consequent low amplitude, this event is of interest because spacecraft local time and Universal Time were very similar (see

Table 4/1). As a result the spacecraft magnetic 'footprint' was over the Greenwich Meridian, and adjacent to the ground network of digital magnetometers deployed by Dr. Bill Stuart of the IGS at Edinburgh, as part of the U.K. International Magnetospheric Survey effort. The 19th. December event therefore provides an opportunity for studying the ground signature of a vortex seen in space.

Spacecraft magnetometer and thermal plasma data for the event are shown in Fig. 4/7. Field data from both spacecraft are displayed in our usual MVA coordinate system, while the plasma data consist of ISEE 2 flow longitude measurements plotted in GSE coordinates. The latter show evidence for two cycles of flow rotation commencing just before 4.40. Although 3D flow data are not presented as they did not resolve the event, it is clear that with $\underline{B}$ again in the ecliptic (Table 4/2) and directed towards 80° GSE - longitude, the event had an oscillating parallel flow component. Significantly, $v_{||}$ lagged $b_{||}$ in phase by $\sim$ 120°, a phase relation similar to that observed for the other vortex events. It is also significant to note that while a compressional magnetic signal was seen in association with the vortex motion, a transverse signal (of longer period) which occurred prior to 4.40, disappeared during the event. This suggests that field compression is important for vortex motion, an observation which is supported by the other vortex events we have studied. Inspection of Figs. 3/2, 4/2 and 4/6 will show that the onset and cessation of vortex flow is associated more with the

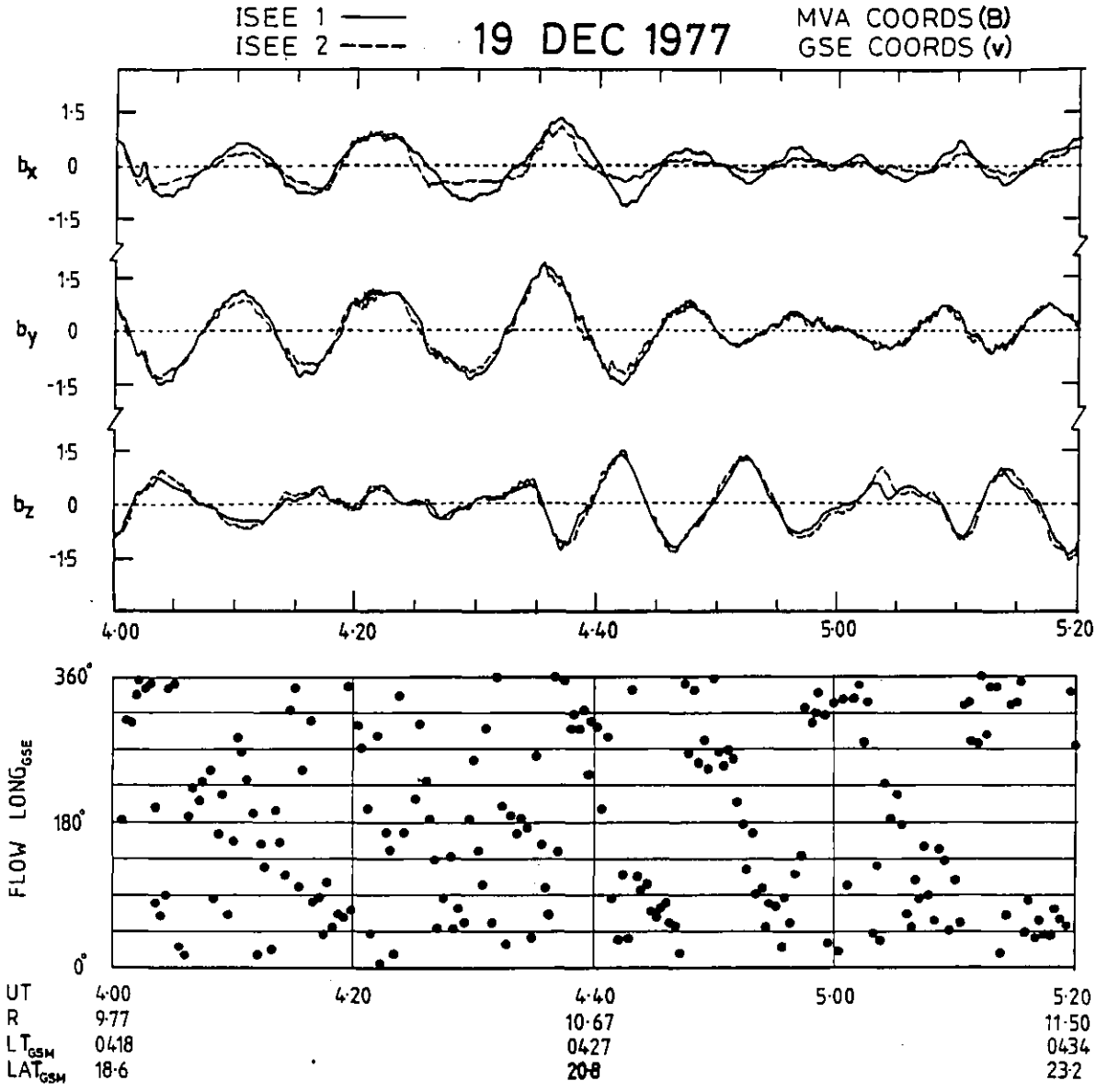

FIGURE 4/7. ISEE-1 and 2 magnetometer data (nT) shown in MVA coordinates, with ISEE 2 plasma flow longitude measurements displayed in GSE coordinates, for the 19 December, 1977 vortex.

presence of $b_{||}$ rather than $b_{\perp}$.

Let us now investigate the event as it appeared on the ground. Fig. 4/8 shows the locations of the IGS magnetometers, together with the positions of other ground observatories from which magnetograms of the event have been obtained (via the World Data Service). The latter include two Southern Hemisphere stations, Syowa and Mawson, which are shown by their conjugate points. The ISEE magnetic 'footprint' determined using the Olson-Pfitzer (1977) field model, is plotted for a 90 minute interval which spans the event. The 'footprint' was located NNE of Iceland - a position very similar to that predicted by the Mead-Fairfield field model.

Ground and spacecraft data are compared in Fig. 4/9, where the ISEE 1 Z_{MVA} field component is plotted with the vertical (Z) ground field components from Tromsø and Eidar. Clearly the three signals begin oscillating together at about 4.35, just prior to the vortex onset, and cease together at about 5.00 when the flow rotation disappears. Signals from the two Icelandic stations, Reykjavik and Eidar, provide evidence for westward phase motion. Fig. 4/10 shows NE magnetic component data from these stations during the vortex event; the vertical guide-lines helping to emphasise that Eidar (the easterly station) led in phase. Cross spectral analysis shows the phase difference was $\sim 80°$, which, as the stations are separated by 4° in longitude, corresponds to an E-W wavelength of $\sim 18°$ or an m - number of ~ 20. Mapping this to L $\sim$ 12 in the magnetosphere gives an azimuthal wavelength $\sim 4R_E$; a value which would be sufficiently

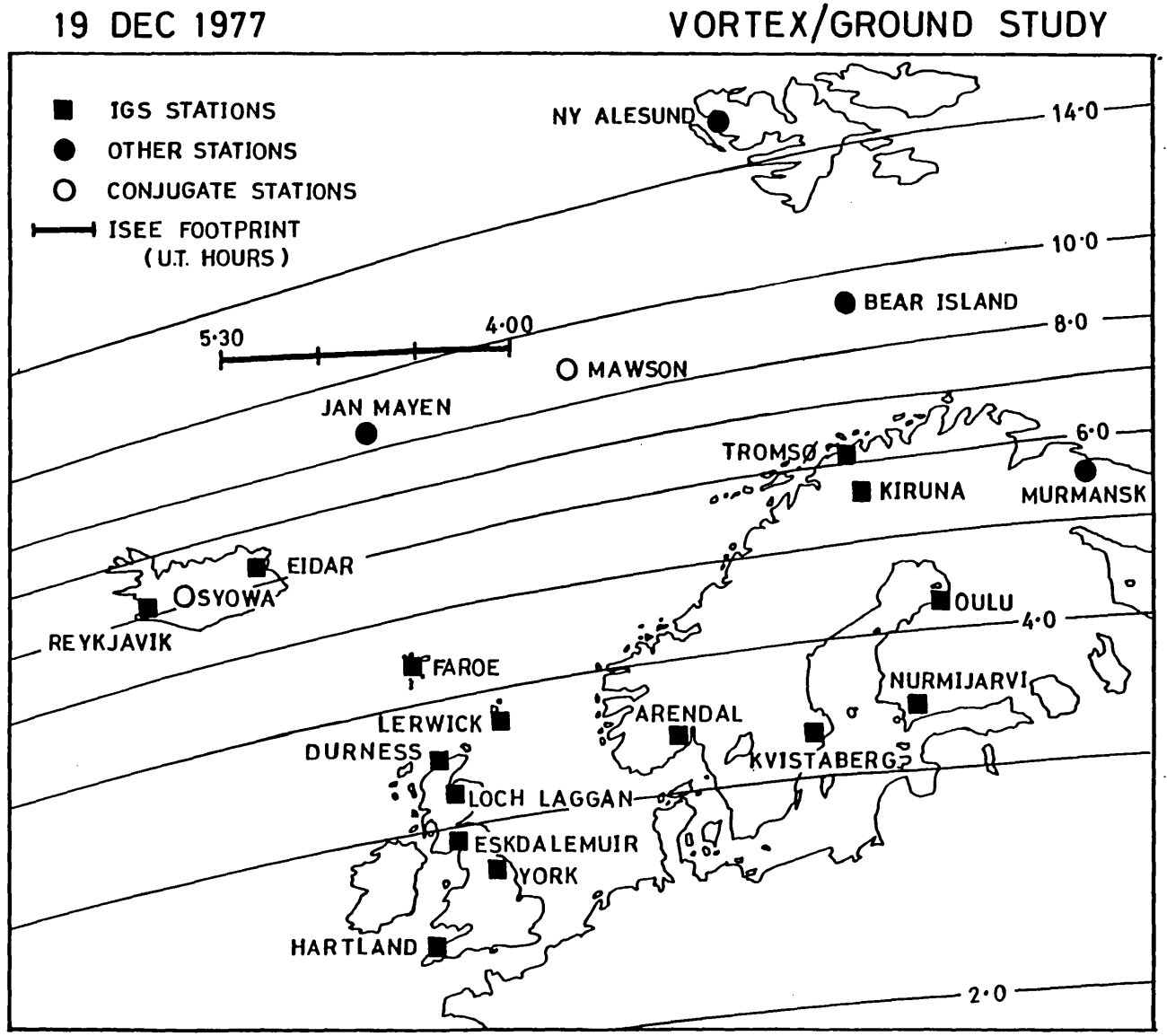

FIGURE 4/8. Ground magnetometer stations, field line L-values, and predicted ISEE magnetic footprint (Olson-Pfitzer (1977) model) for the 19 December, 1977 vortex.

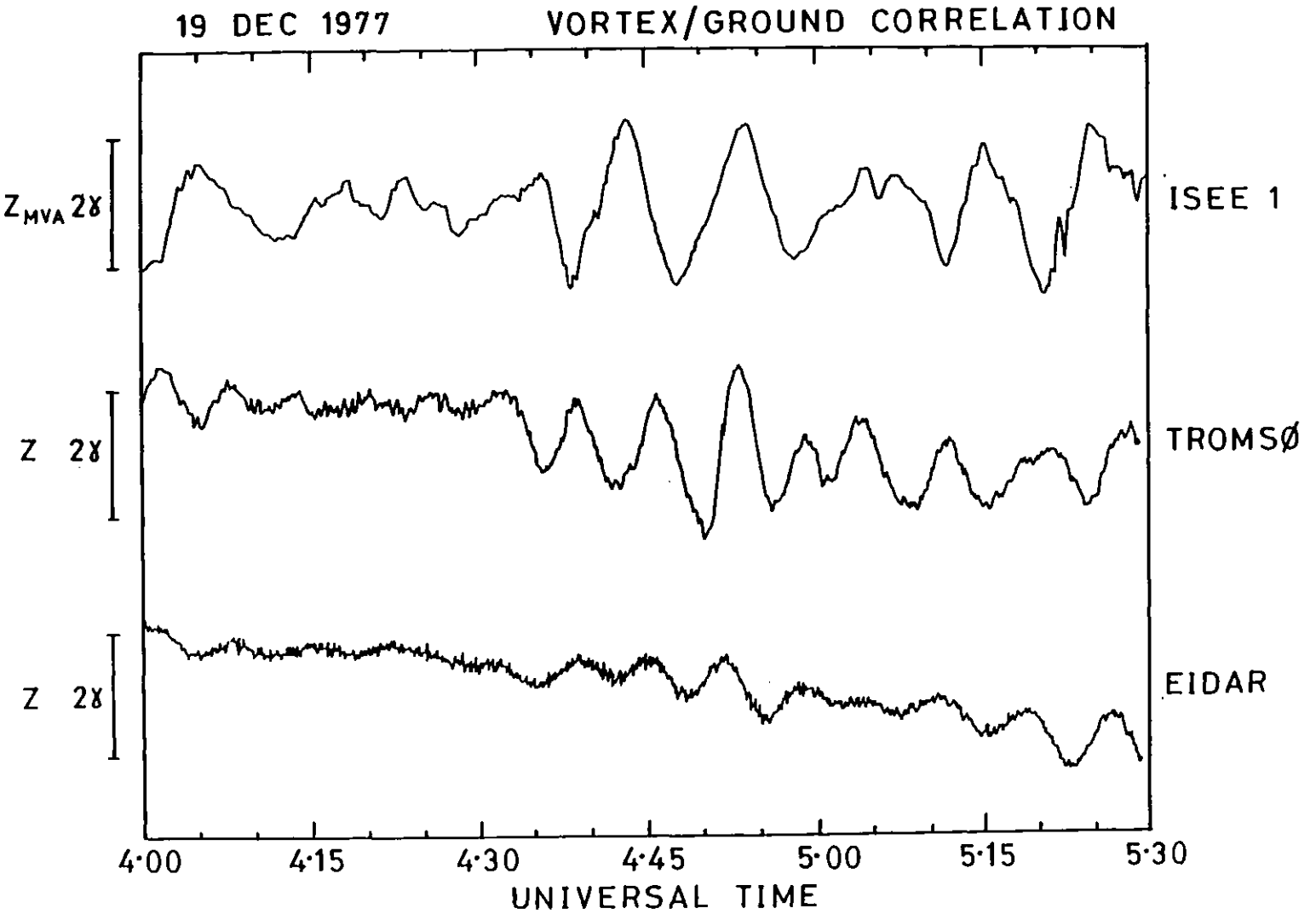

FIGURE 4/9. Ground and spacecraft magnetic field data for the 19 December, 1977 vortex. The compressional (Z_{MVA}) field component is shown for the space signal, while the ground recordings are illustrated by the vertical (Z) component.

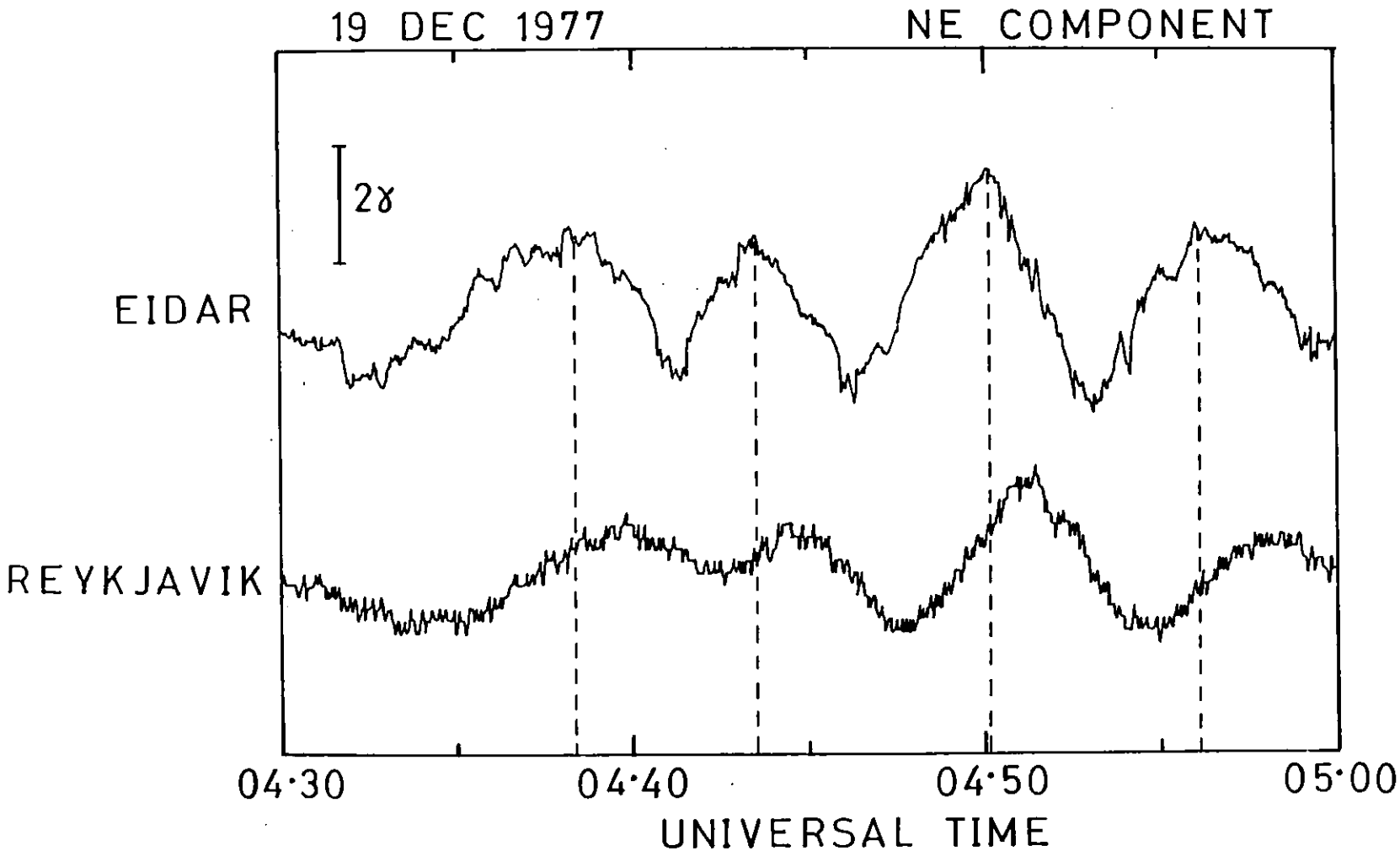

FIGURE 4/10. NE component ground magnetometer recordings from the two Icelandic stations Eidar and Reykjavik, showing that the easterly station (Eidar) lad in phase by ∿ 80° during the vortex event.

large to explain the absence of a phase lag in the signals between the spacecraft (Fig. 4/7). However, it seems this wavelength was variable, because although we have not shown the data, Tromsø leads Eidar in phase by ∿ 130° in the NE wave component, and as the stations are separated in longitude by 38°, a 130° phase difference is inconsistent with there being a multiple number of 18° wavelengths between Tromsø and Eidar.

Despite the synchronism in onset and cessation of signals seen on the ground and in space - which suggests a connection between space and ground phenomena, there is a curious difference between the signals; they have different frequencies. While the wave in space oscillates with a 9 minute period, the ground signals in the auroral zone have a 7 minute period. Evidence for 7 minute activity is also seen further south at Faroes, Lerwick, Kiruna, Oulu and Nurmijarvi - that is, down to L ∿ 3·5 which would be inside the plasmapause. At higher L-values signal behaviour is similarly surprising. Bear Island and Jan Mayen observe 7 minute oscillations while Ny Alesund at L ∿ 16 on Spitzbergen does not see the event. However, the two Antarctic stations, Syowa and especially Mawson, do show evidence for longer period (∿ 10 minute) activity. Unfortunately, the scale of the normal magnetograms from these latter stations makes it impractical to display their data.

As a flux tube should oscillate at the same frequency along its entire length, the fact that the periods of signals seen on the ground and in space do not appear to match,

indicates that none of our ground stations, at least in the northern hemisphere, are underneath the flux tube foot. This is not too surprising considering the limited ground network coverage in the predicted footprint vicinity. The difference in period between the conjugate stations is unexpected however, and indicates a need for improvement in present magnetospheric field models. On this point one should note that the Olson - Pfitzer (1977) model is only applicable to field lines which cross the equator within $15R_E$, a condition which this event may only marginally satisfy.

Another feature of interest is the event's large scale nature. Ground pulsations which appeared to occur nearly simultaneously with the vortex in space, were seen over a longitude range of at least 55° from Murmansk in W. Russia to Reykjavik in W. Iceland. We have also shown that signal excitation was not localised in L-shell.

4.5 Discussion.

The vortex events studied here all occurred at a similar location in the dawn plasma sheet. They were chosen for study for three main reasons. Firstly, they were among the initial vortices to be detected, secondly, they possessed clear magnetic signatures - something seldom seen in other events, and lastly, they were among the better 'rotators' in that their flow rotations were fairly complete. Uninterrupted flow rotations were rare; although flows rotated in a particular sense, there were frequently gaps in flow

longitude where the rotation was incomplete.

As Hones et al. (1981) show, vortices are seen throughout the plasma sheet tailwards of the dawn-dusk meridian. The plasma β conditions under which they occur vary from $\beta \gtrsim 1$ in the events studied here to $\beta \sim 20$ for events near the tail equator. In fact, several vortex events in early 1978 occurred in the neutral sheet vicinity. An example is the event on 2nd. March, the plasma flow data for which is published in Hones et al. (1978). β was of order 20 throughout the hour of data shown, and three neutral sheet crossings occurred - at 16.37, 16.39 and 16.53 U.T. The neutral sheet events clearly deserve study, though interpretation of the field response will be complicated by the unsteady background field. We note for the moment that the 2nd. March vortex possesses two significant features that are common to other events; an oscillating parallel flow component and periodic perturbations in plasma pressure.

Although the 19th. December vortex is the only event of which a detailed ground/spacecraft study has been made by us, Hones et al. (1981) report another example (10th. March, 1979) of ground pulsations seen in association with a vortex in space. In the latter event, periods observed in space and on the ground appear to match, despite the spacecraft field line ($L \sim 15$) probably mapping someway northwards of the auroral zone stations whose data was used. The form of the ground signals - in particular those of the 19th. December event - suggests the disturbance was being driven rather than resonating. A structure resonating on nightside flux

tubes would rapidly damp, owing to poor ionospheric reflection, while the data in Figs. 4/9 and 4/10 show oscillations of approximately constant amplitude.

Considering their range in period (5-20 minutes), region of occurrence, and general irregular waveform, it is not unreasonable to suggest that the hydromagnetic vortices may be associated with some of the pulsations recorded on the ground and classed as Pi3 -type. Pi3's are long-period irregular nightside pulsations which have yet to receive much attention, though Saito (1978) has recently reviewed their properties in regard to substorms. Interestingly, an example in this review of a Pi3 observed simultaneously on the ground and in space - that recorded by OGO-5 at 16.00 U.T. on 8th. June, 1968, and taken from McPherron and Coleman (1971) - shows features in the space signal which are similar to the vortex features we have noted. Furthermore, OGO-5's location was close to the region where the vortex events discussed here were seen.

Day	9 Dec., 1977 (DAY 343)	19 Dec., 1977 (DAY 353)	28 Dec., 1977 (DAY 362)
Time (UT)	15.00	04.45	17.30
Radial Distance (R_E)	10·3	10·8	9·9
Local Time $_{GSM}$	0457	0428	0345
Latitude $_{GSM}$	29°	21°	15°
Dipole L-shell	14·9	∿ 14	12·7
DZ (R_E)	6·9	8·5	4·4
Spacecraft separation GSM (km):	(-60,570,-390)	(30,710,-350)	(180,860,-260)
Spacecraft separation MVA (km):	(-470,-200,470)	(-420,-270,610)	(-630,-300,590)

Table 4/1 Spacecraft position and separation parameters for the vortex events discussed in Chapter 4. DZ is the Fairfield (1980) model neutral sheet distance, and spacecraft separations are from ISEE 2 to ISEE 1.

Day	9 Dec., 1977	19 Dec., 1977	28 Dec., 1977
$B(\gamma)$	45	32	52
$p(\times 10^{-9}\ N/m^2)$	0·2	0·2	0·5
β	0·2	0·5	0·5
$n\ (cm^{-3})$	0·85	0·75	0·85
γ	1·7±0·4	1·5±0·4	1·7±0·4
A (km/s)	1000	800	1200
C_s (km/s)	600	700	1000
v_{th} (km/s)	500 (1·3keV)	600 (2keV)	900 (4keV)
$\tau_{b_{th}}$ (s) $\alpha eq=0°$	1050	800	510
$\tau_{b_{th}}$ (s) $\alpha eq=90°$	560	430	270
$\underline{B}_{GSM}$ (observed)	(12,44,3)γ	(6,30,5)γ	(32,36,18)γ
$\underline{B}_{GSM}$ (model)	(13,43,5)γ	(5,32,3)γ	(20,35,18)γ
K_p	0+	0+	2−
T(s)	850	550	500
Cycles	2	2	2
$b_{\parallel}$ (γ)	3	1·3	3
$b_{\perp}$ (γ)	5	$2·0 > b_{\perp} > 0·6$	10
$v_{\parallel}$ (km/s)			50
$v_{\perp}$ (km/s)			80
$\xi_{\perp}$ (R_E)			1·0
ω/k (km/s)			∿ 17
$(\omega/k)_{\parallel}$ (km/s)			∿ 420
$\lambda_{\parallel}(R_E)$			∿ 33
$\lambda_{\perp}(R_E)$			1·3

Table 4/2 Background parameters (top) and wave parameters (bottom) for the vortex events listed in Table 4/1. The plasma values were determined from the LANL/MPI ion data and have not been corrected for any heavy ion contribution. Blanks in the wave parameters are due to the 3D velocity data either being unavailable (9 Dec), or unsuitable for resolving the event (19 Dec). The oscillating wave quantities are defined by their amplitude.
Dr. P. Hedgecock's 1977B field model for $K_p < 2$ conditions was used for determining the $\underline{B}_{GSM}$ model values.

CHAPTER 5

THEORETICAL INTERPRETATION

5.1 MHD modes in a hot isotropic plasma

To seek an interpretation for the vortex events described in Chapters 3 and 4 we start by reviewing MHD wave theory appropriate to a collisionless, hot and homogenous plasma in a uniform magnetic field. Our theoretical working will assume that plasma pressure remains isotropic exactly as is observed.

In the hydromagnetic limit the parallel and perpendicular momentum equations are

$$\rho \frac{\partial^2 \xi_{\parallel}}{\partial t^2} = -\frac{\partial \delta p}{\partial s} \qquad (4).$$

$$\rho \frac{\partial^2 \underline{\xi}_{\perp}}{\partial t^2} = -\underline{\nabla}_{\perp}\left(\delta p + \frac{B b_{\parallel}}{\mu_o}\right) + \frac{B}{\mu_o}\frac{\partial \underline{b}_{\perp}}{\partial s} \quad , \qquad (5)$$

where $\xi_{\parallel}$, $\underline{\xi}_{\perp}$ are wave-induced plasma displacements along and across $\underline{B}$. ρ is the plasma mass density, and δp is the pressure perturbation produced by the wave. s is a coordinate along the background field, $\underline{B}$, and $\underline{\nabla}_{\perp}$, defined as

$$\underline{\nabla}_{\perp} = \underline{\nabla} - \frac{\underline{B}}{B}\frac{\partial}{\partial s} \quad ,$$

is the gradient operator perpendicular to $\underline{B}$.

Faraday's Law and the frozen-field condition relate $\underline{b}$ and $\underline{\xi}$ as follows:

$$\underline{b} = \underline{\nabla} \times (\underline{\xi} \times \underline{B}) = \underline{\nabla} \times (\underline{\xi}_{\perp} \times \underline{B}) \quad ,$$

so that in a uniform ambient field,

$$b_{\parallel} = -(\nabla \cdot \underline{\xi}_{\perp})\underline{B} = -(\nabla_{\perp} \cdot \underline{\xi}_{\perp})\underline{B} \qquad (6)$$

and $$\underline{b}_{\perp} = B \frac{\partial \underline{\xi}_{\perp}}{\partial s} \cdot \qquad (7)$$

The absence of any change in background pressure either before, during, or after three of the four vortex events, indicates that gradient convection effects were not the dominant cause of the wave pressure perturbations. A similar conclusion also pertains to the 28th. December vortex, where a change in ambient pressure did occur. Consequently we assume that the plasma was uniform, and in that case the equation of continuity gives the wave-induced density change, δn, as

$$\delta n = -n\left(\frac{\partial \xi_{\parallel}}{\partial s} + \nabla_{\perp} \cdot \underline{\xi}_{\perp}\right) \cdot \qquad (8)$$

Combining δn with the thermodynamic equation of state gives

$$\delta p = -\gamma p\left(\frac{\partial \xi_{\parallel}}{\partial s} + \nabla_{\perp} \cdot \underline{\xi}_{\perp}\right) \qquad (9)$$

for the pressure perturbation in an isotropic plasma. The terms in equation (9) have important physical meanings. By analogy with equation (6), the $\nabla_{\perp} \cdot \underline{\xi}_{\perp}$ term describes changes in gas and magnetic pressures due to the flux tube cross section expanding and contracting. The $\xi_{\parallel}$ term describes particle squeezing along $\underline{B}$ in response to parallel acceleration.

The substitution of equations (6), (7) and (9) into equations (4) and (5) gives the following coupled equations:

$$\frac{\partial^2 \xi_{\parallel}}{\partial t^2} = c_s^2 \frac{\partial^2 \xi_{\parallel}}{\partial s^2} + c_s^2 \left(\nabla_{\perp} \cdot \frac{\partial \underline{\xi}_{\perp}}{\partial s}\right) \qquad (10)$$

$$\frac{\partial^2 \underline{\xi}_{\perp}}{\partial t^2} = \nabla_{\perp}\left[(c_s^2 + A^2)(\nabla_{\perp} \cdot \underline{\xi}_{\perp})\right] + A^2 \frac{\partial^2 \underline{\xi}_{\perp}}{\partial s^2} + c_s^2 \nabla_{\perp}\left(\frac{\partial \xi_{\parallel}}{\partial s}\right) \quad , \qquad (11)$$

where c_s and A are the sound and Alfvén speeds respectively.

Equations (10) and (11) contain three separate wave modes, the first of which can be separated out by the use of equation (11) to find the equation satisfied by $\underline{\nabla}_\perp \times \underline{\xi}_\perp$; namely

$$\left(\frac{\partial^2}{\partial t^2} - A^2 \frac{\partial^2}{\partial s^2}\right)(\underline{\nabla}_\perp \times \underline{\xi}_\perp) = 0 \quad . \tag{12}$$

This equation describes the Alfvén mode, alternatively known as the shear, transverse or intermediate mode. It is characterised by

$$\xi_{||} = 0, \quad \underline{\nabla} \cdot \underline{\xi} = 0 \text{ and } b_{||} = 0 \quad . \tag{13}$$

The other two wave modes contained in equations (10) and (11) are the fast and slow magnetosonic modes. These are both characterised by

$$\underline{\nabla} \cdot \underline{\xi} = \underline{\nabla}_\perp \cdot \underline{\xi}_\perp + \frac{\partial \xi_{||}}{\partial s} \neq 0 \quad ,$$

$$\text{and } \underline{\nabla}_\perp \times \underline{\xi}_\perp = 0 \quad . \tag{14}$$

From equations (10) and (11), the equations obeyed by $\partial \xi_{||}/\partial s$ and $\underline{\nabla}_\perp \cdot \underline{\xi}_\perp$ are

$$\left(\frac{\partial^2}{\partial t^2} - c_s^2 \frac{\partial^2}{\partial s^2}\right) \frac{\partial \xi_{||}}{\partial s} = c_s^2 \frac{\partial^2}{\partial s^2}(\underline{\nabla}_\perp \cdot \underline{\xi}_\perp) \tag{15}$$

$$\left(\frac{\partial^2}{\partial t^2} - c_s^2 \nabla_\perp^2 - A^2 \nabla^2\right)(\underline{\nabla}_\perp \cdot \underline{\xi}_\perp) = c_s^2 \nabla_\perp^2 \left(\frac{\partial \xi_{||}}{\partial s}\right) \quad . \tag{16}$$

Eliminating $\partial \xi_{||}/\partial s$ or $(\underline{\nabla}_\perp \cdot \underline{\xi}_\perp)$ from equations (15) and (16) gives a fourth order equation for the two coupled magnetosonic wave modes, for example:

$$\left(\frac{\partial^4}{\partial t^4} - (c_s^2 + A^2)\nabla^2 \frac{\partial^2}{\partial t^2} + c_s^2 A^2 \nabla^2 \frac{\partial^2}{\partial s^2}\right)(\underline{\nabla}_\perp \cdot \underline{\xi}_\perp) = 0 \quad . \tag{17}$$

For plane waves, equation (17) is a quadratic in phase speed, V_p, with roots:

$$V_{p\pm} = \tfrac{1}{2}\left((A^2+c_s^2) \pm \left((A^2+c_s^2)^2 - 4c_s^2A^2\cos^2\phi\right)^{\frac{1}{2}}\right) \qquad (18)$$

where $\cos\phi = \hat{\underline{B}}.\hat{\underline{k}}$. The modes corresponding to the + and - signs in equation (18) are called fast and slow because their phase speeds are respectively always greater than, or less than, that of an Alfvén mode wave propagating in the same direction. There is a crucial kinematic difference between these modes. In the fast wave, $\partial\xi_{\parallel}/\partial s$ and $\underline{\nabla}_{\perp}.\underline{\xi}_{\perp}$ oscillate in phase, while in the slow mode they oscillate in antiphase. This produces an important dynamical difference. From equations (6) and (9), the fast wave has magnetic and gas pressure perturbations which are in phase, while in the slow wave they are in antiphase.

Another type of hot plasma hydromagnetic wave mode we have not considered is the drift wave, (e.g. see Southwood and Lanzerotti, 1979), and, in particular, the drift mirror instability (Hasegawa, 1969, and Kremser et al., 1981). As this mode occurs only in the presence of pressure anisotropy and/or ambient density gradients - features which the vortex events did not have - we discount such modes in this analysis. Similarly, we can also dismiss the Kinetic Alfvén wave (Hasegawa and Mima, 1978) as a possibility, since it has a wavelength perpendicular to $\underline{B}$ of order the thermal Larmor radius. Even the transverse wavelength of event 1, which at $\sim$ 5000 km appears to have been somewhat smaller than the perpendicular wavelengths of the other events, was $\sim$ 30 thermal Larmor radii.

5.2 Vortex wave mode identification.

From the brief review in the previous section, it seems that only one MHD mode has properties appropriate to the vortex events - the slow mode. The slow mode is compressive, it has magnetic and gas pressure perturbations which oscillate in antiphase, and since it does not cause particle displacement that is solenoidal, it can also induce motion along $\underline{B}$ as described by equations (15) and (16). The fast mode can also produce field-aligned flow and is also compressive, but since its phase velocity exceeds both c_s and A, gas and magnetic pressures oscillate in phase. The Alfvén mode (equation 13) has neither perpendicular compressive motion, $\underline{\nabla}_\perp . \underline{\xi}_\perp$, nor parallel 'squeezing' motion, $\xi_\parallel$, associated with it.

In the past the slow mode has often been ignored in collisionless plasma theory because it should be strongly Landau damped. As the vortex events discussed here only lasted a couple of cycles, they could well have been absorbed by collisionless damping. The nett energy flux Earthwards along $\underline{B}$ may be further evidence for Landau damping, since absorption would render standing structure imperfect and parallel phase motion would result (see Newton et al., 1978). However, other absorption processes may also have been important, especially damping due to poor nightside ionospheric reflection.

The wave phase speed is another feature which favours the signal being a form of slow mode. This may be shown by first rotating the data into the MVA coordinate system employed in Fig. 3/14, where z is along $\underline{B}$, $\underline{b}_\perp$ and $\underline{\xi}_\perp$ are polarised in the y- direction, and $\underline{E}$ (from $\underline{E}=-\underline{u}_E \times \underline{B}$) is

polarised in the x- direction, and then applying Faraday's Law. This gives

$$\begin{aligned} b_x &= E_y \frac{k_z}{\omega} \simeq 0 \\ b_y &= -E_x \frac{k_z}{\omega} \\ b_z &= E_x \frac{k_y}{\omega} - E_y \frac{k_x}{\omega} \ ; \end{aligned} \tag{19}$$

expressions which are valid assuming that $E_z=0$, in agreement with observations. Equation (19) defines the wave phase speed along $\underline{B}$, $(\omega/k)_{||}$, in terms of measured quantities; namely

$$\left(\frac{\omega}{k}\right)_{||} = \frac{\omega}{k_z} = \left|\frac{E_x}{b_y}\right| \ .$$

For event 1 (11th. December), the amplitudes of b_y and E_x were 10γ and $\sim$ 6mV/m respectively, the latter value either being measured from Fig. 3/9 or determined using $\underline{E}=-\underline{u}_E x \underline{B}$ with $\underline{u}_E \sim 100$ km/s. In event 2 (28th. December), b_y was again 10γ, and assuming that $|\underline{u}_E| \sim |\underline{v}_\perp| \sim 80$ km/s, E_x was $\sim$ 4mV/m. Consequently the vortex parallel wave phase speeds were $\sim$ 600 km/s (event 1) and $\sim$ 400 km/s (event 2); values which are clearly less than the local Alfvén, A, and sound, c_s, speeds (see Tables 3/2 and 4/2), and therefore consistent with the vortex being a form of slow mode. It is unlikely this conclusion will be affected by our calculation of A and c_s for event 2 ignoring the presence of heavy ions.

Let us take the wave phase speed discussion a stage further and consider the phase speed one would expect if the vortex was a pure slow mode wave, and compare this value with that predicted by the slow mode dispersion relation. In order for the wave vector, $\underline{k}$, to satisfy

both Ampere's Law and Faraday's Law, $\underline{b}.\underline{k}=0$. Consequently, if the vortex was solely a slow mode, that is, having $\underline{B}$, $\underline{b}$ and $\underline{k}$ coplanar (equation 14), the ratio of $b_{\parallel}$ to $|\underline{b}_{\perp}|$ would give the angle ϕ relative to $\underline{B}$ at which it should propagate. It then follows from equation (19) that the slow mode wave phase speed would be

$$\left(\frac{\omega}{k}\right)_s = \frac{E_x}{b_y}\cos\phi \quad .$$

For events 1 and 2, ϕ was respectively $\sim 48°$ and $\sim 17°$, so one would expect $(\omega/k)_s$ to be $\sim$ 400 km/s (event 1) and $\sim$ 380 km/s (event 2). Using these ϕ values and the values for A and c_s given in Tables 3/2 and 4/2, one obtains from the slow mode dispersion relation (equation 18), $(\omega/k)_s \sim$ 320 km/s (event 1) and $\sim$ 810 km/s (event 2). Although there is good agreement between the $(\omega/k)_s$ values for event 1, the factor of two discrepancy for event 2 suggests that this vortex may not have been a slow mode. In fact the agreement for event 1 is misleading, because despite many features to the contrary, this event, and by analogy the other vortex events described here, can <u>not</u> be pure slow mode waves as we now show.

From equations (6) and (9):

$$\frac{Bb_{\parallel}}{\mu_o} = -(\underline{\nabla}_{\perp}\cdot\underline{\xi}_{\perp})\rho A^2 \qquad (20)$$

and

$$\delta p = -\left(\frac{\partial \xi_{\parallel}}{\partial s} + \underline{\nabla}_{\perp}\cdot\underline{\xi}_{\perp}\right)\rho c_s^2 \quad . \qquad (21)$$

Since c_s^2/A^2 $(=\gamma\beta/2)$ was of order 1 and Fig. 3/3 shows $Bb_{\parallel}/\mu_o$ was of order $2\delta p$, it follows from equations (20) and (21) that

$$\frac{\partial \xi_{\parallel}}{\partial s} \sim -\frac{3}{2}(\underline{\nabla}_{\perp}\cdot\underline{\xi}_{\perp}) \quad . \qquad (22)$$

On writing $\underline{\nabla}_\perp = i\underline{k}_\perp$,

it follows that $$\underline{\nabla}_\perp \cdot \underline{\xi}_\perp = ik_\perp \xi_\perp \cos\theta, \qquad (23)$$

where θ is the angle between the directions of perpendicular phase propagation and perpendicular polarisation, the latter taken to be linear. As it is observed that $|v_\parallel| \sim |\underline{v}_\perp|$ (equivalently $|\xi_\parallel| \sim |\underline{\xi}_\perp|$), comparison of equations (22) and (23) shows that

$$|k_\perp \cos\theta| \sim k_\parallel^{-1} \quad . \qquad (24)$$

Furthermore, since $\lambda_\parallel$ $(=(\omega/k)_\parallel T$, where T is the wave period) was of order $34R_E$, equation (24) implies that the perpendicular scale of signal variation was similarly large unless θ was large.

Although the absence of a phase difference between the spacecraft indicates that the scale of variation parallel to $\underline{\xi}_\perp$ was much greater than the spacecraft separation along $\underline{\xi}_\perp$, (about 450 km), there are strong reasons for feeling that $\lambda_\perp$ was small and that θ was large. In particular, the NOAA/SEL energetic particle data provide clear evidence for transverse wave localisation, and for propagation approximately at right angles to $\underline{\xi}_\perp$ (Section 3.3.5). A large θ is also implied by our arguments (Section 3.2.4) based on $\underline{\nabla}.\underline{b}=0$. One can estimate θ by first noting that a sinusoidal plane signal of period T has its peak-to-peak plasma displacement, $\xi_{O\perp}$, and field line velocity amplitude, $v_{O\perp}$, related by

$$\xi_{O\perp} = \frac{v_{O\perp} T}{\pi} \quad .$$

The $v_{O\perp}$ values for events 1 and 2 were 100 km/s and 80 km/s respectively, giving $\xi_{O\perp}=1{\cdot}8R_E$ (event 1) and $\xi_{O\perp}=2{\cdot}0R_E$ (event2). Combining equations (6) and (23) and then substituting these field line displacement values together with the appropriate $b_\parallel$ to B ratio and $\lambda_\perp$ value (see Tables 3/2 and 4/2), one

obtains $\theta=88\cdot7°$ (event 1) and $\theta=88\cdot1°$ (event 2).

Since the signals have $\theta\neq0°$, the vortices can not be pure slow mode waves, because for a slow mode

$$\underline{\nabla}_{\perp} \times \underline{\xi}_{\perp} = 0 \quad .$$

The vortices must therefore be the result of coupling between the slow mode and the Alfvén mode because the Alfvén mode has

$$\underline{\nabla}_{\perp} \times \underline{\xi}_{\perp} \neq 0 \quad .$$

The polarisation plot in Fig. 5/1 illustrates the vortex wave propagation for event 1 in three dimensions. The diagram also shows the difference between the actual wave and a pure slow mode wave. The display is in the rotated MVA coordinate system employed in Fig. 3/14, and to aid orientation the directions of the MVA axes have been sketched on a GSE- coordinate axes plot in the lower part of the Figure. $\underline{k}_V$ and $\underline{k}_S$ denote respectively the wave vectors for the vortex wave and for a pure slow mode wave; for the former $\theta \sim 89°$, while for the latter $\theta=0°$. $\underline{k}_V$ is directed tailwards and northwards, with a small component Earthwards along $\underline{B}$ in the direction of the nett field-aligned energy flux. The angle χ between $\underline{k}_V$ and $\underline{B}$ is $\tan^{-1}\left(\lambda_{\parallel}/\lambda_{\perp}\right)$ which is $\sim 89°$, so the wave's phase velocity is essentially the perpendicular wave phase speed, that is, ω/k is $\sim$ 14 km/s.

Having identified the vortex wave mode, we now discuss how the wave coupling occurs.

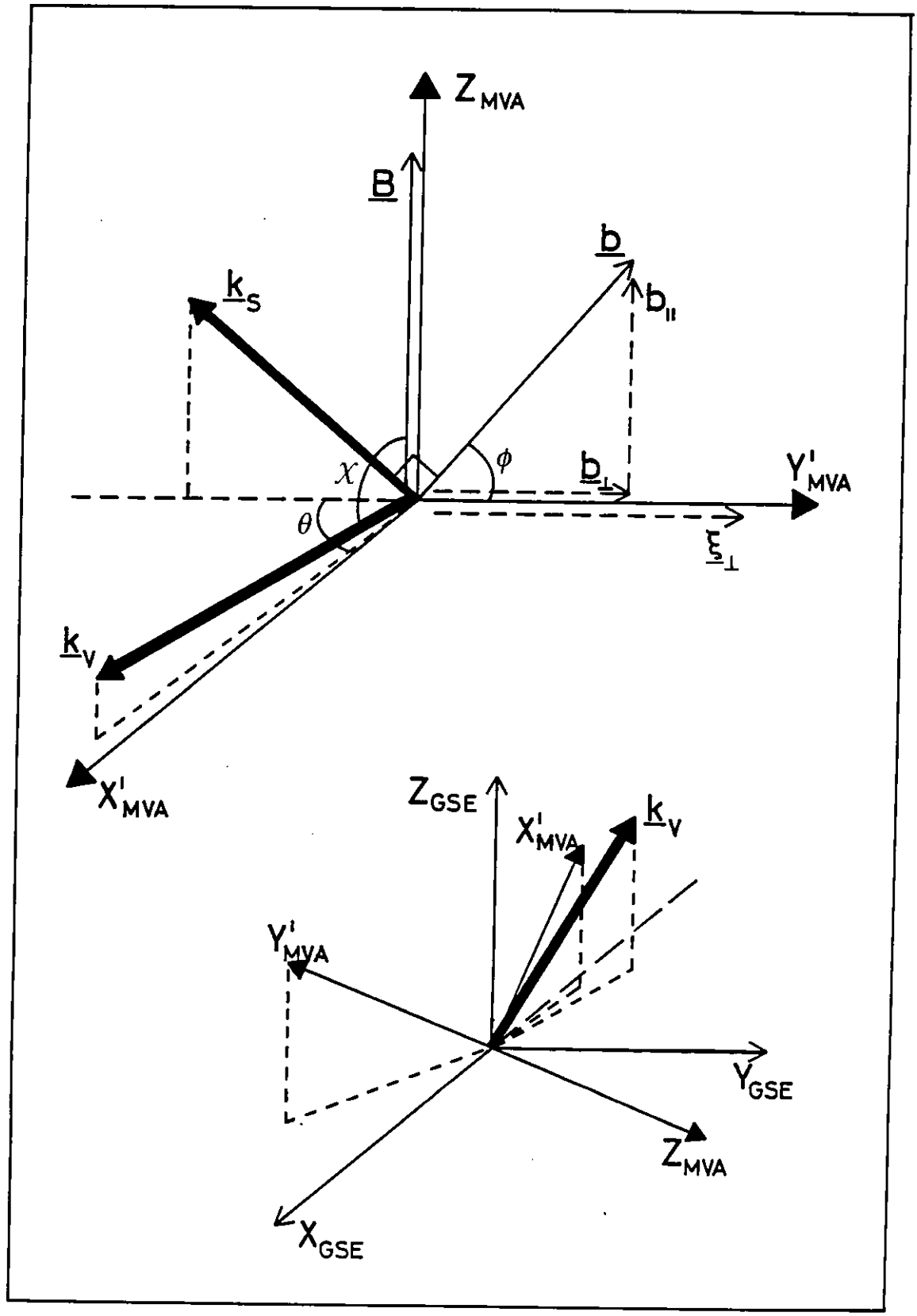

FIGURE 5/1. The upper diagram shows the wave polarisation plot for the 11 December, 1977 vortex. $\underline{k}_v$ is the actual wave vector, while $\underline{k}_s$ denotes the wave vector for a pure slow mode. The lower diagram illustrates the orientation of $\underline{k}_v$ and the MVA coordinate axes in GSE coordinates.

5.3 Coupling of Alfvén and slow modes

Wave coupling can occur in two ways, either through finite Larmor radius effects (see e.g. Coroniti and Kennel, 1970) or from non-uniformity in the background magnetic field. The latter form of coupling has received most attention in cold plasma wave theory, but a full solution to the coupling problem has still to be achieved. With the exception of field line resonance where signals are highly localised and purely transverse, wave coupling is always present in a non-uniform magnetic field such as the Earth's dipole field (Dungey 1954, 1968). Southwood (1977) has shown that in a hot plasma coupling can occur even if the signal is highly localised. Lin and Parks (1978) also suggest that transverse and compressional signals can be coupled by inhomogeneity in a hot plasma.

Finite Larmor radius effects become important when the perpendicular wave wavelength $\lambda_\perp$ approaches the thermal ion Larmor radius (e.g. in the Kinetic Alfvén wave). In such circumstances hydromagnetics no longer adequately describes particle behaviour and it is necessary to use kinetic theory. As the thermal Larmor radius for event 1 was $\lambda_\perp/30$, while for event 2 it was $\lambda_\perp/50$, finite Larmor radius effects were clearly unimportant. Inhomogeneity must have been the cause of wave coupling. The difference in B at the two spacecraft for event 1 (see Fig. 3/3) clearly shows that inhomogeneity was present. Similar ambient field strength differences were recorded for the other events.

To see how non-uniformity in B can cause Alfvén and slow modes to couple, let us consider the ideal case of a

flux tube oscillating in the meridian as a fundamental mode Alfvēn wave. The Alfvēn oscillations possess quasi-standing structure along $\underline{B}$ and east-west localisation across $\underline{B}$; that is, $\underline{\nabla}_\perp x \underline{\xi}_\perp$ is non-zero and the wave phase speed is $\sim (\omega/k)_\perp$. However, for the oscillation to be a pure Alfvēn wave, $b_{||}$ must be zero, in which case plasma pressure, p, and gradients in B, $\underline{\nabla}B$, must be negligible. As the vortices occur in a plasma where β is ~ 1, and since the Earth's dipole field is non-uniform, p and $\underline{\nabla}B$ can clearly not be ignored. Radial oscillations of plasma sheet flux tubes will therefore always give rise to field compression, and the Alfvēn mode oscillations described above will not occur without coupling to a compressional signal. Inhomogeneity in B causes the coupling because it produces a change in flux tube volume, V, in association with the radial motion. In the non-uniform terrestrial dipole field V varies approximately as L^4 - e.g. see Southwood and Kivelson (1975).

As V varies, the plasma within the oscillating tube experiences a periodic compression and rarefaction. Particle energy, W, therefore changes and a perturbation in particle flux results. For an adiabatic process where plasma pressure remains isotropic, these changes are described by

$$WV^{\gamma-1} = \text{constant} .$$

With $V \propto L^4$, the changes in energy, δW, and L-shell, δL, experienced by a particle due to the wave are described by

$$\frac{\delta W}{W} = 4(1-\gamma)\frac{\delta L}{L} \quad . \tag{25}$$

Although this equation indicates that δW is a maximum (minimum) for inward (outward) flux tube displacement, one should note that in addition to the assumption of isotropic δp all along the flux tube, the expression is only strictly correct in the limit when δL does not vary along s. Nevertheless, it is clear that in a hot plasma (where p is not ignorable) particle energy changes do occur when a flux tube oscillates in L-shell. In that case the hot plasma perpendicular momentum equation in a uniform field [equation (5)] shows that for low frequency localised signals the field response will be to minimise the change in total pressure. Since gas and magnetic pressures will oscillate in anti-phase, it is clear that Alfvén and slow mode signals will be coupled. This follows easily from equation (5) by substituting for $b_\perp$ from Faraday's Law and assuming a quasi-standing wave ($\partial/\partial s = k_\parallel$), thus giving

$$\rho\omega^2 \underline{\xi}_\perp = -i\underline{k}_\perp \left(\delta p + \frac{B b_\parallel}{\mu_o}\right) + k_\parallel^2 \left(\frac{B^2}{\mu_o}\right) \underline{\xi}_\perp \ .$$

If the wave pressure perturbations did not tend to cancel, the frequency of signals such as the vortices which are localised far more across $\underline{B}$ than along $\underline{B}$ ($k_\perp >> k_\parallel$), would greatly exceed the frequency of a quasi-standing Alfvén mode ($\omega \sim k_\parallel A$) .

Before proceeding, it is worth pointing out that for event 1, having $\delta W/W \sim 0{\cdot}4$, $\gamma = 5/3$ and $L \sim 10$, equation (25) gives $\delta L \sim 1{\cdot}5 R_E$; a value which compares well with the field line displacement $\sim 1{\cdot}8 R_E$ that we obtained from the plasma data.

While the simple ideas outlined above are useful

for indicating how Alfvén and slow mode waves can couple due to non-uniformity in B, they do not provide a completely satisfactory explanation of the vortex problem. The vortices possess a substantial oscillating field-aligned flow component, a feature one would not expect from oscillations which have δL constant along s since particle acceleration would then be uniform along s and no bounce phase dependence in particle energy would be seen.

Before describing how large parallel flows can be produced, let us reconsider the evidence for acceleration primarily at the equator. Firstly, there is the dispersion in parallel flow. Secondly, the ambient field for events 1 and 2 was flatter with respect to the ecliptic than the model field. This flattening requires the field curvature to be greatest at the equator, and the changes in flux tube volume to be largest there also. A third and strong reason for feeling that the acceleration occurred mainly at the equator, is the fact that the plasma pressure remained isotropic during the wave oscillation (Section 3.2.1). While isotropy can be maintained if there is strong wave turbulence present to cause efficient pitch angle scattering, no turbulence was seen during the vortex events (R.Anderson, private communication). Furthermore, strong turbulence is normally only expected at the outer edge of the plasma sheet. There is, however, an alternative explanation for the local (to ISEE) isotropy.

If acceleration occurred predominately at the equator in a weak B field, field inhomogeneity associated with gradients along $\underline{B}$ could produce the redistribution of energy between parallel and perpendicular degrees of freedom

implied by the isotropic nature of the pressure perturbation. As Cowley (1980) explains in detail, and as we shall indicate, equatorial acceleration in a curved field preferentially enhances a particle's parallel energy. Conservation of the adiabatic invariant, μ, will ensure that the equatorial change in parallel energy is converted into perpendicular energy elsewhere as bounce motion carries the particle away from the equator into regions of stronger B. The pressure will remain isotropic if one is sufficiently far from the equator for the field inhomogeneity along $\underline{B}$, $\partial B/\partial s$, to achieve this energy redistribution. In contrast, for an acceleration source near the field line foot, $\partial B/\partial s$ would produce $p_{||} > p_{\perp}$ pressure anisotropy at the spacecraft.

Clearly there are good reasons for feeling that acceleration did occur at the equator, and in that case the field geometry and motions described below can explain many of the vortex features. Fig. 5/2 illustrates the stretched out field configuration and flux tube motion that we envisage; for simplicity the latter is shown to be radial, though a non-radial component may be present in practice. For further simplicity, the diagram is drawn in 2D with the short perpendicular wavelength direction omitted; the wave is illustrated in 3D later. Since the vortex events that we have detailed occurred pre-dawn, the view is from the duskside of midnight. The solid lines depict the flux tube at four successive times t during the wave cycle of period T, while the dashed lines show the extrema of the flux tube oscillation. Flux tube motion is shown by the dashed arrows,

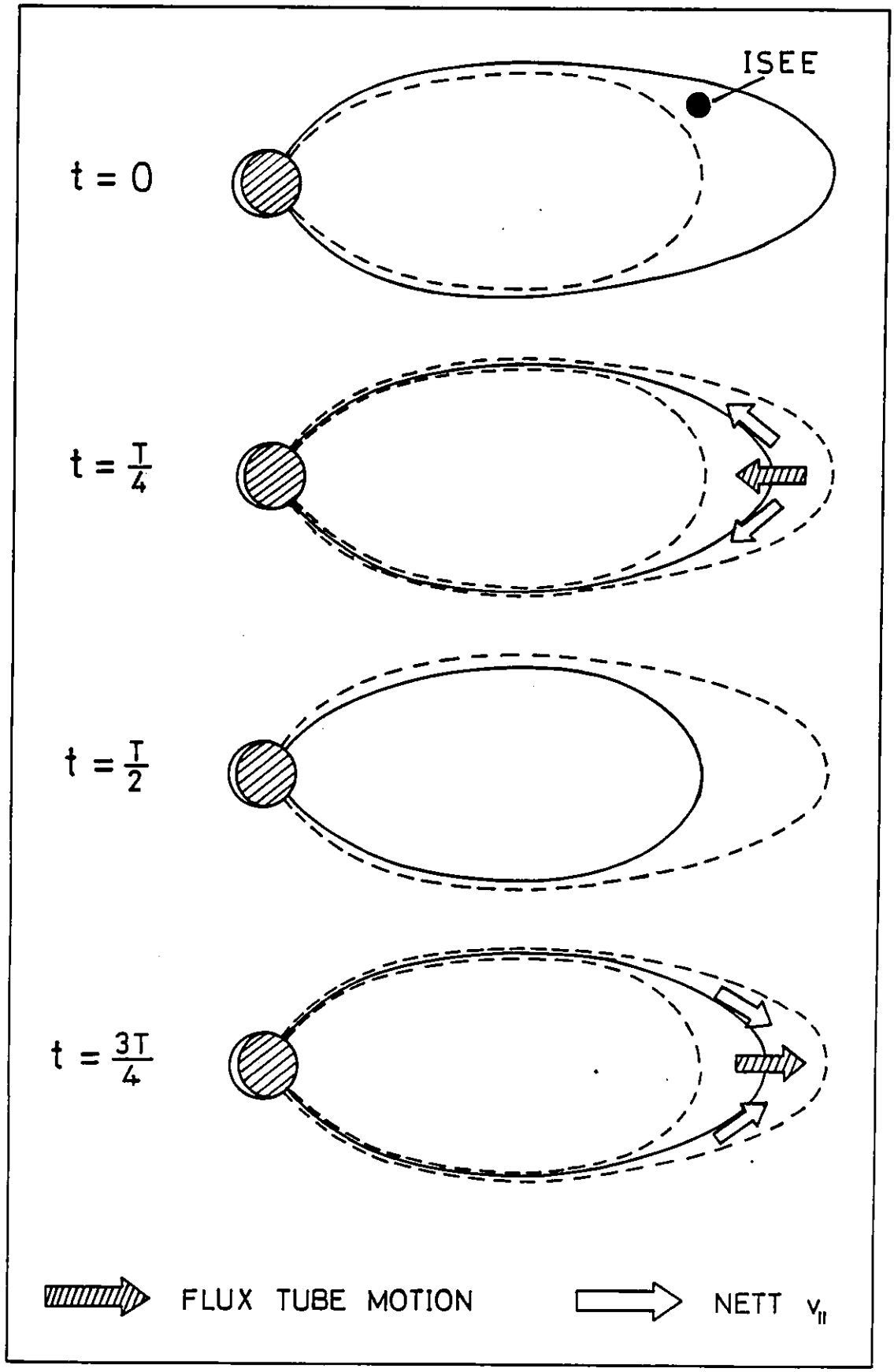

FIGURE 5/2. Two dimensional (meridional) schematics of the vortex flux tube morphology during the wave cycle of period T. The solid line shows the flux tube at time t, while the dashed lines denote the extrema of the flux tube oscillation.

and the directions of nett parallel flow, which we describe below, are indicated by the open arrows. ISEE's approximate position is shown in the t=0 drawing.

The most striking and important feature of Fig. 5/2 is the change in flux tube volume associated with the radial motion. With field lines stretched out by the plasma sheet, field curvature, flux tube displacement, and the volumetric change will all maximise at the equator. The east-west electric field $\underline{E}$ associated with the radial motion, and the particle gradient and curvature magnetic drift, $\underline{v}_d$, will also therefore be largest at the equator. Since the energy of a particle of charge q changes at a rate given by

$$\begin{aligned}\dot{W} &= q\underline{E}\cdot\underline{v}_d + \mu\frac{\partial b_{\parallel}}{\partial t} \\ &= -\frac{2W_{\parallel}\underline{u}_E\cdot\hat{\underline{n}}}{R} - \mu B\left(\underline{\nabla}\cdot\underline{u}_E\right)_{\perp}\end{aligned} \tag{26}$$

(e.g. see Southwood, 1976), where in accordance with previous notation, $\hat{\underline{n}}$ is positive outwards in the meridian, $\dot{W}$ also maximises at the equator. With observations indicating that δW is positive definite for inward flux tube displacement, and with the direction of nett transverse Poynting flux showing that $\underline{k}_{\perp}$ and $\underline{u}_E$ (positive outwards) are antiparallel, the first term must dominate for $\dot{W}$. This term describes energisation due to $\underline{E}.\underline{v}_c$ where $\underline{v}_c$ is the magnetic curvature drift, and will clearly maximise where radial motion is largest and field curvature sharpest.

Although the $\underline{E}.\underline{v}_c$ acceleration term causes δW to increase (decrease) at the equator as the flux tube moves in (out), the spacecraft need not observe a precise anti-

phase variation between δW and $\underline{\xi}_{\perp}$. As we show in a collisionless energy dispersion analysis in Section 5.4, the phase variation that is observed from acceleration at the equator, depends on the spacecraft distance from the equator, on particle energy (or more precisely particle bounce frequency), and on a particle's previous acceleration history. The latter two factors are connected and are important because the plasma does not behave as a fluid; instead, a perturbation imposed at one point on a field line is dispersed as particles of different energies travel along $\underline{B}$ at different speeds. Another outcome of individual particle behaviour is that at locations off the equator, significant particle energy perturbations should occur only at energies where $\omega_b \geq \omega$, for only then can particle bounce motion convey wave-induced energy changes from the equator to the spacecraft. Associated with the change in energy of individual particles is a change in gas pressure; it is this gas pressure oscillation which characterises the slow mode.

Equatorial acceleration provides a natural framework for understanding the origin of the field-aligned flows. A time-varying parallel energisation source at the equator will impose bounce phase dependence in particle energy on a previously uniform particle bounce phase distribution. As a result, two detectors looking in opposite directions along $\underline{B}$ will observe particle distributions shifted in energy by different amounts. In other words they detect a nett field-aligned flux of particles or a field-aligned flow.

The rate of change of particle parallel energy at

one point is

$$\dot{W}_{\parallel} = \dot{W} - \mu\left(\frac{dB}{dt} + \frac{db_{\parallel}}{dt}\right)$$

$$= -\frac{2W_{\parallel}\underline{u}_E \cdot \hat{\underline{n}}}{R} - \mu\left(v_{\parallel}\frac{\partial B}{\partial s} + v_{\parallel}\frac{\partial b_{\parallel}}{\partial s} + \underline{u}_E \cdot \underline{\nabla} b_{\parallel}\right) .$$

The first term describes the parallel energisation due to $\underline{E}.\underline{v}_c$, while the second and third terms are the mirror force contributions from the background field and the wave respectively. Since u_E is an order of magnitude smaller than $v_{\parallel}$, the last term can be neglected when compared with the mirror terms. To explain the presence of the large parallel flows the latter in turn must be small in comparison with the $\underline{E}.\underline{v}_c$ term because, unlike $\underline{E}.\underline{v}_c$ acceleration which can maximise at the equator, the mirror acceleration effects are distributed all along s. For there to be bounce phase dependence in particle energy the acceleration must be fairly localised in space. That $\underline{E}.\underline{v}_c$ acceleration was shown to dominate $\dot{W}$ is another reason for its domination of $\dot{W}_{\parallel}$; a fact substantiating the point made earlier that equatorial acceleration in a curved field preferentially enhances a particle's parallel energy.

The magnitude of changes in parallel energy, $\delta W_{\parallel}$, and in parallel velocity, $\delta v_{\parallel}$, arising from equatorial $\underline{E}.\underline{v}_c$ acceleration are shown below. The integration is taken over the time interval during which a particle passing through the equator experiences acceleration.

$$\delta W_{\parallel} = q\int \underline{E}.\underline{v}_c dt = \int \frac{m v_{\parallel}^2 E}{BR}\, dt = \frac{m v_{\parallel} E_e \Delta s}{B_e R_e}$$

$$\text{and } \delta v_{\parallel} = \frac{E_e \Delta s}{B_e R_e} .$$

The subscript e refers to the equator, m is particle mass and Δs represents the distance along $\underline{B}$ for which the acceleration takes place. $\delta W_{||}$ and $\delta v_{||}$ are clearly enhanced by large E and sharp field curvature.

One might expect that $v_{||}$ and δW are related in phase and indeed this is so, as our modelling of energy dispersion will show. However, for the moment, to provide a feeling for the phase of $v_{||}$ one might expect to see, one should note that as particle energy increases at the equator (at t=T/4 in Fig. 5/2), bounce motion will ensure there is a nett flux of particles away from the equator in both directions. Conversely at t=3T/4, when equatorial deceleration is occurring, nett parallel motion will occur towards the equator. A useful though simplified way of picturing the field-aligned flows is in terms of a squeezing and sucking of particles as the flux tube moves radially in and out.

Before concluding this section let us comment further on the $b_{||}$ signal. Equation (6) indicates that $b_{||}$ should oscillate in antiphase with $\underline{v}_\perp$ (or $\underline{u}_E$) because

$$b_{||}=-(i\underline{k}_\perp \cdot \underline{\xi}_\perp)B=(\underline{k}_\perp \cdot \underline{u}_E)B/\omega,$$

and $\underline{k}_\perp$ and $\underline{u}_E$ are antiparallel as shown by the direction of nett transverse Poynting flux. However, this phase dependence is inconsistent with observations (see Figs. 3/2 and 4/2), indicating that other effects neglected in our theoretical treatment of MHD waves also contributed to $b_{||}$. The $-\underline{\xi}_\perp \cdot \underline{\nabla}B$ term (Southwood, 1973) due to flux tube displacement along a gradient in B could have been important in this regard. Indeed it is worth noting

that the observed phase of $b_{||}$ for events 1 and 2, lay midway between the phases of $-(\underline{\nabla}_{\perp}.\underline{\xi}_{\perp})$ and $-\underline{\xi}_{\perp}.\underline{\nabla}B$, suggesting that the two terms contributed equally to $b_{||}$. However, this need not be the case, because as we show in the next section, the past acceleration history of a particle will modify the observed phase of δW and consequently the phase of $b_{||}$ also. With this complication it is physically easier just to picture the $b_{||}$ signal as the field's response towards minimising the change in total pressure.

To summarise, an east-west propagating Alfvén wave that gives rise to radial flux tube displacements which maximise in amplitude at the equator, will couple to a slow mode wave and produce significant field-aligned flows. The coupling is due to the change in flux tube volume associated with the motion, while the volume change is due to the background field being non-uniform. With a maximum volume change at the equator, particle acceleration, preferentially in parallel energy, will also be greatest at the equator. This will give rise to bounce phase dependence in particle energy and to parallel flows. Although collisionless damping rates have not been estimated, wave decay should be rapid on removal of the equatorial 'pump'.

Before discussing the wave source, we first quantify our arguments for equatorial acceleration by showing that such acceleration can produce the observed energy dispersion, and the observed phase difference between $\delta v_{||}$ and δW. In our modelling we stress the importance of individual particle rather than fluid behaviour, and

therefore the need to consider a particle's past acceleration history.

5.4 Energy Dispersion

5.4.1 Introduction

Although the fluid description of hot plasma waves in Section 5.1 was sufficiently rigorous to allow the vortex wave mode to be identified, a fluid approach is unsuitable for investigating the detailed dynamics of the wave. This is because hydromagnetics is only an approximate theory; it is good for describing particle motion perpendicular to $\underline{B}$ but is inadequate for detailing particle motion along $\underline{B}$. Particles travelling parallel to $\underline{B}$ do not behave as fluid elements - rather they 'free stream', moving at speeds proportional to their energies. As 'free streaming' particles can move substantial distances in a short time, their behaviour at a particular point, say the spacecraft, can depend not on the local wavefield which the spacecraft sees, but on the wavefield some distance away. Hydromagnetic theory does not include the effect of 'distant influences'.

To model the vortex parallel flow and δp one should therefore use a single particle interpretation. By integrating backwards in time along a particle's past trajectory, the local behaviour of a particle can be predicted. This is the approach that we apply here in modelling the vortex energy dispersion and the related matter of the phase difference between $v_{||}$ and δp.

The basis of our theoretical model is described below. By taking the acceleration to be localised at

the equator, we show that important vortex features can be reproduced. The calculation of changes in parallel velocity, $\delta v_{||}$, and particle energy are based on moments of the distribution function. For simplicity (to eliminate the $v_{\perp}$ terms in the moment integrals) let us consider 0° pitch angle particles. In that case

$$\delta v_{||} = \int_{0}^{\infty} \delta f_{+} v_{||} dv_{||} + \int_{-\infty}^{0} \delta f_{-} v_{||} dv_{||} = \int_{0}^{\infty} (\delta f_{+} - \delta f_{-}) v_{||} dv_{||} \tag{27}$$

$$\text{and} \quad \delta W = \delta W_{||} = \frac{1}{2} \int_{0}^{\infty} \delta f_{+} m v_{||}^{2} dv_{||} + \frac{1}{2} \int_{-\infty}^{0} \delta f_{-} m v_{||}^{2} dv_{||} = \frac{1}{2} \int_{0}^{\infty} (\delta f_{+} + \delta f_{-}) m v_{||}^{2} dv_{||} \ , \tag{28}$$

where $\delta f_{+} = -\delta W_{+} \frac{\partial f}{\partial W}$ and $\delta f_{-} = -\delta W_{-} \frac{\partial f}{\partial W}$.

The subscripts + and - refer to changes in distribution function, δf, or particle energy, δW, that are moving parallel (+) or antiparallel (-) to $\underline{B}$ (see Fig. 5/3(a)). It is clear that while $\delta v_{||}$ depends on the <u>difference</u> in particle distribution functions travelling in opposite directions along $\underline{B}$, δW depends on the <u>sum</u> of δf_{+} and δf_{-}. This change in sign is important for it allows a phase difference to occur between $\delta v_{||}$ and δW. From equation (28) it follows that an identical phase difference should also exist between $\delta v_{||}$ and δp because δp is in phase with δW.

We shall consider two types of equatorial signal variation, though the model can be used to investigate other forms of signal. The first signal we apply has a Gaussian variation in acceleration amplitude and we follow this by studying the effect of damping on a sudden (Heaviside) impulse signal. The former signal has the

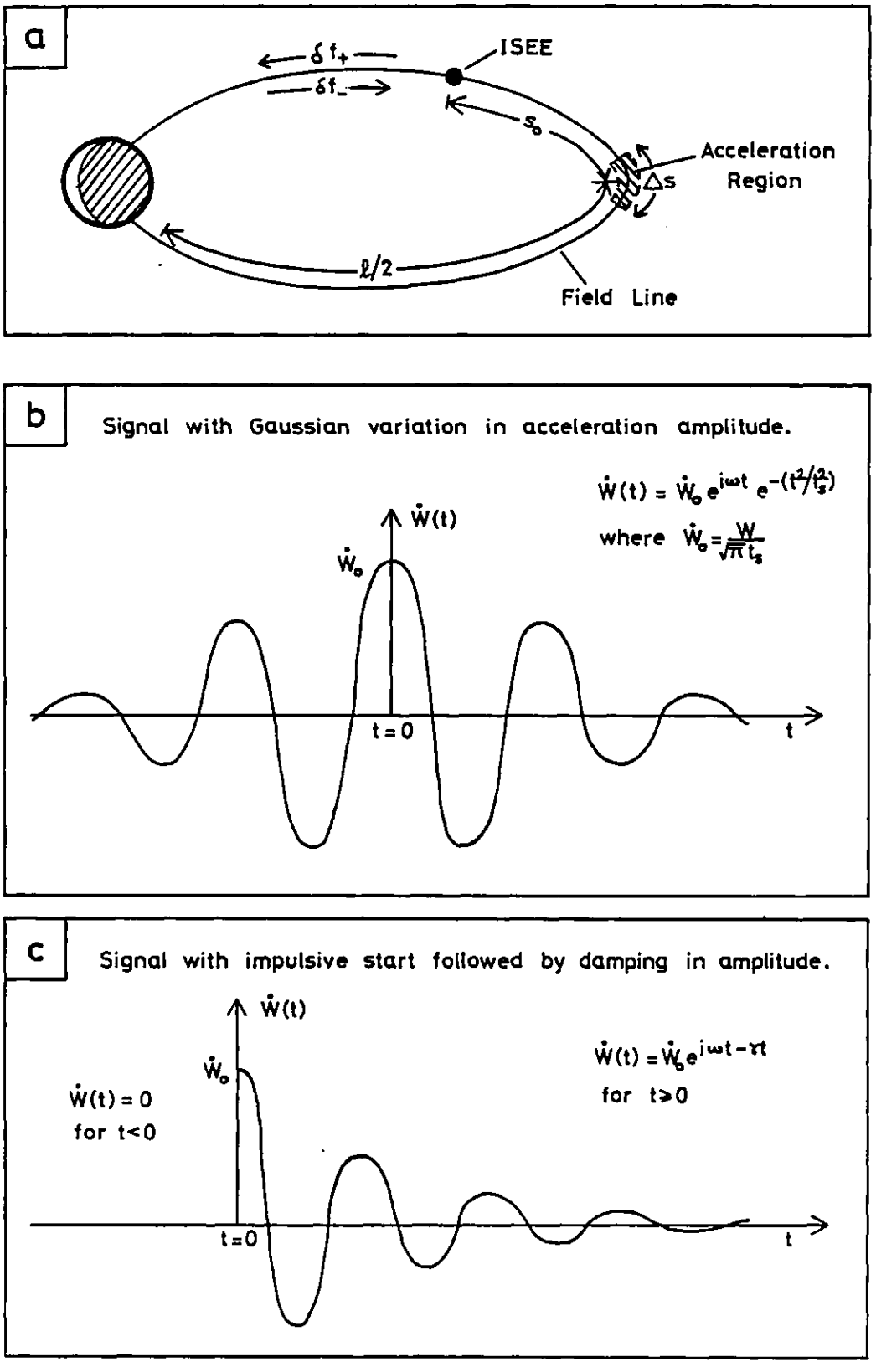

Figure 5/3. Definition of parameters (a) and signals (b and c) used in the energy dispersion modelling.

advantage of matching well the observed variation in wave amplitude. The second signal is investigated because in another instance of parallel motion (Quinn and Southwood, 1982) acceleration onset was impulsive.

5.4.2 Gaussian signal

For acceleration which varies sinusoidally with time and has a Gaussian variation in amplitude that peaks at time t=0, we may write from equation (26)

$$\dot{W}(t) = -\frac{2W_{||}\underline{u}_E \cdot \hat{\underline{n}}}{R} - \mu B\left(\underline{\nabla} \cdot \underline{u}_E\right)_{\perp}$$

$$= \dot{W}_o e^{i\omega t} e^{-(t^2/t_s^2)} \quad , \tag{29}$$

where $\dot{W}_o = \frac{1}{\sqrt{2\pi}\sigma}$, $t_s = \sqrt{2}\sigma$

and σ is the standard deviation of $\dot{W}(t)$. This signal is illustrated in Fig. 5/3(b). With acceleration localised along a small segment Δs of s about the equator, where s is a coordinate measured parallel to $\underline{B}$ and s=0 corresponds to the equator, equation (29) becomes

$$\dot{W}(t) = \dot{W}_o \Delta s \, \delta(s) e^{i\omega t} e^{-(t^2/t_s^2)}$$

where $\delta(\ )$ is the Dirac delta function.

The change in particle energy observed at time t_o, $\delta W(t_o)$, is calculated by integrating backwards in time along the particle's past orbit. This integration is to include the effect on local particle behaviour of previous encounters with the equator. Thus

$$\delta W(t_o) = \dot{W}_o \Delta s \int_{\substack{-\infty \\ \text{along} \\ \text{orbit}}}^{t_o} \delta(s) e^{i\omega t} e^{-(t^2/t_s^2)} \, dt \quad . \tag{30}$$

Now particles of speed v at position s_o at time t_o and moving towards the Earth, were previously at the equator at times, t, given by

$$t=t_o-\frac{s_o}{v}-\frac{n\ell}{v} \tag{31}$$

where n is an integer and ℓ is half the bounce path length. s_o and ℓ are also defined in Fig. 5/3(a). While the particles described by equation (31) contribute to δf_+, particles travelling in the opposite direction (away from the Earth) at t_o and s_o give rise to δf_-. These latter particles were at the equator at times

$$t=t_o+\frac{s_o}{v}-\frac{\ell}{v}-\frac{n\ell}{v}$$

$$=t_o-\frac{s_o}{v}-\frac{n\ell}{v}+\frac{(2s_o-\ell)}{v} \quad . \tag{32}$$

From equation (28), the nett δW depends on the sum of δf_+ and δf_-. Equations (31) and (32) can be substituted into equation (30) to give

$$\delta W(t_o)=\sum_{n=o}^{\infty}\frac{\dot{W}_o\Delta s}{v}\left[\int_{-\infty\,\text{orbit}}^{t_o}\delta\left(t-t_o+\frac{s_o}{v}+\frac{n\ell}{v}\right)e^{i\omega t}e^{-(t^2/t_s^2)}\,dt\right.$$

$$\left.+\int_{-\infty\,\text{orbit}}^{t_o}\delta\left(t-t_o+\frac{s_o}{v}+\frac{n\ell}{v}+\frac{(\ell-2s_o)}{v}\right)e^{i\omega t}e^{-(t^2/t_s^2)}\,dt\right]$$

where a summation has been taken over all previous encounters with the equator.

$$\therefore\ \delta W(t_o)=\sum_{n=o}^{\infty}\frac{\dot{W}_o\Delta s}{v}\left[e^{i\omega(t_o-s_o/v-n\ell/v)}e^{-(t_o-s_o/v-n\ell/v)^2/t_s^2}\right.$$

$$+e^{i\omega(t_o - s_o/v - n\ell/v - (\ell-2s_o)/v)} e^{-(t_o - s_o/v - n\ell/v - (\ell-2s_o)/v)^2/t_s^2}$$

$$= \sum_{n=o}^{\infty} \frac{\dot{W}_o \Delta s}{v} \left[A + B \right] \quad , \text{ say.} \tag{33}$$

It is now straightforward to obtain a corresponding expression for $\delta v_{||}$ at t_o and s_o. As equation (27) shows that $\delta v_{||}$ depends on the <u>difference</u> between δf_+ and δf_-, and since the peak equatorial parallel acceleration, $\dot{v}_{o_{||}}$, is related to $\dot{W}_o$ by

$$\dot{v}_{o_{||}} = \frac{\dot{W}_{o||}}{m v_{||}} \simeq \frac{\dot{W}_o}{m v_{||}} \quad ,$$

it follows that

$$\delta v_{||}(t_o) = \sum_{n=o}^{\infty} \frac{\dot{W}_o \Delta s}{m v \; v_{||}} \left[A - B \right] \cdot \tag{34}$$

For a given s_o and t_o, equations (33) and (34) allow the phases and relative magnitudes of δW and $\delta v_{||}$ to be calculated in terms of particle energy. A few modelling results are presented in Fig. 5/4 for a wave frequency corresponding to that of the 11th. December, 1977 vortex event.

Fig. 5/4(a) shows plots of dispersion in parallel flow calculated (using equation (34)) for different values of ℓ (x10^{4}km) at fixed s_o/ℓ, t_o and t_s. The angle $\psi_{||}$ is the phase angle between ωt_o and $\delta v_{||}$, and is proportional to the phase delay between a maxima, say, in the equatorial acceleration, and the subsequent maxima in $\delta v_{||}$ at the spacecraft. For a given ℓ, $\delta v_{||}$ clearly maximises first at high energy, while at large ℓ the phase delay for low velocity particles can exceed the wave period. The

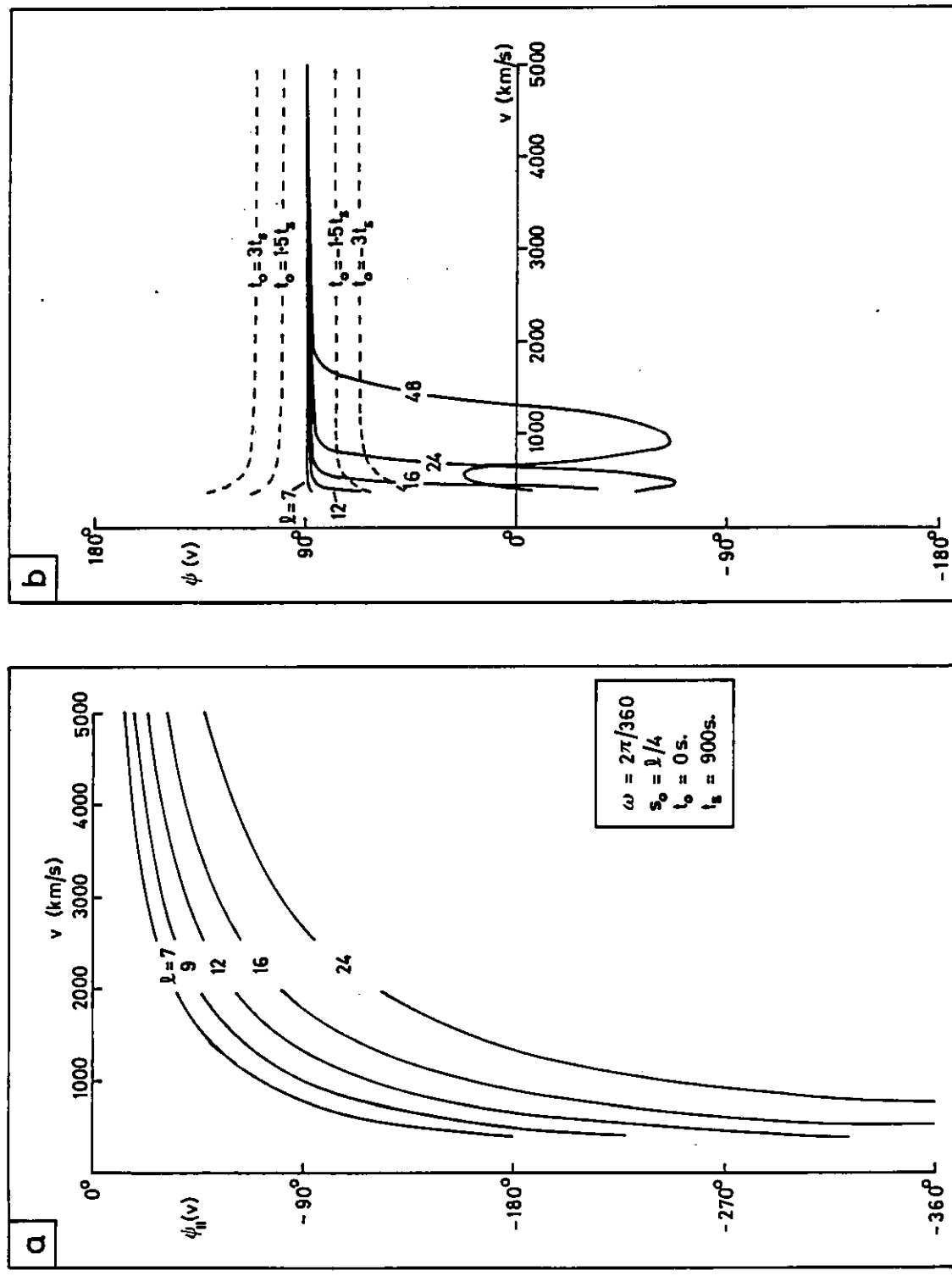

FIGURE 5/4. Phase angles resulting from an equatorial acceleration signal of period 360s having a Gaussian variation in amplitude (Fig. 5/3 (b)). With the exception of the dashed line plots in (b), t_o, s_o/ℓ and t_s are constant at the values shown boxed in (a). (a) illustrates the phase angle in parallel flow, ψ_{II}, as a function of velocity for different bounce amplitudes $\ell(\times 10^4 km)$. The solid curves in(b) show the phase, ψ, between v_{II} and δW as a function of particle speed and ℓ. The dashed curves indicate the effect of varying t_o for $\ell=9$. ψ is positive if v_{II} leads δW in phase.

observed energy dispersion in Fig. 3/15 matches best the dispersion curve corresponding to $\ell \sim 9$ in Fig. 5/4(a). This implies that $\omega_{b,th}$ was $\sim 2\omega$; a bounce frequency in reasonable agreement with that calculated using the thermal velocity and estimated field line L-value (see Table 3/2). Although not shown, the dependence of $\psi_{||}$ on t_o, t_s and s_o/ℓ is small. For example, at $\ell=9\times10^4$km, $s_o=\ell/4$, $t_s=900$s and v=1000km/s, $\psi_{||}$ varies less than 8° over a range in t_o values between 2500s and -2500s.

The phase angle between $\delta v_{||}$ and δW (or δp), defined as ψ, is plotted in Fig. 5/4(b) as a function of v and ℓ. $\delta v_{||}$ leads δW in phase if ψ is positive. The curves show that ψ is independent of energy provided $\omega_b \geq \omega$. However, unlike the case of $\psi_{||}$, ψ does depend on t_o, and increases during the event as the dashed curves (plotted for $\ell=9\times10^4$km) show. Comparison with Fig. 3/2 shows that these model results are in fair agreement with observations. Differences exist, in that the observed phase angle is $\sim 60°$ (rather than 90°), and also in that observations indicate a decrease rather than an increase in ψ during the event.

5.4.3 Impulse signal and damping

A signal consisting of an acceleration impulse at t=0 with subsequent damping in amplitude is illustrated in Fig. 5/3(c). Redefining the wave frequency used previously with $\omega=\omega+i\gamma$, where γ (negative for wave growth) is the damping rate, we can describe the signal by

$$\dot{W}(t)=\dot{W}_o e^{i\omega t-\gamma t} \quad , \quad t\geq 0,$$

where $\dot{W}_o$ is the initial amplitude.

Taking the acceleration to be localised at the equator and applying the same theoretical procedures described for the Gaussian signal analysis, one obtains

$$\delta W(t_o) = \sum_{n=o}^{n=N} \frac{\dot{W}_o \Delta s}{v} \left[\int_o^{t_o} \delta\left(t - t_o + \frac{s_o}{v} + \frac{n\ell}{v}\right) e^{i\omega t - \gamma t} dt \right.$$

$$\left. + \int_o^{t_o} \delta\left(t - t_o + \frac{s_o}{v} + \frac{n\ell}{v} + \frac{(\ell - 2s_o)}{v}\right) e^{i\omega t - \gamma t} dt \right]$$

$$= \sum_{n=o}^{n=N} \frac{\dot{W}_o \Delta s}{v} e^{i\omega t_o} e^{-i\omega s_o / v} e^{-i\omega n\ell / v} e^{-\gamma t_o} e^{\gamma s_o / v} e^{\gamma n\ell / v}$$

$$\left(1 + e^{-i\omega(\ell - 2s_o)/v} e^{\gamma(\ell - 2s_o)/v}\right) . \qquad (35)$$

The integration backwards in time is truncated at t=0 because the particles do not experience acceleration prior to signal onset. N is the number of equatorial encounters between t=0 and t_o, and is assumed to be the same for particles travelling in opposite directions at s_o. Applying the geometric series formula

$$\sum_{n=o}^{n=N} x^n = 1 + x + x^2 + \ldots\ldots = \frac{1 - x^N}{1 - x} \quad , \quad x \neq 1$$

to equation (35), and noting that $N = t_o v/\ell$, it follows that

$$\delta W(t_o) = \frac{\dot{W}_o \Delta s}{v} e^{i\omega(t_o - s_o/v)} e^{-\gamma(t_o - s_o/v)} \left[\frac{1 - e^{\gamma t_o} e^{-i\omega t_o}}{1 - e^{\gamma\ell/v} e^{-i\omega\ell/v}} \right]$$

$$\left(1+e^{-i\omega(\ell-2s_o)/v_e\gamma(\ell-2s_o)/v}\right)$$

$$= \frac{\dot{W}_o \Delta s}{v} C(1+D)$$

where $D=e^{-i\omega(\ell-2s_o)/v_e\gamma(\ell-2s_o)/v}$.

The corresponding expression for $\delta v_{||}$ at t_o and s_o is

$$\delta v_{||}(t_o)=\frac{\dot{W}_o \Delta s}{m v_{||} v} C(1-D) \quad . \tag{36}$$

The phase angle, ψ, between $\delta v_{||}$ and δW is governed by the ratio

$$\frac{1 - D}{1 + D}$$

and is independent of t_o. A few algebraic steps give the result that

$$\psi=\tan^{-1}\left(\frac{-\sin\left(\frac{\omega}{V}(\ell-2s_o)\right)}{\sinh\left(\frac{\gamma}{V}(\ell-2s_o)\right)}\right)$$

which shows that if there is no damping ($\gamma=0$), ψ is 90° independent of energy and s_o. This result arises from the remarkable fact, which is proved in Appendix E, that no energy dispersion occurs when γ is zero. This unexpected feature is also evident in Fig. 5/5(b) where values of the phase angle $\psi_{||}$(between ωt_o and $\delta v_{||}$) are shown computed as a function of v and γ. For these calculations ω was again taken to be $2\pi/360$, and values of 9×10^4km and $\ell/4$ were used for ℓ and s_o respectively. The dispersion in parallel flow is clearly too small to match observations. Furthermore, wave growth rather than damping is required

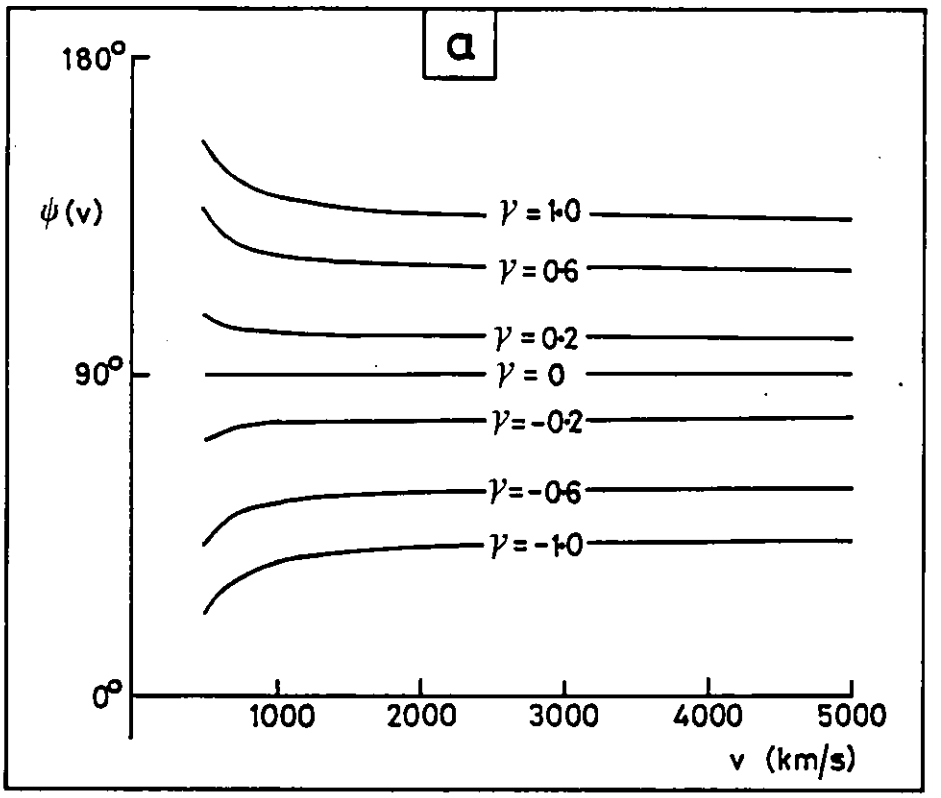

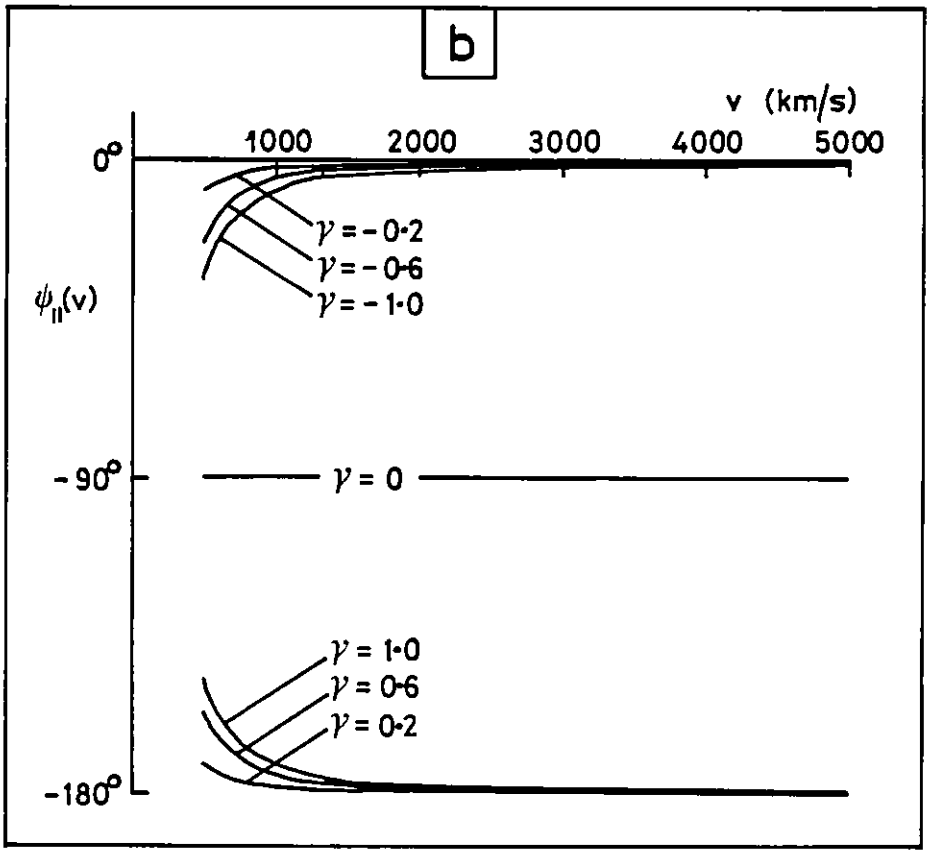

FIGURE 5/5. Phase angles resulting from a Heaviside impulse acceleration signal at the equator with subsequent damping ($\gamma>0$) or growth ($\gamma<0$) in wave amplitude. Computations used equations (36) and (37) with $\omega=2\pi/360$ radians/s, $\ell=9\times10^4$km, $s_0=\ell/4$ and $t_0=360$s ((b) only). (a) illustrates the variation in phase angle, ψ, between v_{II} and δW as a function of γ and v, while (b) shows a similar display for the phase angle, ψ_{II}, in parallel flow.

for high energies to lead in phase. Fig. 5/5(a) shows that wave growth is also required for the phase angle ψ to agree with observations ($\psi<90°$). It is also worth noting that ψ is more sensitive than $\psi_{||}$ to changes in γ.

5.4.4 Discussion

The modelling results obtained with the impulse acceleration signal followed by damping are clearly less satisfactory than those obtained using the Gaussian signal. The latter reproduces well the observed energy dispersion when $\omega_{b,th} \sim 2\omega$; a bounce frequency which would allow wave-induced energy changes to propagate along $\underline{B}$, and which is also consistent with the value calculated from the thermal velocity and estimated field line L- value (Table 3/2). Although the Gaussian slightly overestimates the phase angle ψ, this could be overcome, as Fig. 5/5(a) shows, by including a wave growth term in equation (29). In short, the agreement with observations obtained using this signal is sufficiently good to provide strong support for the idea that equatorial acceleration can explain the vortex features.

An important further test of our modelling results would be to investigate the phases of δW and $\delta v_{||}$ observed at energies below the thermal energy. As Figs. 5/4 and 5/5 show, the phase changes should become increasingly larger at lower energies where ω_b approaches ω.

5.5 Wave generation

The vortex events that we have studied have been interpreted as the coupling of Alfvén and slow mode waves resulting from radial flux tube oscillations which maximised in amplitude at the equator. As event occurrence is independent of K_p (see Tables 3/2 and 4/2) - a fact which is true for vortices in general (Hones et al., 1981) - the field line motions are not substorm related. In that case, and since the direction of nett wave energy flux is inwards in the meridian and Earthwards along $\underline{B}$, there are good reasons for feeling that the radial oscillations were imposed by surface waves at the outer boundary.

The Kelvin-Helmholtz (KH) or 'wind-over-water' instability, due to the velocity shear between solar wind or low latitude boundary layer plasma streaming along the flanks of the magnetosphere and the plasma sheet proper, provides the most attractive way of generating surface waves (see Southwood (1979) for a recent review). KH instability theory makes two simple predictions. Firstly, energy input should occur preferentially at the equator, where the magnetic field which is inhibiting to wave growth is weakest and plasma pressure largest. Secondly, wave motion should be tailwards at a speed comparable to the exterior, or 'wind', velocity v_{sw}, that is at $\sim$ 100-200km/s.

On the first point our observations and model are consistent with the instability prediction. However, the wave amplitude for events 1 and 2 of $\sim 1R_E$ is somewhat large compared with surface wave amplitudes reported previously, which are typically a few $x10^3$km (e.g. Southwood (1979), Lepping and Burlaga (1979)). On the second prediction there is disagreement. For example, in event 1,

while the vortex wave propagates tailwards, its phase speed is only 14km/s (or ∿ 20-25km/s when projected to the magnetopause), a value clearly much less than v_{sw}. The phase speeds of the other vortex events are also well below v_{sw}. In this context it is interesting to note the observations reported by Fahnenstiel (1981), who, using ISEE MEPE data to remote sense the magnetopause for wave motion, obtained (from an initial two event study) east-west wave phase speeds of order 3km/s.

In seeking an explanation for these low values one should note that it is the group velocity and not the phase velocity which propagates tailwards at v_{sw}. By analogy, therefore, with waves on the ocean where group and phase velocities do not match, the vortex events would show consistency with the KH instability if their group velocity was significantly greater than their phase velocity. However, this explanation is unsatisfactory because the events had no measurable energy flux in the propagation direction, implying that the group velocity in this direction was small. The question therefore remains open as to how to reconcile the low phase and group speeds in the direction of propagation with wave generation by the KH instability. Nevertheless, in view of the other vortex features which suggest that the waves were established at the outer boundary, this instability remains the most feasible source mechanism.

To conclude, we show in Fig. 5/6 a 3D schematic as to how one might visualise surface waves, either at the magnetopause or at the inner edge of the low latitude boundary layer, causing meridional oscillations on equator-

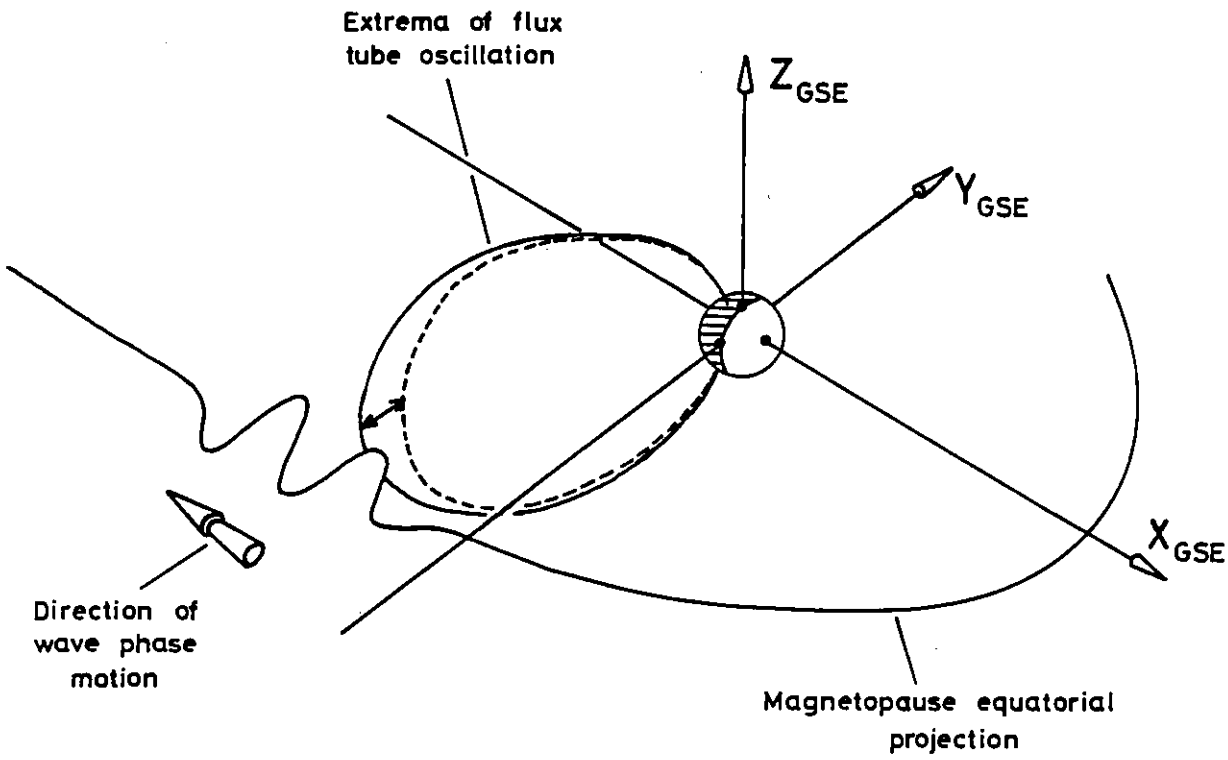

FIGURE 5/6. Vortex wave schematic in 3D, illustrating the possible establishment, by surface waves at the magnetopause, of the flux tube configurations and motions shown in Fig. 5/2.

ially extended tail flux tubes, thereby generating the vortex wave.

CHAPTER 6

CONCLUSIONS AND SUGGESTIONS FOR FURTHER WORK

Despite its title, this thesis is primarily concerned with interpreting through data analysis and theory, a curious and unexpected ISEE spacecraft discovery: the magnetotail plasma vortices. It should be emphasized at the outset that the conclusions described below refer to the vortex events studied here; it would be unwise, without further study, to generalise the results to all vortices. Nevertheless, the thesis clearly puts into question the original vortex interpretation of Hones et al. (1978,1981) which envisages a spatially rotating plasma flow feature with $\nabla \times \underline{v} \neq 0$; the vortices are certainly far more complex than these initial studies implied.

The vortices are in fact associated with hydromagnetic waves, and apparent vortical motion is seen in the ecliptic plane because the flow parallel to $\underline{B}$ is in quadrature to the flow perpendicular to $\underline{B}$. Specifically, the vortex wave is a coupling between the Alfvén mode and the MHD slow mode; the latter is a wave mode which has often been neglected previously in collisionless plasma theory because it should be strongly Landau damped. An explanation based on changes in flux tube volume, has been suggested as to how this wave coupling can occur in a hot inhomogenous plasma. The important requirement is for the volumetric change to

maximise at the equator, so ensuring that plasma acceleration, mainly in parallel energy, is also largest at the equator. Equatorial acceleration can explain the slow mode wave features of field-aligned flow and perturbations in gas and field pressures. Since the changes in flux tube volume which give rise to the plasma acceleration occur because the Earth's dipole field is non-uniform, one can interpret the wave coupling as due to non-uniformity in B. This explanation has been quantified with reasonable success by modelling the important vortex features using an acceleration source localised at the equator. A feature of the modelling approach is the need to view the plasma in terms of individual particles rather than as a fluid.

Further to clarifying the nature of the vortices, as described above, the thesis also contributes to existing knowledge on the properties and theory of hot plasma hydromagnetic waves. In particular the evidence presented for the existence of the slow mode, is to our knowledge the strongest to date, while the discussion of wave coupling (between Alfvēn and slow modes) is novel and should provide a sound basis for mathematical development.

Other findings worth mentioning include those associated with the interpretation of the energetic particle measurements. The large spin modulation in these data originally caused much puzzlement, and was interpreted by Fritz (1981) as evidence for an ambient density gradient oscillating back and forth

across the spacecraft. While showing this theory to be incorrect, it was argued that the spin modulations were wave-induced, reflecting the wave's small perpendicular scalelength and large amplitude. This interpretation has an important experimental consequence in that the energetic particle flux asymmetries can be used to remote sense the wave, thereby allowing the wave's perpendicular wavelength and direction of propagation to be determined; wave parameters which are otherwise difficult to measure accurately. A theoretical implication of the wave induced pressure gradients is that diamagnetic ($\nabla p \times B$) drift can be more important than $E \times B$ drift in producing spin cycle flux asymmetry in a hot plasma at high energy.

A further result mentioned here is also theoretical in nature and relates to the unexpected discovery that in a collisionless plasma an equatorial periodic acceleration signal of constant amplitude can give rise to parallel flows with no energy dispersion. Dispersion disappears when one integrates backwards in time to incorporate the effect on local behaviour of a particle's past acceleration history.

The last noteworthy finding reported here is the experimental identification of magnetic field pulsations on the ground in association with a vortex seen in space; a result which gives independent support to the hydromagnetic description of the vortices.

To discuss briefly suggestions for further work is far from easy; not because all the problems have been solved - rather the converse! The obvious limitation

of the present work is the number of events studied; although the 11th December event was not unique, vortices in the vicinity of the neutral sheet and on the duskside have yet to receive detailed study. As 'detailed study' in this context would involve synthesizing magnetometer, 3D plasma, electric field and energetic particle data - a difficult task - simpler but effective studies can be undertaken with just magnetic field and plasma measurements.

A top priority should be the investigation as to whether all vortex events possess a parallel flow component. If, as would seem likely, this is so, the equatorial acceleration model proposed here can explain the change in sense of flow rotation between dawnside and duskside events reported by Hones et al. (1981); namely clockwise (anticlockwise) on the dawnside (duskside) when viewed from above the ecliptic. For example, if at duskside locations symmetrically opposite to the dawnside positions where the vortices studied here were observed, $v_{||}$ also led $v_{\perp}$ in quadrature, anticlockwise flow rotation would endure because of the different directions of the background field and meridian on the duskside compared with the dawnside. To test this and other theories requires knowledge of the variation in phase between $v_{||}$ and $v_{\perp}$ as a function of local time and latitude.

Another useful study would be to establish whether perturbations in temperature and pressure are generally present in the vortex plasma data, and if so, how they relate in phase to $\delta v_{||}$. Other features requiring investigation include the degree of isotropy shown by δp, and the energy dispersion in $\delta v_{||}$ and δp. Only by

studying these key vortex features for many events, will the generality of any vortex model be determined.

The magnetometer data should be used to establish whether the field tilting associated with the vortices is consistent with the stretched out field configuration at the equator that one would expect of an equatorial source. Field data from both spacecraft should be compared to gain information on wave scalesize, speed and direction of propagation. On the duskside the latter wave property would be a useful further test for how applicable the Kelvin-Kelmholtz instability mechanism is to vortex generation. Due to the large scalesize of the vortices, large spacecraft separations are preferable, so emphasis should be given to studying the vortex events during the Spring of 1979 when separations maximised at about 10,000km (see Fig.1/2). As data from a suitably deployed ground magnetometer network can, amongst other things, furnish useful information on wave scalesize and direction of propagation, ground studies should be actively pursued.

The main priority of future theoretical work should be to put into mathematical form the physical ideas on Alfvén/slow mode wave coupling outlined here. This mathematical description should include treatments of wave damping and of pressure balance. Other studies which could be usefully undertaken are a more detailed modelling of the equatorial acceleration source by attempting other types of signal, and a consideration of the full significance of the disappearance in energy dispersion when this acceleration signal is of constant

amplitude. Further theoretical developments should await, and be based on, future observational results.

This investigation has been notable for its surprises - for example, the field-aligned flows and the steep gradients in the energetic ions - features which have caused difficulty in interpretation both for the writer, and for other investigators of the vortices. However, it is salutary to reflect that these surprises demonstrate the value of an empirical approach to magnetospheric theory, for only through in situ observations by a well-equipped instrument payload will one ultimately understand the full complexities of key magnetospheric phenomena.

The surprises, though often a source of irritation with the inevitable setbacks involved, have also provided a challenge, a challenge which has made the vortices fascinating phenomena to study. When one considers that they were discovered barely four years ago, one wonders also how many other intriguing space physics phenomena remain to be revealed!

REFERENCES

Bame, S.J., Ashbridge, J.R., Felthauser, H.E., Glore, J.P., Paschmann, G., Hemmerich, P., Lehmann, K. and Rosenbauer, H., ISEE 1 and ISEE 2 fast plasma experiment and the ISEE 1 solar wind experiment, IEEE Trans. Geosci. Electron., GE-16, 216, 1978.

Barfield, J.N. and McPherron, R.L., Statistical characteristics of storm-associated Pc5 micropulsations observed at the synchronous equatorial orbit, J. Geophys. Res., 77, 4720, 1972.

Cahill, L.J. and Amazeen, P.G., The boundary of the geomagnetic field, J. Geophys. Res., 68, 1835, 1963.

Clemmow, P.C. and Dougherty, J.P., 'Electrodynamics of Particles and Plasmas', Addison-Wesley, London, 1969.

Compton, A.H. and Getting,I.A., An apparent effect of galactic rotation on the intensity of cosmic rays. Phys. Rev., 47, 818, 1935.

Coroniti, F.V. and Kennel, C.F., Auroral micropulsation instability, J. Geophys. Res., 75, 1863, 1970.

Cowley, S.W.H., The effect of pressure anisotropy on the equilibrium structure of magnetic current sheets, Planet. Space Sci., 26, 1037, 1978.

Cowley, S.W.H., Plasma populations in a simple open model magnetosphere, Space Sci. Rev., 26, 217, 1980.

Dungey, J.W., Electrodynamics of the outer atmosphere, Report 69 (Ionos. Res. Lab., Pa. State Univ.), 1954.

Dungey, J.W., in 'Physics of Geomagnetic Phenomena', edited by B.M. McCormac, p.913, Academic Press, New York,1968.

Durney, A.C., The International Sun-Earth Explorer (formerly IME), ESA Journal, 1, 1, 1977.

Durney, A.C., Mission update: the International Sun-Earth Explorer, EOS Trans. AGU, 61, 701, 1980.

Elphic, R.C. and Russell, C.T., ISEE-1 and 2 observations of the magnetopause, in 'Magnetospheric Boundary Layers', edited by B. Battrick, p.43, ESA SP-148, Noordwijk, Netherlands, 1979.

Fahleson, U.V., Fälthammar, C-G., Lindqvist, P-A., Mozer, F.S., Torbert, R.B., Gonfalone,A. and Pedersen, A., Quasistatic electric fields observed during a number of magnetopause crossings by ISEE 1, in 'Magnetospheric Boundary Layers', edited by B. Battrick, p.51, ESA SP-148, Noordwijk, Netherlands, 1979.

Fahnenstiel, S., Standing waves observed at the dayside magnetopause, Geophys. Res. Lett., 8, 1155, 1981.

Fairfield, D.H., A statistical determination of the shape and position of the geomagnetic neutral sheet, J. Geophys. Res., 85, 775, 1980.

Fritz, T.A., ISEE 1 energetic ion measurements associated with the December 11, 1977 'vortex' event, IAGA Bull. No. 45, IUGG Publications, Paris, France, p.434, 1981.

Gosling, J.T., Ashbridge, J.R., Bame, S.J., Paschmann, G., and Sckopke, N., Observations of two distinct populations of bow shock ions in the upstream solar wind, Geophys. Res. Lett., 5, 957, 1978.

Greenwald, R.A. and Walker, A.D.M., Energetics of long period resonant hydromagnetic waves, Geophys. Res. Lett., 7, 745, 1980.

Hasegawa, A., Drift mirror instability in the magnetosphere, Phys. Fluids, 13, 2642, 1969.

Hasegawa, A. and Mima, K., Anomalous transport produced by kinetic Alfvén wave turbulence, J. Geophys. Res., 83, 1117, 1978 (correction: J. Geophys. Res., 83, 5778, 1978).

Hedgecock, P.C., Giant Pc5 pulsations in the outer magnetosphere: a survey of HEOS 1 data, Planet. Space Sci., 24, 921, 1976.

Hones, E.W., Jr., Paschmann, G., Bame, S.J., Ashbridge, J.R., Sckopke, N. and Schindler, K., Vortices in magnetospheric plasma flow, Geophys. Res. Lett., 5, 1059, 1978.

Hones, E.W., Jr., Birn, J., Bame, S.J., Ashbridge, J.R., Paschmann, G., Sckopke, N. and Haerendel, G.,

Further determination of the characteristics of magnetospheric plasma vortices with ISEE-1 and 2, J. Geophys. Res., 86, 814, 1981.

Hughes, W.J. and Southwood, D.J., The screening of micropulsation signals by the atmosphere and ionsphere, J. Geophys. Res., 81, 3224, 1976a.

Hughes, W.J. and Southwood, D.J., An illustration of modification of geomagnetic pulsation structure by the ionosphere, J. Geophys. Res., 81, 3241, 1976b.

Hughes, W.J., McPherron, R.L., Barfield, J.N. and Mauk, B.H., A compressional Pc4 pulsation observed by three satellites in geostationary orbit near local midnight, Planet. Space Sci., 27, 821, 1979.

Hultqvist, B., in 'The Magnetospheres of Earth and Jupiter', edited by V. Formisano, p.77, Reidel, Dordrecht, 1975.

Ipavich, F.M., The Compton-Getting effect for low energy particles, Geophys. Res. Lett., 1, 149, 1974.

Kremser, G., Korth, A., Fejer, J.A., Wilken, B., Gurevich, A.V. and Amata, E., Observations of quasi-periodic flux variations of energetic ions and electrons associated with Pc5 geomagnetic pulsations, J. Geophys. Res., 86, 3345, 1981.

Lanzerotti, L.J. and Southwood, D.J., Hydromagnetic waves, in 'Solar System Plasma Physics', Vol. 3, edited by L.J. Lanzerotti, C.F. Kennel and E.N. Parker, p.109, North Holland, Amsterdam, 1979.

Lennartsson, W., Shelley, E.G., Sharp, R:D., Johnson, R.G. and Balsiger, H., Some initial ISEE 1 results on the ring current composition and dynamics during the magnetic storm of December 11th, 1977, Geophys. Res. Lett., 6, 483, 1979.

Lepping, R.P. and Burlaga, L.F., Geomagnetopause surface fluctuations observed by Voyager 1, J. Geophys. Res., 84, 7099, 1979.

Lin, C.S. and Parks, G.K., The coupling of Alfvén and compressional waves, J. Geophys. Res., 83, 2628, 1978.

McPherron, R.L. and Coleman, P.J., Jr., Satellite observations of band-limited micropulsations during a

magnetospheric substorm, J. Geophys. Res., 76, 3010, 1971.

Newton, R.S., Southwood, D.J. and Hughes, W.J., The damping of pulsations by the ionosphere, Planet. Space Sci., 26, 201, 1978.

Ogilvie, K.W., Von Rosenvinge, T. and Durney, A.C., International Sun Earth Explorer - a three spacecraft programme, Science, 198, 131, 1977.

Olson, W.P. and Pfitzer, K.A., Magnetospheric magnetic field modelling, McDonnell Douglas Astronautics Co., Preprint, 1977.

Paschmann, G., Sckopke, N., Haerendel, G., Papamastorakis, I., Bame, S.J., Ashbridge, J.R., Gosling, J.T., Hones, E.W., Jr. and Tech, E.R., ISEE plasma observations near the subsolar magnetopause, Space Sci. Rev., 22, 717, 1978.

Paschmann, G., Sonnerup, B.U.Ö., Papamastorakis, I., Sckopke, N., Haerendel, G., Bame, S.J.., Ashbridge, J.R., Gosling, J.T., Russell, C.T. and Elphic, R.C., Plasma acceleration at the Earth's magnetopause: evidence for reconnection, Nature, 282, 243, 1979.

Quinn, J.M. and Southwood, D.J., Observations of parallel ion energisation in the equatorial region, Preprint, 1982.

Roelof, E.C., Keath, E.P., Bostrom, C.O. and Williams, D.J., Fluxes of $\geqslant$ 50keV protons and $\geqslant$ 30keV electrons at $\sim 35R_E$, 1, velocity anisotropies and plasma flow in the magnetotail, J. Geophys. Res., 81, 2304, 1976.

Russell, C.T., Geophysical coordinate transformations, Cosmic Electrodynamics, 2, 184, 1971.

Russell, C.T., ISEE-1 and 2 fluxgate magnetometers, IEEE Trans. Geosci. Electron., GE-16, 239, 1978.

Russell, C.T. and Elphic, R.C., Initial ISEE magnetometer results: magnetopause observations, Space Sci. Rev., 22, 681, 1978.

Russell, C.T. and Elphic, R.C., ISEE observations of flux transfer events at the dayside magnetopause, Geophys. Res. Lett., 6, 33, 1979.

Russell, C.T., Siscoe, G.L. and Smith, E.J. Comparison of ISEE-1 and 3 interplanetary magnetic field observations, Geophys. Res. Lett., 7, 381, 1980.

Saito, T., Long-period irregular magnetic pulsation, Pi3, Space Sci. Rev., 21, 427, 1978.

Sarris, E.T., Krimigis, S.M., Lui, A.T.Y., Ackerson, K.L., Frank, L.A. and Williams, D.J., Relationship between energetic particles and plasma in the distant plasma sheet, Geophys. Res. Lett., 8, 349, 1981.

Sckopke, N., Paschmann, G., Haerendel, G., Sonnerup, B.U.Ö., Bame, S.J., Forbes, T.G., Hones, E.W., Jr. and Russell, C.T., Structure of the low-latitude boundary layer, J. Geophys. Res., 86, 2099, 1981.

Sonnerup, B.U.Ö., Paschmann, G., Papamastorakis, I., Sckopke, N., Haerendel, G., Bame, S.J., Ashbridge, J.R., Gosling, J.T. and Russell, C.T., Evidence for magnetic field reconnection at the Earth's magnetopause, J. Geophys. Res., 86, 10049, 1981.

Southwood, D.J., The behaviour of ULF waves and particles in the magnetosphere, Planet. Space Sci., 21, 53, 1973.

Southwood, D.J., A general approach to low-frequency instability in the ring current plasma, J. Geophys. Res., 81, 3340, 1976.

Southwood, D.J., Localised compressional hydromagnetic waves in the magnetospheric ring current, Planet. Space Sci., 25, 549, 1977.

Southwood, D.J., Magnetopause Kelvin-Helmholtz instability, in 'Magnetospheric Boundary Layers', edited by B. Battrick, p.357, ESA SP-148, Noordwijk, Netherlands, 1979.

Southwood, D.J., Low frequency pulsation generation by energetic particles, J. Geomag. and Geoelec., 32, Suppl. 2, 1980.

Southwood, D.J. and Kivelson, M.G., An approximate analytic description of plasma bulk parameters and pitch angle anisotropy under adiabatic flow in a dipolar magnetospheric field, J. Geophys. Res., 80, 2069, 1975.

Southwood, D.J. and Kivelson, M.G., Charged particle behaviour in low-frequency geomagnetic pulsations, 1, transverse waves, J. Geophys. Res., 86, 5643, 1981.

Spjeldvik, W.N. and Fritz, T.A., Energetic ion and electron observations of the geomagnetic plasma sheet boundary layer: three dimensional results from ISEE 1, J. Geophys. Res., 86, 2480, 1981.

Su, S-Y., Konradi, A. and Fritz, T.A., On the propagation direction of ring current proton ULF waves observed by ATS-6 at $6{\cdot}6R_E$, J. Geophys. Res., 82, 1859, 1977.

Sugiura, M. and Wilson, C.R., Oscillation of the geomagnetic field lines and associated magnetic perturbations at conjugate points, J. Geophys. Res., 69, 1211, 1964.

Thompson, W.B., 'An introduction to Plasma Physics', Pergamon Press, Oxford, 1962.

Williams, D.J., Magnetopause characteristics inferred from three-dimensional energetic particle distributions, J. Geophys. Res., 84, 101, 1979.

Williams, D.J., Keppler, E., Fritz, T.A., Wilken, B. and Wibberenz, G., ISEE-1 and 2 medium energy particles experiment, IEEE Trans. Geosci. Electron., GE-16, 270, 1978.

Williams, D.J., Fritz, T.A., Wilken, B. and Keppler, E., An energetic particle perspective of the magnetopause, J. Geophys. Res., 84, 6385, 1979.

APPENDIX A

SPACECRAFT AND INITIAL ORBIT PARAMETERS

	ISEE 1	ISEE 2	ISEE 3
Structure	IMP modification	New	IMP modification
Spin rate	19·7rpm	19·8rpm	19·75rpm
Mass	340kg	166kg	469kg
Payload mass, power	89kg,76W	28kg,27W	97kg,57W
Number of experiments	13	8	12
Data rate (high)	16kbps	8kbps	2kbps
Data rate (low)	4kbps	2kbps	1kbps
Spin-axis alignment	Perpendicular to ecliptic plane		⊥ar to ecliptic
Launch date	Tandem, 22nd October, 1977		12th August, 1978
Perigee	700km		
Apogee	$22 \cdot 6 R_E$		
Orbital period	57 hours		
Inclination to ecliptic	30°		

APPENDIX B

THE ISEE-1 AND 2 EXPERIMENTS

EXPERIMENT	ISEE 1 PRINCIPAL INVESTIGATOR	ISEE 2 PRINCIPAL INVESTIGATOR
Magnetometer Range 8192γ, sensitivity 0·25γ Range 256γ, sensitivity 0·008γ	C.T. Russell UCLA	C.T. Russell UCLA
Fast Plasma Protons : 70eV–40keV Electrons : 11eV–20keV	S.J. Bame Los Alamos National Laboratory	G. Paschmann Max Planck Institute Munich
Medium Energy Particles Protons : 24 keV–2MeV Electrons : 24keV–1MeV (high angular resolution)	D.J. Williams NOAA, Boulder	E. Keppler Max Planck Institute Lindau
Plasma Waves Electric field : 10Hz–2MHz Magnetic field : 10Hz–10kHz	D.A. Gurnett University of Iowa	D.A. Gurnett University of Iowa
Low Energy Protons and Electrons Protons : 1eV–50keV Electrons : 1eV–250keV (high angular resolution)	L.A. Frank University of Iowa	L.A. Frank University of Iowa
Electron Density Electron density around ISEE 1 and integral between ISEE-1 and 2.	C.C. Harvey Meudon Observatory, Paris	C.C. Harvey Meudon Observatory, Paris
Protons and Electrons Protons : 8–380keV Electrons : 8–200keV (high time resolution)	K.A. Anderson University of California Berkeley	K.A. Anderson University of California Berkeley
Quasistatic Electric Fields 0–12Hz	F.S. Mozer University of California Berkeley	———
D.C. Electric Field 0·1–3200Hz	J.P. Heppner Goddard Space Flight Center	———
Ion Composition Cold plasma composition up to 40keV/charge	R.D. Sharp Lockheed, Palo Alto	———
Low Energy Cosmic Rays Particle composition up to 20MeV/nucleon	D. Hovestadt Max Planck Institute, Munich	———
Fast Electrons Electrons : 6eV–10keV	K.W. Ogilvie Goddard Space Flight Center	———
VLF Wave Propagation Reception from ground transmitter	R.A. Helliwell Stanford University	———
Solar Wind Ions : 0·01–10keV/charge	———	G. Moreno Frascati, Rome

APPENDIX C

SOFTWARE CONTRIBUTIONS

Two contributions to the ICST Space Physics Group software library are briefly described. The first is a routine for converting data into a Boundary Normal or LMN coordinate system for studies in connection with the magnetopause. In this system, introduced by Russell and Elphic (1978), and illustrated below, $\hat{N}$ is directed outwards along the normal to the magnetopause, $\hat{L}$ points northward so that the GSM $\hat{Z}$ axis lies in the LN plane, while $\hat{M}$ completes the orthogonal triad and points westward.

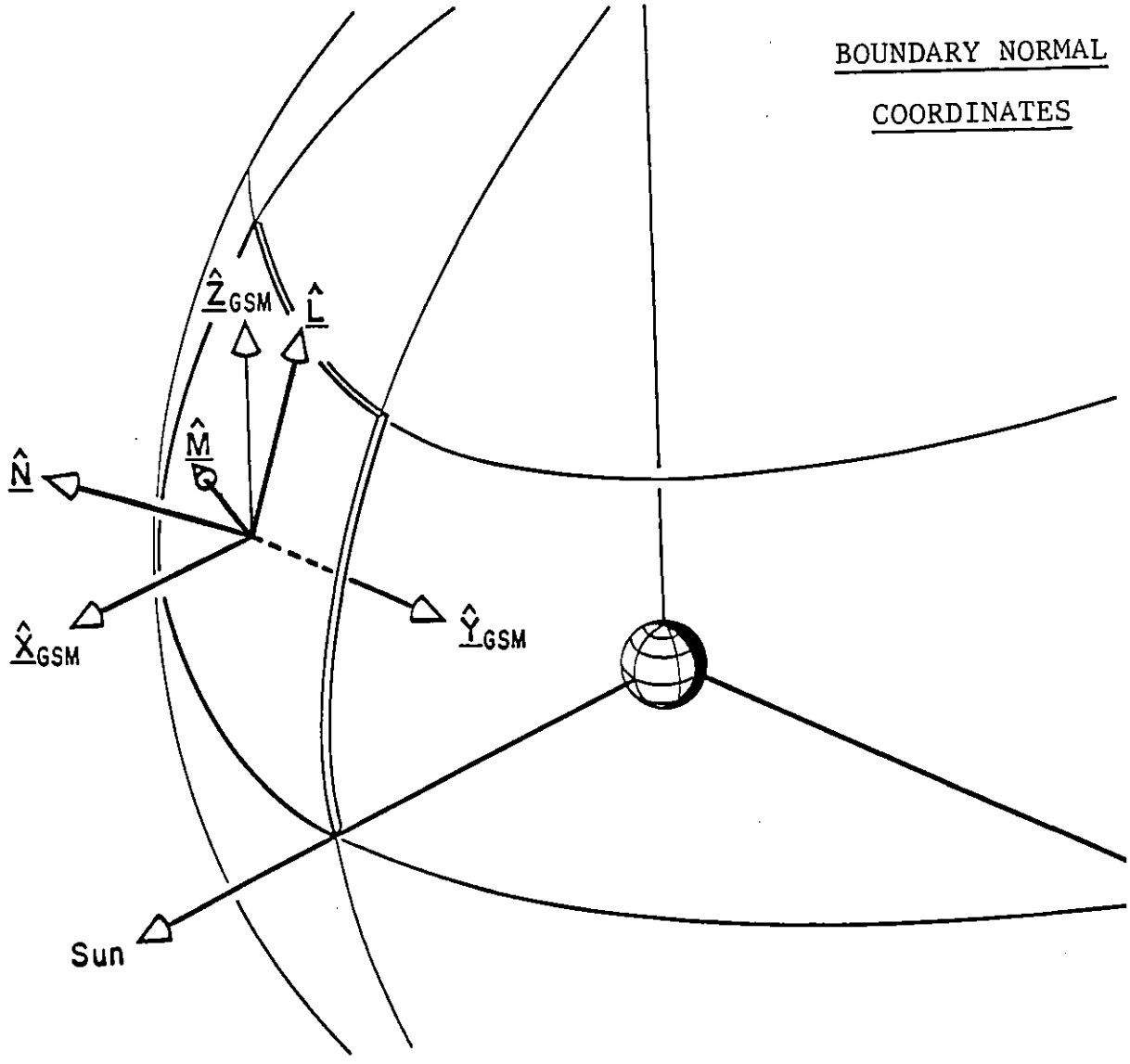

The benefit of using a Boundary Normal coordinate system in magnetopause work is that it confines variations in the data to two dimensions (the LM plane), thereby making the data easier to understand. The fact that the global GSE or GSM systems rarely achieve this ordering, partly explains why important magnetopause-associated features such as flux transfer events (Russell and Elphic, 1978, 1979; Elphic and Russell, 1979), were not reported in spacecraft data earlier. Although the normal direction can be determined in different ways, we favour the method which assumes that the magnetopause is a tangential discontinuity, so that $\hat{\underline{N}}$ is obtained by taking the cross product of suitably chosen internal and external fields.

The second software contribution mentioned here also relates to the magnetopause. A graphics programme has been written which displays the strength and components (in LMN coordinates) of the field simultaneously for both spacecraft.

APPENDIX D

ROUTINE FOR CONVERTING TO MEAN FIELD-ALIGNED (MVA) COORDINATES

```
      SUBROUTINE XYZMVA(X,Y,Z,XM,YM,ZM,VMAG,XMVA,YMVA,ZMVA)
C
C     SUBROUTINE TO TRANSFORM A VECTOR IN THE XYZ COORDINATE
C     SYSTEM TO MEAN VECTOR ALIGNED COORDINATES WITH +Z IN
C     THE DIRECTION OF THE MEAN VECTOR SPECIFIED BY XM,YM,ZM AND
C     +Y IN THE YZ PLANE OF THE ORIGINAL COORDINATE SYSTEM.
C
C     ANTICLOCKWISE ROTATION THROUGH THETA ABOUT X
C
      THETA=-ATAN2(YM,ZM)
      YMVA=Y*COS(THETA)+Z*SIN(THETA)
      Z1=-Y*SIN(THETA)+Z*COS(THETA)
C
C     CLOCKWISE ROTATION THROUGH THETA ABOUT Y
C
      VMAG=SQRT(XM**2+YM**2+ZM**2)
      THETA=ASIN(XM/VMAG)
      XMVA=X*COS(THETA)-Z1*SIN(THETA)
      ZMVA=X*SIN(THETA)+Z1*COS(THETA)
C
      RETURN
      END
```

APPENDIX E

Proof that a sinusoidal acceleration signal of constant amplitude localised at the equator, will not give rise to energy dispersion.

Let us start from equation (36), the expression for $\delta v_{||}(t_o)$:

$$\delta v_{||}(t_o)=\frac{\dot{W}_o \Delta s}{mv\, v_{||}}\, e^{i\omega(t_o-s_o/v)} e^{-\gamma(t_o-s_o/v)} \left[\frac{1-e^{\gamma t_o}e^{-i\omega t_o}}{1-e^{\gamma \ell/v}e^{-i\omega \ell/v}}\right] \left(1-e^{-i\omega(\ell-2s_o)/v}e^{\gamma(\ell-2s_o)/v}\right)$$

and consider the limit when $\gamma=0$, that is, when there is no damping. In that case the $\delta v_{||}(t_o)$ phase information is:

$$e^{i\omega(t_o-s_o/v)} \left[\frac{1-e^{-i\omega t_o}}{1-e^{-i\omega \ell/v}}\right] \left(1-e^{-i\omega(\ell-2s_o)/v}\right)$$

$$=\left(e^{i\omega t_o}-1\right) e^{-i\omega s_o/v}\left(1-e^{i\omega \ell/v}\right)\left(1-e^{-i\omega(\ell-2s_o)/v}\right)$$

$$=\left(e^{i\omega t_o}-1\right) e^{-i\omega s_o/v}\left(1+e^{i\omega 2s_o/v}-e^{i\omega \ell/v}-e^{-i\omega(\ell-2s_o)/v}\right)$$

$$=\left(e^{i\omega t_o}-1\right)\left(e^{-i\omega s_o/v}+e^{i\omega s_o/v}-e^{i\omega(\ell-s_o)/v}-e^{-i\omega(\ell-s_o)/v}\right)$$

$$=2\left(e^{i\omega t_o}-1\right)\left(\cos(\omega s_o/v)-\cos\left|\omega(\ell-s_o)/v\right|\right) \quad .$$

The left hand bracket is speed independent describing only the phase of the source signal. The right hand bracket contains the velocity dependent phase information. As there is no imaginary part to the latter it is clear that the energy dispersion is zero; that is, $\delta v_{||}(t_o)$ is in phase for all v and s_o.
